eXPRESS Polymer Letters Vol.4, No.12 (2010) 742
Available online at www.expresspolymlett.com
DOI: 10.3144/expresspolymlett.2010.89

# Editorial corner – a personal view

## Physically Networked Polymers: Materials that change with their environment

R. A. Shanks[*]

School of Applied Sciences, RMIT University, GPO Box 2476V, Melbourne, 3001, Australia

Polymer networks have continuity of molecular and intermolecular links throughout their structure. These links can be established by covalent, polar or dispersive forces. The choice of link depends on whether a permanent or a reversible structure is required. The continuous network and matrix phase may be different, either chemically or physically, if there is identifiably separate phases. When network formation is through a filler a percolation threshold concentration must be exceeded. Agglomeration of the filler will produce a non-linear strain response. When the matrix phase is of distinct chemistry and physically it can be a gas (aerogel), liquid (gel) or solid (dispersed or co-continuous). The emphasis of this discussion is on reversible networks. They require a reversing stimulus, typically heat, shear, pH, electrical or magnetic. The magnitude of the reversing force is important for application.

Thermoplastic rubbers require reversal of physical cross-links during processing, for all other circumstances they must have a permanent network structure. Reological additives exhibit network reversal on shear and the gelling forces should be weak and potentially rapidly reversible. Dispersive forces, called hydrophobic forces when a polar medium is the matrix, meet networking criteria. Ionic or dipolar forces can be enhanced by molecular orientation formed by shear or an electrical field thus causing an increase in structure formation with a rheopectic or shear thickening effect. In solids such additives modify the viscoelastic properties. The distinction between a liquid and a solid is uncertain for amorphous materials.

A feature of more recent research is the formation of self-assembling network systems, often using functionalized polymers with interacting groups having high specificity and facile reversibility. Reversibility is either self-controlled in response to changes in the environment or activated by external stimuli, such as those mentioned above. Materials with these responsive changes to their structure have been called smart materials. A reverse situation may apply where changes in the structure of the material lead to changes in the stimulus field. Changing chemical, mechanical or shear conditions may lead to a change in conductivity or light transmission, so the material can become a sensor. Nematic liquid crystalline ordering of side-chain mesogens can be controlled by electro-optical stimuli. Thermo-reversible networks are much studied, but network formation can be activated by electrical or magnetic fields. Many new materials are based upon the principles that have been discussed with the similarity that they include reversible supramolecular structures.

Prof. Dr. Robert A. Shanks
Member of International Advisory Board

---

[*] Corresponding author, e-mail: robert.shanks@rmit.edu.au

*eXPRESS Polymer Letters Vol.4, No.12 (2010) 743–752*
*Available online at www.expresspolymlett.com*
*DOI: 10.3144/expresspolymlett.2010.90*

# Synergistic effects of sepiolite on intumescent flame retardant polypropylene

*N. H. Huang*[1,2*], *Z. J. Chen*[1,2], *J. Q. Wang*[3], *P. Wei*[4]

[1]Key Laboratory of Green Processing and Functional Textiles of New Textile Materials, Ministry of Education, Wuhan Textile University, Wuhan 430073, China
[2]Department of Polymer Science and Engineering, Wuhan Textile University, Wuhan 430073, China
[3]National Laboratory of Flame Retardant Materials, Beijing Institute of Technology, Beijing 100081, China

*Received 11 May 2010; accepted in revised form 17 August 2010*

**Abstract.** In this paper, the effects of sepiolite as a synergistic agent on the flame retardancy of intumescent flame retardant polypropylene (PP/IFR) were studied using the limiting oxygen index (LOI), the UL-94 test, thermogravimetric analysis (TGA), laser Raman spectroscopy (LRS), cone calorimeter test (CCT) and scanning electron microscopy (SEM), and the IFR system mainly consisted of the ammonium polyphosphate modified with γ-aminopropyltriethoxysilane coupling agent, melamine and dipentaerythritol. The results from the LOI and UL 94 tests show that sepiolite added to the PP/IFR system has a synergistic flame retardant effects with the IFR system. The TGA results reveal that sepiolite enhances the thermal stability of the PP/IFR composite and increases the char residue formation. The cone calorimeter results indicate that the heat release rate, mass loss rate, total heat release and average specific extinction area of the PP/IFR/sepiolite composite decrease in comparison with the PP/IFR composite. The LRS measurements provide useful information on the carbonaceous microstructures. The morphological structures observed by SEM have demonstrated that sepiolite promote the formation of the reinforced and homogeneous char barrier on the surface of the composites. Simultaneously, the Young's modulus and flexural modulus of the PP/IFR composites are also much better improved with the increase of sepiolite added.

***Keywords:*** *polymer composites, sepiolite, polypropylene, intumescent flame retardant, synergistic effect*

## 1. Introduction

Polypropylene (PP) is an important commodity plastic and used extensively in many fields, such as housing, transportation, and electrical engineering materials, but its usage is often limited because of its poor flame retardancy (the limiting oxygen index (LOI) is often lower than 18%). Therefore, studies on flame-retardant PP have attracted considerable interest during the last decades. One of the most important ways to improve the fire retardancy of PP is by applying an intumescent flame retardant (IFR) [1–5]. On heating, the IFR additives form a foamed cellular charred layer on the surface of the product, which slows down the heat and mass transfer between the gas and the condensed phase. Moreover, the IFR systems reduce the smoke density and produce little corrosive gas during combustion.

However, the IFR systems are relatively effective at low concentrations but not enough in stringent cases. In order to enhance the flame retardancy, new intumescent flame retardant systems have been developed rapidly [3, 6–8], which has high flame retardant efficiency. In addition, some synergistic agents have also been used to improve further the flame retardant of intumescent flame retardant PP systems, such as nano-$Mn_{0.4}Zn_{0.6}Fe_2O_4$ [9], zeolites [10], montmorillonite [11, 12], silica [13],

---

[*]Corresponding author, e-mail: nhhuang1223@yahoo.com.cn

alumina [13], silicotungstic acid [14], lanthanum oxide [15, 16], nano-$BaWO_4$ [17], expandable graphite [18], iron powder [19], nanoflaky manganese phosphate [20], phosphotungstic acid [21], hydroxy silicone oil [22], a-ZrP [23], colemanite [24], zinc borate [25], polysilsesquioxane [26], borosiloxane [27] and other metallic compounds [1]. Sepiolite is a family of fibrous hydrated magnesium silicate with the theoretical half unit-cell formula $Si_{12}O_{30}Mg_8(OH)_4\ (OH_2)_4{\cdot}8H_2O$ characterized by a needle-like morphology [28]. It can have a surface area as high as 200–300 $m^2/g$, lengths of 0.2–4 µm, a width of 10–30 nm and thickness of 5–10 nm [29]. In a previous study, we found that sepiolite has a good flame retardant synergistic effect with magnesium hydroxide in EVA [30] or PP [31]. However, there are few reports about sepiolite use in IFR polypropylene [32, 33].

In general, the poor water resistance and compatibility with PP matrix of traditional IFR system based on ammonium polyphosphate (APP), melamine and pentaerythritol restrict its application. Demir *et al.* [34] found that surface modification of APP with 3-(trimethoxysilyl)-1-propanethiol coupling agent can improve its water resistance and the compatibility. So, the IFR system based on APP modified with γ-aminopropyltriethoxysilane coupling agent was used as flame retardant in this paper.

The objective of this paper is to study the synergistic effects of sepiolite with the IFR system based on ammonium polyphosphate (IFR) modified with γ-aminopropyltriethoxysilane coupling agents, melamine and dipentaerythritol in PP using the limiting oxygen index (LOI), UL-94 test, thermogravimetric analysis(TGA), cone calorimeter test, Raman spectroscopy, and scanning electron microscopy (SEM). Mechanical properties of the composites have also been tested. More detailed investigations concerning the thermal degradation mechanism of PP/IFR/sepiolite composite are still ongoing by using *in situ* FTIR, TG/FTIR, Py-GC-MS and XPS techniques in the lab.

## 2. Experimental

### 2.1. Materials

Polypropylene powder (PP) (PPH-XD-075, melt flow rate: 2.1 g/10 min, 230°C, 2.16 kg), with the particle size 140–240 µm, was purchased from Wuhan Petroleum Chemical Plant, China. The intumescent flame retardant system containing 22±2 wt% P, 18±1 wt% N with an average particle size of 10 µm, which consisted of ammonium polyphosphate modified with γ-aminopropyltriethoxysilane coupling agent (APP), melamine (MN) and dipentaerythritol (DPER) (the mass ratio of APP, MN and DPER is 4:1:1), was purchased from Hangzhou JLS Flame Retardants Chemical Co., Ltd., China. Non-modified Pangel S9 sepiolite was kindly supplied by Tolsa SA (Spain).

### 2.2. Composites preparation

Prior to mixing and getting the sepiolite dried the sample was heated first at 100°C for 4 h and cooled slowly then to room temperature under vacuum for 16 h. PP matrix composites were firstly prepared by blending of PP, IFR and sepiolite using a high-speed mixer (approximately 1000 r/min). Concentration of fillers was fixed at 25% mass of total amounts of composite. Sepiolite was added with mass fractions of 1, 2, 3 and 4%. Then flame retardant PP composites were extruded by a co-rotating twin-screw extruder (diameter = 20 mm, length/diameter = 36, model: SHJ-20, Lanzhou Tianhua Chemical Engineering and Automation Company, China) at a temperature profile of 130, 150, 180, 190, 200, 205, 200°C, and cutting into pellets using a granulator. The resulting sample bars for testing were prepared by injection moldings (injector: model HBL-1300, Zhejiang Haibo Co., Ltd., China) at a temperature profile of 200, 210 and 215°C.

### 2.3. Characterization

#### 2.3.1. Limiting oxygen index

Limiting oxygen index (LOI) measurements were carried out using a JF-3 type instrument (Jiangning Analysis Instrument Factory, China) according to GB 2406-80 (ASTM D 2863-77). The samples used for the test were of dimensions 100 mm× 6.5 mm×3 mm.

#### 2.3.2. UL-94 test

The UL-94 vertical test was measured on a CZF-2 type instrument (Jiangning Analysis Instrument Factory, China) with sample dimensions of 127 mm× 12.7 mm×3 mm according to ASTM D 635-77. UL-94 test results are classified by burning ratings

V-0, V-1 or V-2. V-0 rating presents the best flame retardancy of polymeric materials.

### 2.3.3. Thermogravimetric analysis

Thermogravimetric analysis (TG) was performed on a NETZSCH thermal analyzer (TG 209 F1). Samples weighting about 5.0 mg were heated from room temperature to 700°C at a heating rate of 10°C/min in a dynamic nitrogen atmosphere. The nitrogen flow rate was 50 ml/min.

### 2.3.4. Cone calorimeter test

Combustion experiments were performed in a cone calorimeter (Fire Testing Technology, UK) at an incident heat flux of 35 kW/m$^2$ according to ISO 5600. The bottom and edges of each specimen with a dimension of 100 mm×100 mm×4 mm are wrapped with aluminum foil. All samples were run in duplicate and the average value was reported. Various parameters can be measured including time to ignition (TTI), heat release rate (HRR) as a function of time, peak of heat release rate (PHRR), mass loss rate, and so on. The experimental error of data from the cone calorimeter was about 5%.

### 2.3.5. Raman spectroscopy

The Raman spectra were obtained from a Thermo Fisher Scientific Raman Spectrometer (model DXR) coupled with an OLYMPUS BX51 optical microscope. Excitation wavelengths were 633 nm using a He-Ne laser. The laser power at the sample was kept below 2 mW to avoid degradation problems or peak shifts due to overheating effects. The laser was focused to a 2 μm diameter spot on the sample using a 50× objective lens. The spectral resolution was 2 cm$^{-1}$. The Raman spectra were collected and recorded using a Peltier cooled charge-coupled device (CCD) detector with an exposure time of 30 s. Data (baseline calibration and integral) were processed by the Software 'OMNIC 8.1', Thermo Fisher Scientific Company, USA.

### 2.3.6. Scanning electron microscopy

The SEM micrographs of intumescent chars were observed by a JEOL JSM-7401F scanning electron microscopy. The specimens were previously coated with a conductive gold layer.

### 2.3.7 Mechanical properties testing

The impact strengths were measured with an XJJ-5 Charpy impact tester (Chengde Tester Co., Ltd., China) at 23°C according to GB/T1043. Tensile tests were carried out on an Instron Universal Tester Machine (model 5566) with a crosshead speed of 50 mm/min according to ASTM D 638. The tested parallel samples were 10, the presented results are average data.

## 3. Results and discussion

### 3.1. LOI and UL 94 testing

Table 1 presents the changes of LOI values versus sepiolite level for the PP/IFR/sepiolite composites at the total amount of 25 wt% additives kept constant. It is seen that the LOI value of the PP/IFR composite containing 25 wt% IFR increases rapidly to 34.4 from 17.6% of PP, indicating that IFR when used alone can significantly improve flame retardancy of PP. The LOI values of samples (PP0 to PP1) increase to 36.0% with 1.0 wt% loading of sepiolite in the formulation. However, the LOI decreases with further addition of sepiolite. When the loading of sepiolite reached to 4 wt% the LOI value of PP4 decreased to 32.3%. The main reason for this phenomenon may be that, during the combustion process, higher concentration of sepiolite makes the char too rigid and fragile and it increases the heat conductivity.

**Table 1.** LOI and UL-94 data of PP and its flame retardant composites with different loadings of sepiolite

| Sample code | PP [wt%] | IFR [wt%] | SP [wt%] | LOI | UL 94 test | Dripping |
|---|---|---|---|---|---|---|
| PP | 100 | 0 | 0 | 17.6 | no rating | yes |
| PP0 | 75 | 25 | 0 | 34.4 | V-1 | no |
| PP1 | 75 | 24 | 1 | 36.0 | V-0 | no |
| PP2 | 75 | 23 | 2 | 35.8 | V-0 | no |
| PP3 | 75 | 22 | 3 | 35.8 | V-1 | no |
| PP4 | 75 | 21 | 4 | 32.3 | V-2 | no |

UL-94 test results of the PP/IFR composites versus sepiolite loading are given in Table 1. From Table 1, when the loading of sepiolite was kept in between 1 and 2 wt% in IFR, and samples of the PP/IFR composites can pass the V-0 rating. However, further increasing to 3 and 4 wt%, they only pass the V-1 rating and V-2 rating as revealed by samples PP3 and PP4, respectively. These results indicate that an appropriate amount of sepiolite may cause the synergistic effect in the PP/IFR/Sepiolite composites more efficient.

## 3.2. Cone calorimeter study

Cone calorimetry is widely used to evaluate fire performance of materials. Various parameters can be obtained from cone calorimetry including the time to ignition (TTI), the heat release rate (HRR), the peak heat release rate (PHRR), the total heat release (THR), average mass loss rate (av-MLR), average specific extinction area (av-SEA) and fire performance index (FPI) (defined as a ratio of TTI/PHRR) [35], and so on. The heat release rate (HRR) is a very important parameter, and can be used to express the intensity of a fire. An effective flame retardant system normally shows a low HRR value.

The heat release rate curves for PP and its flame retardant PP composites are shown in Figure 1 and all of the cone calorimetric data is presented in Table 2. It can be seen that the pristine PP burns very fast after ignition and a sharp HRR peak appears with a PHRR of 662 kW/m$^2$. The curve of the PP/IFR composite without sepiolite showed much lower peak heat release rate (PHRR) of 71 kW/m$^2$, and two peaks are observed at about 63 and 440 s, respectively. According to a former study [20], the first peak could be due to the development of the intumescent protective structure, and the second peak could be assigned to the degradation of this protective layer. In the IFR system, ammonium polyphosphate is used as the acid source; during heating, the poly(phosphoric acid) formed in the degradation of APP provides an acid catalyst for organic reactions [36]. During the heating process of APP, gaseous products (mainly ammonia), make the mixture of the phosphor-carbonaceous residue swollen; this leads to the formation of the intumescent char residue. The PHRR values (see Table 2) for PP/IFR composite with 1% sepiolite was 51 kW/m$^2$, which was much lower than that for pristine PP (662 kW/m$^2$) and that for PP/IFR composite (71 kW/m$^2$). It was also noteworthy that the HRR curve for PP/IFR/SP 1% composite exhibited a flattened pattern at 400–600 s, as shown in Figure 1. This was probably because sepiolite enhanced the strength and thermal stability of char layer, prevented the char layer from cracking and promoted the formation of the homogenous and compact intumescent char layer (see the SEM micrographs to be presented later). It was also found that IFR and sepiolite obviously render the ignition time shortened (see Table 2) which is attributed to the char layer formation on the surface of the PP/IFR composites. This is because the char layer prevents heat and oxygen from transferring into the matrix interior [16]. At the initial stage of heating, the surface temperature of the PP/IFR and PP/IFR/SP composites rises quickly due to the char

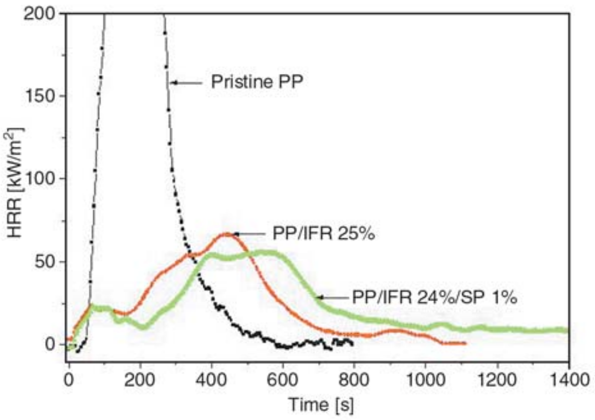

**Figure 1.** Heat release rate curves for pristine PP, PP/IFR and PP/IFR/SP 1% composites at a heat flux of 35 kW/m$^2$

**Table 2.** Cone summary results of pristine PP and its flame retardant composites (35 kW/m$^2$)

| Sample | TTI [s] | PHRR [kW/m$^2$] | THR [MJ/m$^2$] | av-SEA [m$^2$/kg] | av-MLR [g/s·m$^2$] | FPI [kW/m$^2$·s] |
|---|---|---|---|---|---|---|
| Pristine PP | 48 | 662 | 83.3 | 487.8 | 0.040 | 0.073 |
| PP/IFR 25% | 30 | 71 | 32.5 | 348.2 | 0.012 | 0.423 |
| PP/IFR 24%/SP 1% | 29 | 51 | 30.8 | 238.9 | 0.009 | 0.569 |

TTI, time to ignition; PHRR, peak heat release rate; THR, total heat release; av-SEA, average specific extinction area; av-MLR, average mass loss rate; FPI, fire performance index

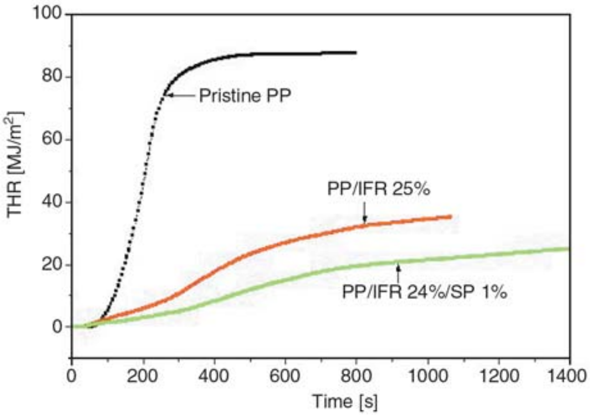

**Figure 2.** Total heat release (THR) curves for pristine PP, PP/IFR and PP/IFR/SP 1% composites at a heat flux of 35 kW/m²

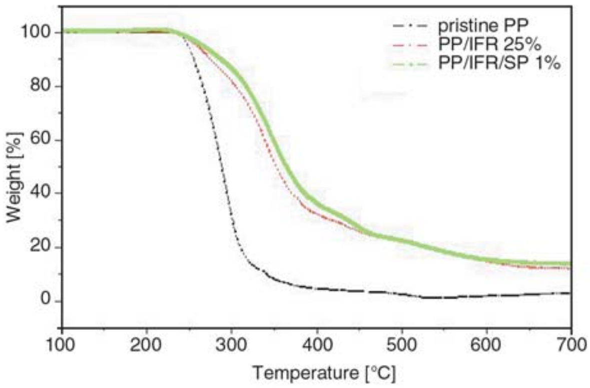

**Figure 3.** TG curves of pristine PP, PP/IFR and PP/IFR/SP 1% composites in $N_2$ at a heating rate of 10°C/min

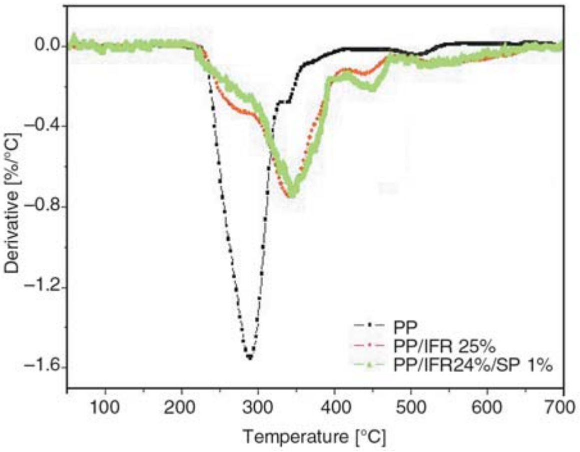

**Figure 4.** DTG curves of pristine PP, PP/IFR and PP/IFR/SP 1% composites in $N_2$ at a heating rate of 10°C/min

layer formation, this results in fast decomposition of PP on the surface of the composites. Therefore, this makes the ignition time (TTI) shortened.

Figure 2 shows another plot for total heat release (THR) of all samples. Similar conclusion can be drawn that the THR goes down while the flame retardant IFR and IFR/SP were incorporated in. Consequently, it is also suggested that the synergistic effect between IFR and sepiolite is well deserved in the system.

Fire performance index (FPI) is independent of the tested sample thickness and often used to predict whether a material can easily develop drastic combustion after ignition. Therefore, the smaller the FPI value is, the better the fire resistance is. From Table 2, PP/IFR/SP 1% composite has the smallest value of 1.76, indicating that sepiolite can improve the flame retardant efficiency of PP/IFR composite. In addition, it clearly shows that both the smoke emission and average mass loss rate during combustion process are depressed by the incorporation of sepiolite.

### 3.3. Thermogravimetric analysis

Figures 3 and 4 present TG and DTG curves of pristine PP, PP/IFR, and PP/IFR/SP 1% samples under a flow of $N_2$, respectively. The 10% mass loss temperature ($T_{10\%}$), the maximum mass loss temperature ($T_{max}$), the maximum mass loss rate ($R_{max}$), and char (or residue) yield values at 700°C are all summarized in Table 3. PP loses the weight in the temperature range 249–350°C, formation a residue of about 2.7% at 700°C. It is clearly seen from Table 3 that the onset temperature (temperature at 10% mass loss, $T_{10\%}$) is increased for all composites, by 23°C for PP/IFR composite and 33°C for PP/IFR/SP 1% composite, respectively. The above results indicate that sepiolite improves the thermal stability of PP/IFR composite. However, this does

**Table 3.** TGA data of pristine PP, PP/IFR and PP/IFR/SP 1% samples under $N_2$ at a heating rate of 10°C/min

| Sample | $T_{10\%}$ [°C] | $T_{max}$ [°C] | $R_{max}$ [%/min] | Residue yield at 700°C [wt%] |
|---|---|---|---|---|
| Pristine PP | 255 | 295 | 1.55 | 2.7 |
| PP/IFR | 278 | 340 | 0.75 | 11.8 |
| PP/IFR/SP 1% | 288 | 347 | 0.73 | 13.9 |

$T_{10\%}$ is the temperature at 10% weight loss; $T_{max}$ is the temperature at which the rate of weight loss reaches a maximum.
$R_{max}$ is the maximum rate of weight loss.

notcorrelate with a decrease of TTI in the cone calorimeter (see Table 2). The fact may be attributed to the existence of sepiolite which may cause the whole process more complicated.

The IFR made a profound effect on the maximum thermal decomposition temperature ($T_{max}$). It can be seen from Table 3 that with the IFR obviously enhanced $T_{max}$ of PP, which is 295°C for pristine PP, 340°C for the PP/IFR composite and 347°C for the PP/IFR/SP 1% composite, respectively. This fact demonstrated that the char layer formed at higher temperature protected PP from decomposing. The maximum mass loss rate ($R_{max}$) for PP/IFR composite with and without sepiolite are decreased from 1.55 to 0.75, 0.73%/°C, respectively. It is noteworthy that the char residue of pristine PP and PP/IFR composite are only 2.7 and 11.8 wt% at 700°C, respectively, while that of PP/IFR composite containing 1 wt% sepiolite is 13.9 wt%. This illuminates that sepiolite could promote the char formation of the PP/IFR composites.

### 3.4. Morphology analysis of the char residue

The morphology of the residual char formed after cone calorimeter testing is investigated by scanning electron microscopy (magnification 500×). Figures 5a and 5b present the SEM photographs of the outer char of the PP/IFR composite and PP/IFR/SP 1% composite, respectively. As shown in Figure 5a, it is observed that the char is loose and porous, so it cannot provide the good flame shield for the underlying material. Comparing Figure 5b with Figure 5a, it is found that the char of the PP/IFR/SP 1% composite is more homogenous than that of the PP/IFR composite. Moreover, the addition of sepiolite also seems to reinforce the char barrier, keeping it more resistant against the disintegrating effect of the bubbles evolved. So the char layer with improved performance leads to the enhancement of flame retardancy.

### 3.5. Microstructure characterization of carbonaceous charred layers

Raman spectroscopy has been proven an effective method to investigate the carbonaceous char formed by combustion of polymers [37–39]. Figure 6 shows the Raman spectra of the char residues formed after cone calorimeter testing. The spectra of the char residues with or without sepiolite exhibit two broad bands around 1580 and 1350 cm$^{-1}$, similar to the graphite-like species [40]. The first band ($G$ peak) may be assigned to the $E_{2g}$ vibrational mode (C–C vibrations). The band at 1350 cm$^{-1}$ (D peak), the so-called defect band [41], is assigned to the $A_{1g}$ vibrational mode and may be related to the structural organization of the carbonaceous matter. These results provided a positive evidence for the formation of the carbonaceous matter.

Tuinstra and Koening [42] found that the relative intensity ration $R$ of the $D$ peak to the $G$ peak is

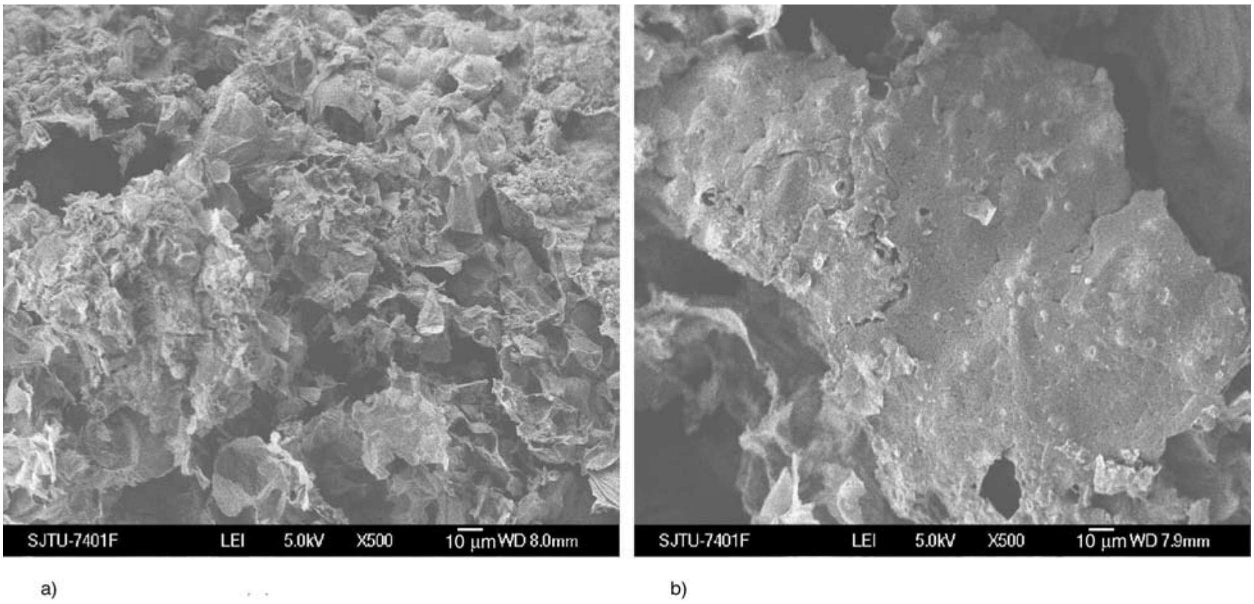

**Figure 5.** SEM micrographs of PP/IFR char residue with and without sepiolite: (a) PP/IFR composite, 500×; (b) PP/IFR 24%/SP 1% composite, 500×

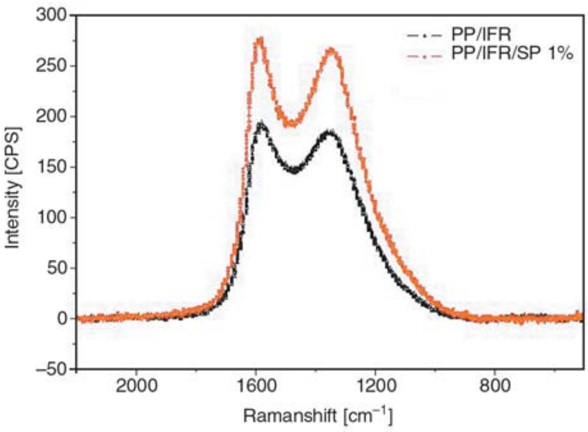

**Figure 6.** Raman spectra of chars produced during cone calorimeter experiments

inversely proportional to an in-plane microcrystalline size. From Figure 6, the relative intensity ration *R* of the *D* peak to the *G* peak for PP/IFR/SP 1% composite (*R* is about 1.15) is higher than that of PP/IFR composite (*R* is about 1.07). That is to say, the size of carbonaceous microstructures from the PP/IFR/SP 1% composite could be smaller than from the PP/IFR composite. Bourbigot *et al.* [43] believed that the higher protective shield efficiency was related to the smaller size of carbonaceous microstructures. Therefore, it is proposed that sepiolite or its pyrolytic products repress the increase of the carbonaceous micro-domain in size during burning, which leads to formation of more compact charred layers.

### 3.6. Mechanical properties

The mechanical properties of pristine PP and its flame retardant composites with different loading of sepiolite are listed in Table 4. Taking PP0 as an example, the addition of IFR by great amount into PP matrix reduces the tensile strength, elongation at break and notched Charpy impact strength, but oppositely for the Young's modulus, flexural strength and flexural modulus. An explanation for the reduction in elongation at break may be the formation of microvoids due to debonding of clay fibres from the polymer matrix upon failure. Comparing sample PP0 with the samples PP1, PP3 and PP4, adding sepiolite into PP/IFR system does not influence the tensile strength, flexural strength and elongation at break very much. However, Young's modulus and flexural modulus for the samples PP1, PP3 and PP4 are increased with increasing sepiolite content, probably because the rigid needle-like sepiolite in PP matrix directly enhanced the stiffness of flame retardant composites. At the same time, notched Charpy impact strength at 23°C for the samples PP1, PP3 and PP4 is slightly increased with increasing sepiolite content.

## 4. Conclusions

Flame-retardant system composed of sepiolite and IFR system (ammonium polyphosphate modified with aminosilane coupling agents and combined with melamine and dipentaerithritol) was processed by melt compounding to flame retard PP resin. The LOI, UL94 test results showed that sepiolite had a significant influence on flame retardancy and LOI value reached 36.0% with loading of 1.0 wt% sepiolite at the total amount of additives kept constant at 25 wt%. Besides, the PP/IFR composites could pass UL 94 V-0 rating with 1–2 wt% sepiolite loading. The TGA results showed that sepiolite enhanced the thermal stability of PP/IFR composite and played a role of promoting the formation of char layer. From the results of cone calorimeter tests, sepiolite had obvious effects on CONE data, such as decreasing the heat release rate (HRR), the total heat release (THR), the average specific extinction area (av-SEA) and the average mass loss rate (av-MLR) during combustion. By the analysis of the morphology and microstructures of char residue by the LRS and SEM, it was revealed that the synergistic effects between sepiolite and IFR on flame retardance was attributed to the improvement in building a reinforced and homogeneous char bar-

**Table 4.** Mechanical properties of pristine PP and its flame retardant composites

| Sample code | PP | PP0 | PP1 | PP3 | PP4 |
|---|---|---|---|---|---|
| Tensile strength [MPa] | 32.4±0.6 | 29.3±0.4 | 30.2±0.4 | 29.8±0.3 | 29.7±0.6 |
| Elongation at break [%] | 32.2±2.1 | 10.1±0.4 | 8.8±0.2 | 9.1±0.4 | 9.2±0.4 |
| Young's modulus [MPa] | 456±37.8 | 670±80.4 | 738±83.6 | 755±38.5 | 768±37.8 |
| Flexural strength [MPa] | 38.9±1.0 | 44.9±0.5 | 46.1±0.9 | 45.4±0.4 | 45.8±1.0 |
| Flexural modulus [MPa] | 1280±47.6 | 1458±17.8 | 1540±17.3 | 1545±17.4 | 1589±27.6 |
| Notched charpy impact strength 23°C [kJ/m$^2$] | 6.1±0.6 | 2.5±0.3 | 2.7±0.2 | 2.8±0.3 | 3.0±0.3 |

rier on the surface of the burning composites. In addition, the rigid needlelike sepiolite in PP matrix directly enhanced the stiffness of flame retardant composites and improved the Young's modulus and flexural modulus.

## References

[1] Lewin M., Endo M.: Catalysis of intumescent flame retardancy of polypropylene by metallic compounds. Polymers for Advanced Technologies, **14**, 3–11 (2003). DOI: 10.1002/pat.265

[2] Du B., Guo Z., Fang Z. P.: Effects of organo-clay and sodium dodecyl sulfonate intercalated layered double hydroxide on thermal and flame behaviour of intumescent flame retarded polypropylene. Polymer Degradation and Stability, **94**, 1979–1985 (2009). DOI: 10.1016/j.polymdegradstab.2009.07.024

[3] Xing W. Y., Song L., Lu H. D., Hu Y., Zhou S.: Flame retardancy and thermal degradation of intumescent flame retardant polypropylene with MP/TPMP. Polymers for Advanced Technologies, **20**, 696–702 (2009). DOI: 10.1002/pat.1335

[4] Zhang M., Ding P., Qu B. J.: Flammable, thermal, and mechanical properties of intumescent flame retardant PP/LDH nanocomposites with different divalent cations. Polymer Composites, **30**, 1000–1006 (2009). DOI: 10.1002/pc.20648

[5] Liu Y., Feng Z. Q., Wang Q.: The investigation of intumescent flame-retardant polypropylene using a new macromolecular charring agent polyamide 11. Polymer Composites, **30**, 221–225 (2009). DOI: 10.1002/pc.20555

[6] Li B., Xu M. J.: Effect of a novel charring-foaming agent on flame retardancy and thermal degradation of intumescent flame retardant polypropylene. Polymer Degradation and Stability, **91**, 1380–1386 (2006). DOI: 10.1016/j.polymdegradstab.2005.07.020

[7] He Q. L., Lu H. D., Song L., Hu Y., Chen L. J.: Flammability and thermal properties of a novel intumescent flame retardant polypropylene. Journal of Fire Sciences, **27**, 303–321 (2009). DOI: 10.1177/0734904109100182

[8] Song P. A., Fang Z. P., Tong L. F., Xu Z. B.: Synthesis of a novel oligomeric intumescent flame retardant and its application in polypropylene. Polymer Engineering and Science, **49**, 1326–1331 (2009). DOI: 10.1002/pen.21153

[9] Wang X. L., Song Y., Bao J. C.: Synergistic effects of nano-$Mn_{0.4}Zn_{0.6}Fe_2O_4$ on intumescent flame-retarded polypropylene. Journal of Vinyl and Additive Technology, **14**, 120–125 (2008). DOI: 10.1002/vnl.20152

[10] Demir H., Arkis E., Balköse D., Ülkü S.: Synergistic effect of natural zeolites on flame retardant additives. Polymer Degradation and Stability, **89**, 478–483 (2005). DOI: 10.1016/j.polymdegradstab.2005.01.028

[11] Tang Y., Hu Y., Li B. Q., Liu L., Wang Z. Z., Chen Z. Y., Fan W. C.: Polypropylene/montmorillonite nanocomposites and intumescent, flame-retardant montmorillonite synergism in polypropylene nanocomposites. Journal of Polymer Science Part A: Polymer Chemistry, **42**, 6163–6173 (2004). DOI: 10.1002/pola.20432

[12] Tang Y., Hu Y., Wang S. F., Gui Z., Chen Z. Y., Fan W. C.: Intumescent flame retardant-montmorillonite synergism in polypropylene-layered silicate nanocomposites. Polymer International, **52**, 1396–1400 (2003). DOI: 10.1002/pi.1270

[13] Wei P., Hao J. W., Du J. X., Wang J. Q.: An investigation on synergism of an intumescent flame retardant based on silica and alumina. Journal of Fire Sciences, **21**, 17–28 (2003). DOI: 10.1177/0734904103021001002

[14] Wu Q., Qu B. J.: Synergistic effects of silicotungistic acid on intumescent flame retardant polypropylene. Polymer Degradation and Stability, **74**, 255–261 (2001). DOI: 10.1016/S0141-3910(01)00155-0

[15] Wu J., Hu Y., Song L., Kang W. J.: Synergistic effect of lanthanum oxide on intumescent flame-retardant polypropylene-based formulations. Journal of Fire Sciences, **26**, 399–414 (2008). DOI: 10.1177/0734904108091990

[16] Li Y. T., Li B., Dai J. F., Jia H., Gao S. L.: Synergistic effects of lanthanum oxide on a novel intumescent flame retardant polypropylene system. Polymer Degradation and Stability, **93**, 9–16 (2008). DOI: 10.1016/j.polymdegradstab.2007.11.002

[17] Wang X. L., Song Y., Bao J. C.: Synergistic effects of nano-$BaWO_4$ on intumescent flame-retarded polypropylene. Polymer-Plastics Technology and Engineering, **48**, 621–626 (2009). DOI: 10.1080/03602550902824465

[18] Wei P., Li H. X., Jiang P. K., Yu H. Y.: An investigation on the flammability of halogen-free fire retardant PP-APP-EG systems. Journal of Fire Sciences, **22**, 367–377 (2004). DOI: 10.1177/0734904104042437

[19] Chen X. L., Jiao C. M., Wang Y.: Synergistic effects of iron powder on intumescent flame retardant polypropylene system. Express Polymer Letters, **3**, 359–365 (2009). DOI: 10.3144/expresspolymlett.2009.45

[20] Zhang P., Song L., Lu H. D., Hu Y., Xing W., Ni J., Wang J.: Synergistic effect of nanoflaky manganese phosphate on thermal degradation and flame retardant properties of intumescent flame retardant polypropylene system. Polymer Degradation and Stability, **94**, 201–207 (2009).
DOI: 10.1016/j.polymdegradstab.2008.11.004

[21] Liu Y., Wang Q.: Catalytic action of phospho-tungstic acid in the synthesis of melamine salts of pentaerythritol phosphate and their synergistic effects in flame retarded polypropylene. Polymer Degradation and Stability, **91**, 2513–2519 (2006).
DOI: 10.1016/j.polymdegradstab.2006.03.009

[22] Chen X. L., Jiao C. M.: Synergistic effects of hydroxy silicone oil on intumescent flame retardant polypropylene system. Journal of Polymer Research, **16**, 537–543 (2009).
DOI: 10.1007/s10965-008-9257-4

[23] Yang D. D., Hu Y., Song L., Nie S. B., He S. Q., Cai Y. B.: Catalyzing carbonization function of α-ZrP based intumescent fire retardant polypropylene nanocomposites. Polymer Degradation and Stability, **93**, 2014–2018 (2008).
DOI: 10.1016/j.polymdegradstab.2008.02.012

[24] Atikler U., Demir H., Tokatli F., Tihminlioglu F., Balköse D., Ülkü S.: Optimisation of the effect of colemanite as a new synergistic agent in an intumescent system. Polymer Degradation and Stability, **91**, 1563–1570 (2006).
DOI: 10.1016/j.polymdegradstab.2005.09.017

[25] Fontaine G., Bourbigot S., Duquesne S.: Neutralized flame retardant phosphorus agent: Facile synthesis, reaction to fire in PP and synergy with zinc borate. Polymer Degradation and Stability, **93**, 68–76 (2008).
DOI: 10.1016/j.polymdegradstab.2007.10.019

[26] Vannier A., Duquesne S., Bourbigot S., Castrovinci A., Camino G., Delobel R.: The use of POSS as synergist in intumescent recycled poly(ethylene terephthalate). Polymer Degradation and Stability, **93**, 818–826 (2008).
DOI: 10.1016/j.polymdegradstab.2008.01.016

[27] Marosi G., Márton A., Szép A., Csontos I., Keszei S., Zimonyi E., Tóth A., Almeras X., Bras M.: Fire retardancy effect of migration in polypropylene nanocomposites induced by modified interlayer. Polymer Degradation and Stability, **82**, 379–385 (2003).
DOI: 10.1016/S0141-3910(03)00223-4

[28] Tartaglione G., Tabuani D., Camino G.: Thermal and morphological characterisation of organically modified sepiolite. Microporous and Mesoporous Materials, **107**, 161–168 (2008).
DOI: 10.1016/j.micromeso.2007.04.020

[29] Ma J., Bilotti E., Peijs T., Darr J. A.: Preparation of polypropylene/sepiolite nanocomposites using supercritical $CO_2$ assisted mixing. European Polymer Journal, **43**, 4931–4939 (2007).
DOI: 10.1016/j.eurpolymj.2007.09.010

[30] Huang N. H., Chen Z. J., Wang J. Q.: Synergistic flame retardant effects between sepiolite and magnesium hydroxide in ethylene-vinyl acetate (EVA) matrix. Express Polymer Letters, **4**, 227–233 (2010).
DOI: 10.3144/expresspolymlett.2010.29

[31] Marosfői B. B., Garas S., Bodzay B., Zubonyai F., Marosi G.: Flame retardancy study on magnesium hydroxide associated with clays of different morphology in polypropylene matrix. Polymers for Advanced Technologies, **19**, 693–700 (2008).
DOI: 10.1002/pat.1153

[32] Marosfői B., Szabó A., Kiss K., Marosi G.: Use of organosilicone composites as flame retardant additives and coating for polypropylene. in 'Fire retardancy of polymers: New strategies and mechanisms' (eds.: Kandola K., Hull R.) The Royal Society of Chemistry, London, Vol 4, 49–58 (2008).

[33] Szabó A., Marosfői B., Anna P., Marosi G.: Complex micro-analysis assisted design of fire retardant nanocomposites- contribution to the nano-mechanism. in 'Fire retardancy of polymers: New Strategies and Mechanisms' (eds.: Kandola K., Hull R.) The Royal Society of Chemistry, London, Vol 4, 74–91 (2008).

[34] Demir H., Balköse D., Ülkü S.: Influence of surface modification of fillers and polymer on flammability and tensile behaviour of polypropylene-composites. Polymer Degradation and Stability, **91**, 1079–1085 (2006).
DOI: 10.1016/j.polymdegradstab.2005.07.012

[35] Schartel B., Hull T. R.: Development of fire-retarded materials- Interpretation of cone calorimeter data. Fire and Materials, **31**, 327–354 (2007).
DOI: 10.1002/fam.949

[36] Bourbigot S., Le Bras M., Delobel R., Bréant P., Trémillon J-M.: Carbonization mechanisms resulting from intumescence-part II. Association with an ethylene terpolymer and the ammonium polyphosphate-pentaerythritol fire retardant system. Carbon, **33**, 283–294 (1995).
DOI: 10.1016/0008-6223(94)00131-I

[37] Bras M. L., Bourbigot S., Tallec Y. L., Laureyns J.: Synergy in intumescence- Application to β-cyclodextrin carbonisation agent in intumescent additives for fire retardant polyethylene formulations. Polymer Degradation and Stability, **56**, 11–21 (1997).
DOI: 10.1016/S0141-3910(96)00190-5

[38] Hillemans J. P. H. M., Colemonts C. M. C. J., Meier R. J., Kip B. J.: An *in situ* Raman spectroscopic study of the degradation of PVC. Polymer Degradation and Stability, **42**, 323–333 (1993).
DOI: 10.1016/0141-3910(93)90228-B

[39] Zhu S. W., Shi W. F.: Thermal degradation of a new flame retardant phosphate methacrylate polymer. Polymer Degradation and Stability, **80**, 217–222 (2003).
DOI: 10.1016/S0141-3910(02)00401-9

[40] Bourbigot S., Le Bras M., Delobel R., Decressain R., Amoureux J. P.: Synergistic effect of zeolite in an intumescence process. Study of the interactions between the polymer and the additives. Journal of the Chemical Society, Faraday Transactions, **92**, 3435–3444 (1996).
DOI: 10.1039/FT9969203435

[41] Nakamizo M., Kammereck R., Walker Jr P. L.: Laser raman studies on carbons. Carbon, **12**, 259–267 (1974).
DOI: 10.1016/0008-6223(74)90068-2

[42] Tuinstra F., Koenig J. L.: Raman spectrum of graphite. The Journal of Chemical Physics, **3**, 1126–1130 (1970).
DOI: 10.1063/1.1674108

[43] Bourbigot S., Le Bras M., Delobel R., Decressain R., Amoureux J-P.: Synergistic effect of zeolite in an intumescence process: Study of the carbonaceous structures using solid-state NMR. Journal of the Chemical Society, Faraday Transactions, **92**, 149–158 (1996).
DOI: 10.1039/FT9969200149

*eXPRESS Polymer Letters Vol.4, No.12 (2010) 753–762*
*Available online at www.expresspolymlett.com*
*DOI: 10.3144/expresspolymlett.2010.91*

# Wettability transition of plasma-treated polystyrene micro/nano pillars-aligned patterns

*J. Kong*[1,2*], *K. L. Yung*[2], *Y. Xu*[2], *W. Tian*[1]

[1]Department of Applied Chemistry, School of Science, Northwestern Polytechnical University, Xi'an, 710072, P. R. China
[2]Department of Industrial and Systems Engineering, The Hong Kong Polytechnic University, Hung Hom, Kowloon, Hong Kong

*Received 30 May 2010; accepted in revised form 17 August 2010*

**Abstract.** This paper reports the wettability transition of plasma-treated polystyrene (PS) micro/nano pillars-aligned patterns. The micro/nano pillars were prepared using hot embossing on silicon microporous template and alumina nanoporous template, which were fabricated by ultraviolet (UV) lithography and inductive coupled plasma (ICP) etching, and two-step anodic oxidation, respectively. The results indicate that the combination of micro/nano patterning and plasma irradiation can easily regulate wettabilities of PS surfaces, i.e. from hydrophilicity to hydrophobicity, or from hydrophobicity to superhydrophilicity. During the wettability transition from hydrophobicity to hydrophilicity there is only mild hydrophilicity loss. After plasma irradiation, moreover, the wettability of PS micro/nano pillars-aligned patterns is more stable than that of flat PS surfaces. The observed wettability transition and wettability stability of PS micro/nano pillars-aligned patterns are new phenomena, which may have potential in creating programmable functional polymer surfaces.

***Keywords:*** *nanomaterials, patterns, nanopillars, wettability*

## 1. Introduction

Controlling the wettability of a surface has gained huge attention because wettability (hydrophobic, amphiphobic, and hydrophilic etc.) play a crucial role in many natural and industrial applications, e.g. self-cleaning, water repellency, superhydrophobic coatings, intelligent textiles, infection of medical polymers and particle attraction in deoxyribonucleic acid (DNA) purification [1–6]. A surface is hydrophilic when the water contact angle (CA) is lower than 90° and even considered as superhydrophilic when its CA is below 5°. On the other hand, the surface is hydrophobic when its CA is greater than 90°. Moreover, the surface becomes superhydrophobic when its CA is above 150°. Generally, the wettability of a solid surface is mainly caused by the chemical composition and structure asperities, which depend on surface energy and geometric structure [7].

To obtain hydrophobic polymer surfaces, coating with low surface energy materials such as fluoroalkylsilane can be helpful [8–12]. On the other hand, geometric structures including rough structures and regular micro/nano patterns are also crucial [13, 14]. To obtain polymer regular micro/nano geometric surfaces, various nanoprocessing approaches can be employed, including nanoporous template wetting [15], capillary lithography [16], nanoimprint lithography [17], microstereolithography [18], template rolling press [19], and water spreading of carbon nanotubes [20]. A number of theoretical and experimental studies indicated that

---

[*]Corresponding author, e-mail: mfkongjie@hotmail.com

polymer aligned nanopillar arrays or carbon nanotube arrays could exhibit hydrophobic or surperhydrophobic feature [21–24].

As important as enhancing hydrophobicity of polymer surfaces, controlling hydrophilicity of polymer surfaces is also an interesting issue because most polymers are hydrophobic in nature that makes them unsuitable for important biomedical and industrial applications [25]. Several surface modification techniques have been developed in order to induce polymer hydrophilic surfaces and to preserve desirable bulk properties at the same time. Wet chemical processing, plasma treatment (glow discharge, corona, and flame), and radiation treatment (ultraviolet irradiation and laser treatment) are the main surface modification techniques employed [26]. In particular, plasma treatment of polymeric materials has become one of the most important methods to enhance wettability, printability, and adhesion without affecting bulk material feature [27, 28]. However the hydrophilicity is often lost when the plasma treated surface is exposed to air again. So, one challenge lies in how to produce superhydrophilic surfaces without hydrophilicity loss or with low hydrophilicity loss during the exposure to air.

In this paper, we report the wettability transition behavior of plasma-treated polystyrene (PS) micro/nano pillars-aligned patterns. The interesting phenomena are that the combination of micro/nano patterning and plasma irradiation can easily regulate PS surfaces' wettabilities, i.e. from hydrophilicity to hydrophobicity, or from hydrophobicity to superhydrophilicity. When wettability transition from hydrophobicity to hydrophilicity occurs, there is only mild hydrophilicity loss. After plasma irradiation, moreover, the wettability of PS micro/nano pillars-aligned patterns is more stable than that of flat PS surfaces fixed with other processing conditions.

## 2. Experimental

### 2.1. Materials

PS was purchased from Sigma-Aldrich Co. (430102, average $M_w$~192 000, Germany). Micro porous silicon templates with pore diameters of 5, 10 and 20 µm were fabricated using ultraviolet (UV) lithography and subsequent inductive coupled plasma (ICP) etching in our laboratory. Nano porous anodic alumina (PAA) template with average pore diameters of 250 nm was purchased directly (Anodisc 13, Whatman International Ltd, Maidstone, UK). It is through-hole, freestanding disk with channel length of about 50 µm. PAA template with pore diameters of 100 nm was prepared by us [29]. Analytic grade chemical reagents including NaOH, ethanol and deionized water were purchased from Alfa Aesar China Co. Ltd (Tianjin, China).

### 2.2. Preparation of micro porous silicon template

To fabricate micro porous silicon template, the combined process of UV lithography and ICP etching were employed [30]. Firstly, the silicon wafer was spin coated using photoresist (BP212) and softly baked under 110°C for 1 min on a Spin Coater (CEE model 100CB, Brewer Science Co., USA). Then UV lithography processing was conducted with a deep UV Mask aligner (MA6, Suss Co., Germany). Then the designed micro porous silicon templates (5, 10, 20 µm) were obtained on the ICP machine (Multiplex Systems ASE, STS Co., UK).

### 2.3. Preparation of PS micropatterns and nanopatterns

The PS micro/nano pillars-aligned patterns were prepared using hot embossing. PS film with a thickness of 1.5 mm was put on the top of micro porous silicon template or nano porous anodic alumina template. After the machine mould cavity is closed, the temperature was raised to 130°C. Then a pressure of 0.3 MPa was applied through a hydraulic press to compress PS film and micro porous silicon template or nano porous anodic alumina template for 10 min, which allowed the PS melt to infiltrate into the pores of templates. Then, the moulds were cooled to around 80°C and the formed PS micropillars-aligned pattern was separated from micro porous silicon template by machine tension method. For the porous anodic alumina template, the formed PS nanopillars-aligned pattern were released by removing the template in NaOH solutions and rinsed thoroughly with deionized water and ethanol.

The samples were dried in an oven at 30°C for 2 days (0.02 MPa).

### 2.4. Plasma treatment of PS micro/nano pillars-aligned patterns

The PS micro/nano pillars-aligned patterns and PS original surface were treated using an air plasma instrument (PDC-32G, Harrick Plasma, USA). The input power is 100 W (220 V) and a maximum of 18 W is applied to the RF coil with no RF emission. The frequency is 50 Hz. The vacuum of 20 Pa was employed during the whole irradiation process. The distance from the sample to the top of chamber (7.62 cm diameter) is about 3.8 cm. Plasma irradiation time for all the specimens was set at 90 seconds. As comparison, the PS coating on silicon wafer was also prepared with its tetrahydrofuran solution (0.5 g/ml) on a Spin Coater (CEE model 100CB, Brewer Science Co., USA). The sample was dry in the oven at 30°C for 2 days (0.02 MPa). The plasma irradiation process is same as micro/nano pillars-aligned patterns.

### 2.5. Characterization and measurement

Micro porous silicon template, nano PAA template and the as-prepared PS micro/nano pillars-aligned patterns were characterized using scanning electron microscopy (SEM, Leica Stereoscan 440, Leica Co., Germany) and field-emission scanning electron microscopy (FE-SEM, JEOL JSM-6335F, JEOL Ltd., Japan). All samples were coated with 5 nm Au before measurements.

Water static CA was measured using a contact angle goniometer (Model 250-F1, Rame-hart Instrument Co., USA) at ambient temperature. A drop of ion-exchanged water (3 μl) was placed on the as-prepared surface using microsyringe appurtenance, then a photograph was taken with drop image

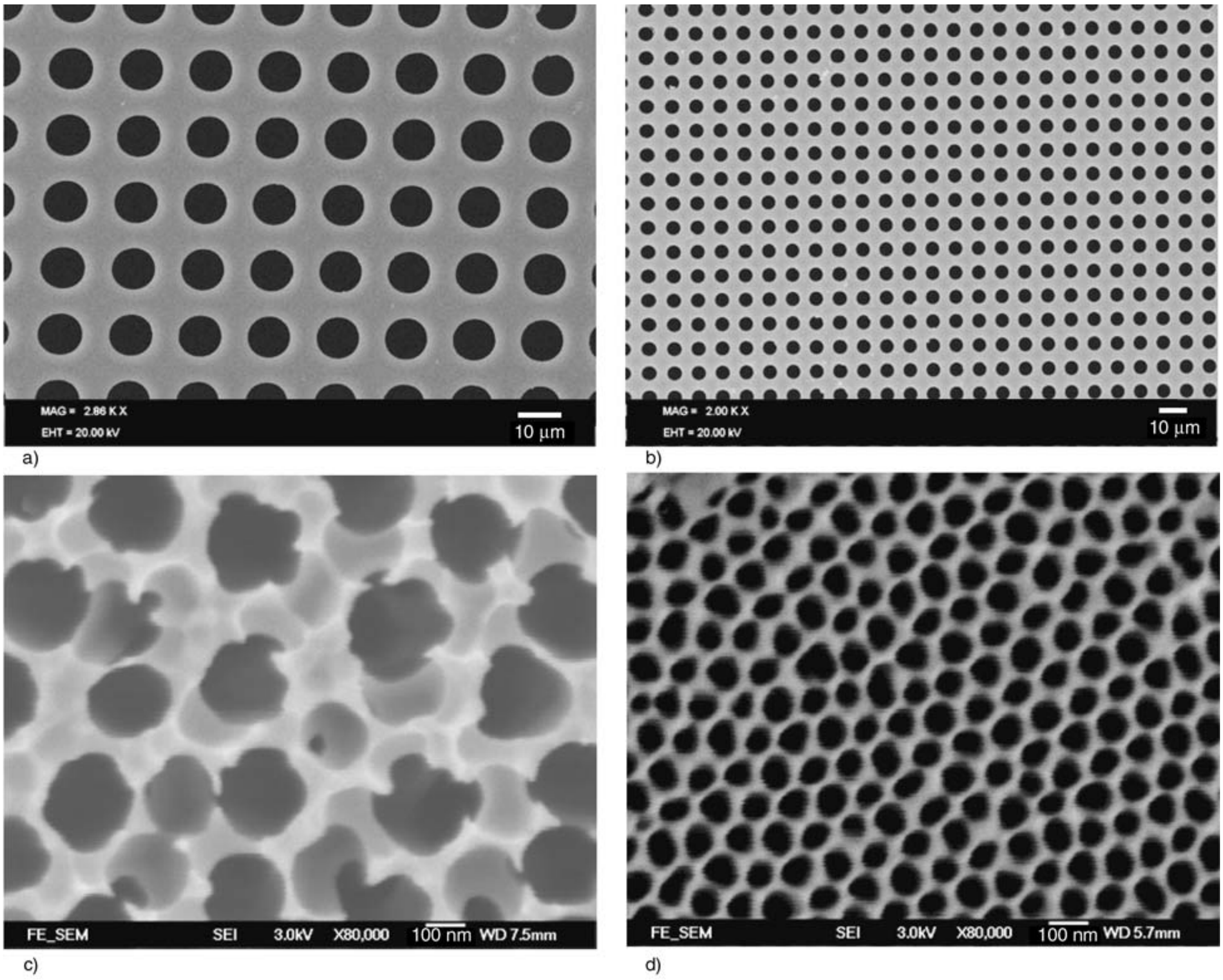

**Figure 1.** SEM images of micro and nano porous templates, (a) silicon template with pore diameter of 10 μm; (b) silicon template with pore diameter of 5 μm; (c) alumina template with pore diameter of 250 nm; (d) alumina template with pore diameter of 100 nm

Advanced 2.1 software. The contact angle was determined by fitting a Young-Laplace curve around the drop. Six parallel measurements were made for each sample, and the average contact angle was taken as the result for each surface.

## 3. Results and discussion

### 3.1. PS micro/nano pillars-aligned patterns

The microporous silicon templates were fabricated by combined process of UV lithography and ICP etching [30], and the nanoporous anodic alumina templates were prepared by the so-called two-step anodic oxidation [31, 32]. Their SEM top-view images are presented in Figure 1. In addition, the SEM cross-section images of a microporous silicon template and nanoporous anodic alumina template are shown in Figure 2.

The regular micropores with diameters of 5, 10 and 20 μm were well prepared using the combined process of UV lithography and ICP etching. The diameters of micropores are uniform with the interval space of 3, 6 and 12 μm, respectively. The depth of all the micropores is about 20 μm from its cross-section image (Figure 2a). For anodic alumina templates, average diameters of nanoporous are 100 and 250 nm, respectively. And their depth of the two templates is about 50 μm from the SEM cross-section observation (Figure 2b).

Employing these inorganic templates with high surface energy, the wetting and infiltration of PS melts into micro-/nanopores can be accomplished, which are driven by capillary force due to the high surface energy of silicon and alumina [35, 36]. When PS melts shrink after cooling to ambient temperature and templates are removed with mechanical demoulding method and NaOH solution, respectively. The generated PS one-dimensional micro/nano pillars are aligned on the residual PS bulk substrate resulting in the formation of PS micro/nano pillars-aligned patterns as shown in Figure 3. The diameter of micropillars is nearly equal to the diameter of template employed. The height of micropillars from 10 and 20 μm silicon templates is about 20 μm as similar with their depth. However, due to the damage during the mechanical demoulding (Figure 3b), the height of micropillars from 5 μm silicon template is only about 5 μm, so the aspect ratio is equal to that of micropillars from 20 μm silicon template. On the other hand, the diameter of nanopillars with height of about 45 μm (Figure 3e) is a little smaller than the diameter of template employed because the enhanced shrinkage effect on nanoscale after cooling from PS melts.

### 3.2. Wettability transition from hydrophilicity to hydrophobicity of PS micro/nano pillars-aligned patterns

To demonstrate the wettability transition behavior after the micro/nano patterning process and plasma irradiation, the static water CAs of the PS micro/nano pillars-aligned patterns are presented in Figure 4, where the corresponding water droplet shapes are enclosed.

When the PS surface is patterned with aligned micropillars with diameters of 5, 10 and 20 μm, the static water CAs without plasma treatment are

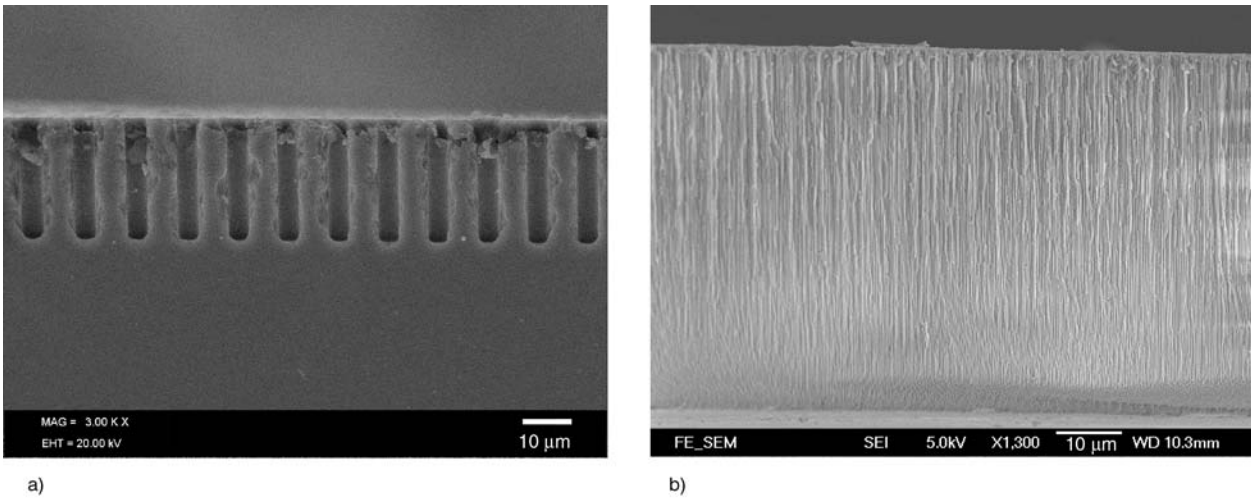

**Figure 2.** SEM images of micro and nano porous templates, (a) cross-section of silicon template with pore diameter of 5 μm; (b) cross-section of alumina template with pore diameter of 250 nm

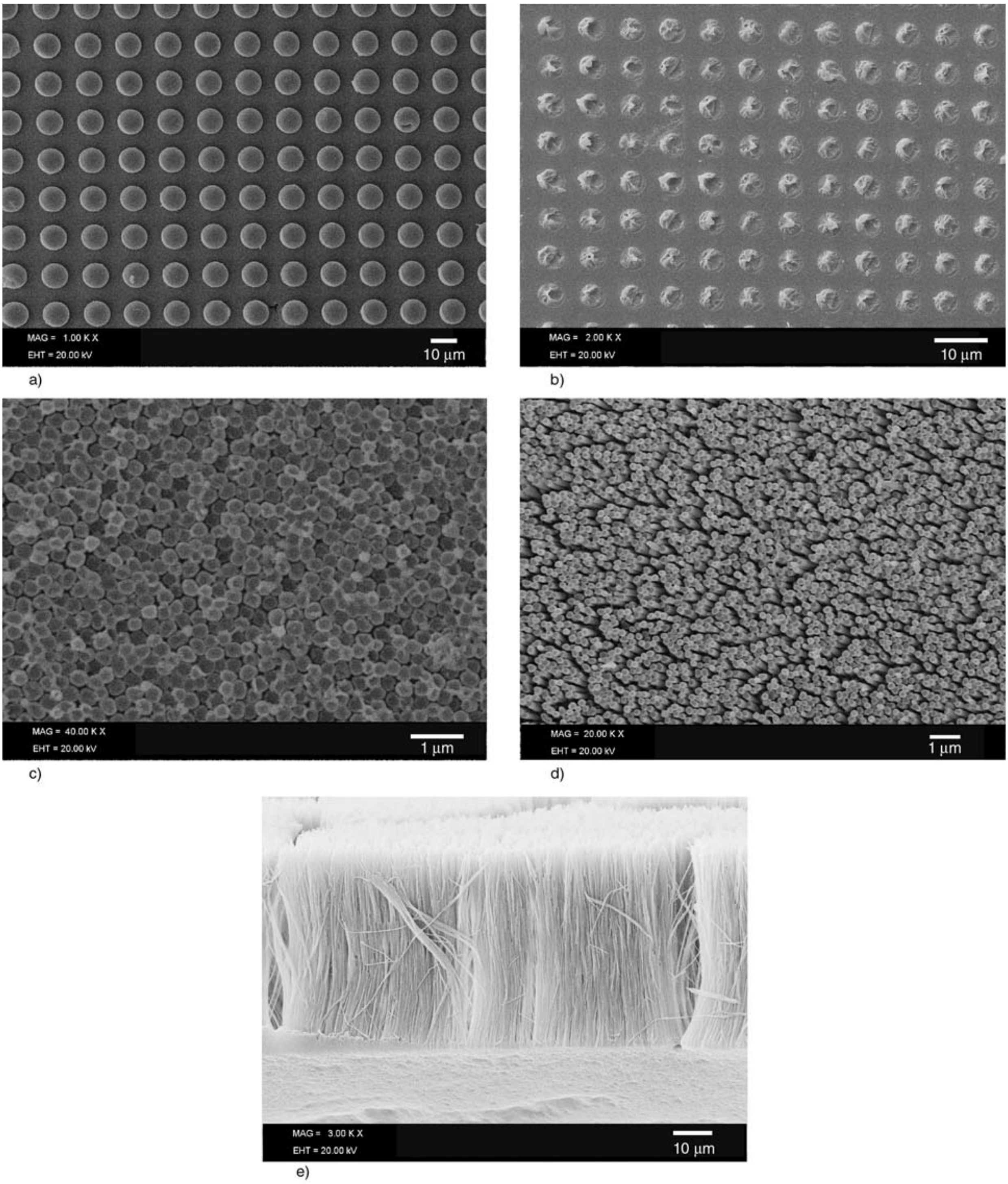

**Figure 3.** SEM images of PS micro/nano pillars-aligned patterns formed with aligned pillars with diameter of (a) 10 µm; (b) 5 µm; (c) 250 nm; (d) 100 nm; (e) cross-section of d

enhanced from 76° (PS original surface) to 101° that exhibits hydrophobicity. Similarly, when PS surface pattern is formed by the aligned nanopillars with diameter of 100 or 250 nm, the static water CAs are increased to 130° that exhibits high hydrophobicity. In a wide scale of pillar diameters from nano to micro, the wettabilities of PS micro/nano pillars-aligned patterns are changed from hydrophilicity to hydrophobicity after micro/nano patterning process. It is not surprizing because the PS surfaces are turned to be compounded rough surfaces consisting of micro/nano pillars and air [37, 38]. It is well known that the relationship between a compounded rough surface ($\theta_c$) and the equilibrium contact angle on a flat surface ($\theta_e$) can be described as the Cassie's equation (no-wetted state) [39] (Equation (1)):

$$\cos\theta_c = \Phi_s \cos\theta_e - (1-\Phi_s) \qquad (1)$$

where $\Phi_s$ is the solid-liquid contact (or solid) fraction of the surface. Compared with flat surface, the PS micro/nano pillars-aligned patterns possess the greater contact area fraction of water droplet and air on the tip of pillars and their interval on patterns, so the hydrophobicity phenomena are observed.

### 3.3. Wettability transition from hydrophobicity to hydrophilicity of PS micro/nano pillars-aligned patterns with plasma irradiation

The wettability transition from hydrophilicity to hydrophobicity of PS micro/nano pillars-aligned patterns mentioned above is not surprizing, which can be also observed on the other polymer nanopatterned surfaces, such as the polyethylene nanopatterns or self-assembled fluorosilanated monolayer structures [29, 39]. However, after only 90 seconds air plasma irradiation (200 Pa), the interesting sharp transition from hydrophobicity to hydrophilicity of PS micro/nano pillars-aligned patterns was observed as presented in Figure 4.

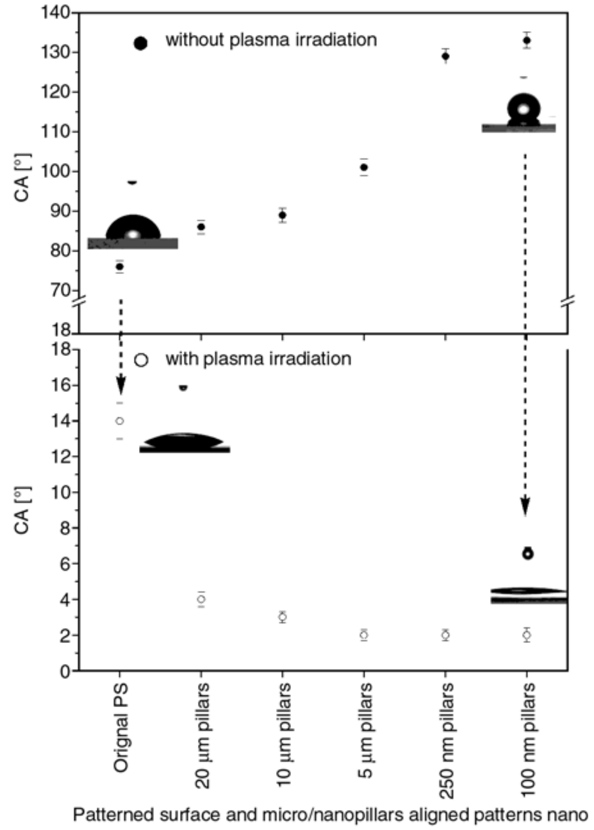

**Figure 4.** Static water contact angles of PS flat surface, micro/nano pillars-aligned patterns with and without plasma irradiation enclosed with the corresponding water droplet shape

After plasma irradiation, the PS original surface with weak hydrophilicity (CA of 76°) was transformed into a hydrophilic surface with CA of 15°. The PS coating on silicon wafer also show the similar transition (from 78 to 17°). However, the PS micro/nano pillars-aligned patterns were directly transformed from hydrophobic (CA of 101 and 130°, respectively) to superhydrophilic (CA less than 5°). That is, the PS micro/nano pillars-aligned patterns present sharp wettability transition from hydrophobicity to superhydrophilicity (from 130° to less than 5°) compared with the flat PS surface (from 76 to 15°).

For PS surface with CA of 76°, a rough surface of micro/nano pillars-aligned patterns may make it hydrophobic according to Cassie state (no-wetted state). It is well known that plasma irradiation change the chemical composition of PS surface [40–42] to lead to a slow chain scission with hydroxyl group, carboxyl group, are discussed in references in detail [26, 43, 44]. If PS surface or coating was treated using air plasma irradiation, the hydrophilic surface with CA of 15° was obtained. It indicates the water can wet PS surface according the Wenzel state (wet state). Under this condition, the water drop can diffuse along the contact surface on the tip of pillars and their interval on patterns during the static CA measurement. Compared with the PS original flat surface or coating, the high surface ratio of PS micro/nano pillars-aligned patterns enhance the diffuse effect thus resulting in the sharp transition from hydrophobicity to hydrophilicity. That is, the integrated effects of surface natural wettability and structure asperities lead to sharp transition from hydrophobicity to hydrophilicity of micro/nano pillars-aligned patterns with plasma irradiation.

### 3.4. Wettability stabilities of PS micro/nano pillars-aligned patterns after plasma irradiation

When plasma treated micro/nano pillars-aligned patterns are exposed to air, the wettability stability and durability of hydrophilicity is an important

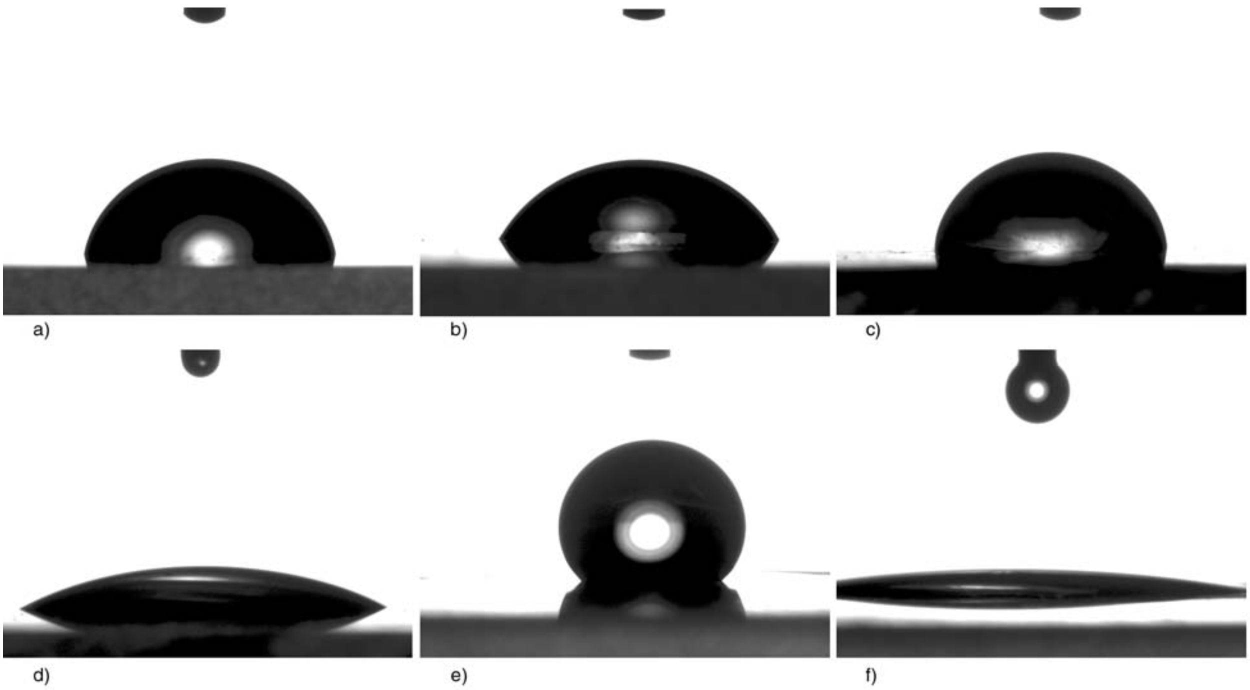

**Figure 5.** Droplet shape on PS micro/nano pillars-aligned patterns, (a) PS flat surface; (b) plasma treated PS flat surface (after 2 days); (c) PS micro pillars-aligned patterns; (d) plasma treated PS micro pillars-aligned patterns (after 2 days); (e) PS nano pillars-aligned patterns; (f) plasma treated PS nano pillars-aligned patterns (after 2 days)

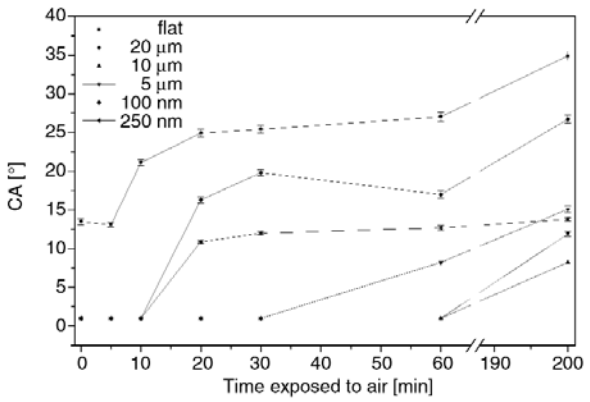

**Figure 6.** The development of water contact angles of PS micro/nano pillars-aligned patterns in a short-term after plasma irradiation

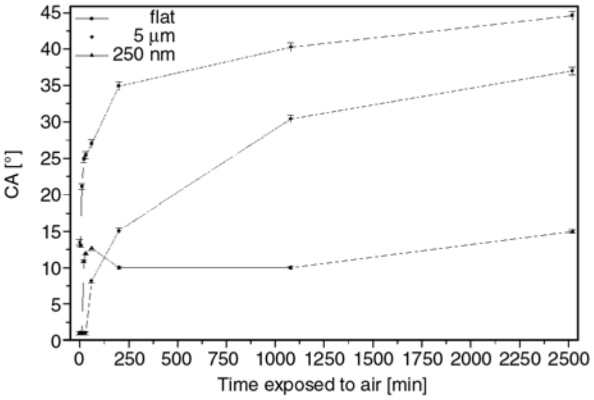

**Figure 7.** The development of water contact angles of PS micro/nano pillars-aligned patterns in a long term after plasma irradiation

issue. To investigate the wettability stability, a series of CA measurements were conducted as time going by. The droplet shapes are presented in Figure 5 and CA during the recovery process within the first 200 min and 2 days are shown in Figure 6 and Figure 7, respectively.

After being exposed to air for 2 days, the plasma treated PS micro/nano pillars-aligned patterns still exhibit obvious hydrophilicity (15–32°), while, the plasma treated PS flat surface recovers to CA of 45°. The recovery process in Figure 6 and 7 demonstrates that the hydrophilicity of micro/nano pillars-aligned patterns is more stable than that of PS flat surface no matter in 200 min recovery (short term) or in 2 days recovery (long term) after plasma irradiation. Because that chemistry change has time dependence, the hydrophilic polymer surface obtained using plasma irradiation can usually be recovered to its original wettabilty state to some degree just like the PS flat surface recovery. But for micro/nano pillars-aligned patterns with high surface ratio, the recovery is obvious lagging due to the dynamic contact angle hysteresis phenomena [39].

On the other hand, the recovery also demonstrates a little difference between micro and nano pillars-aligned patterns. After plasma irradiation, the nano pillars-aligned patterns keep on superhydrophilic state for 10 min, then CA is increased to 15° within 10 min. Comparatively, the micro pillars-aligned patterns keep on superhydrophilic state for 30 to 60 min. The CA of micro pillars-aligned patterns is below that of nano pillars-aligned patterns within the first 200 min. On the other hand, the recovery of the micro pillars-aligned patterns continue even after 2 days, while, the recovery for the nano pillars-aligned patterns turns weak after 230 min. After 230 min, the CA of the micro pillars-aligned patterns slowly exceeded that of nano pillars-aligned patterns. Since the nano pillars-aligned patterns possess higher high surface ratio than micro pillars-aligned patterns, nano pillars-aligned patterns exhibit higher stability in the long run than micro pillars-aligned patterns. The differences in the CA stability profiles between micro/nano pillars-aligned patterns and flat original surface are not only interesting, but also useful in providing new possible methods for creating programmable surfaces for particle capture and releasing in drug delivery and DNA analysis.

## 4. Conclusions

PS micro/nano pillars-aligned patterns were prepared using hot embossing on silicon microporous template and alumina nanoporous template. The combination of micro/nano patterning and plasma irradiation can easily regulate wettabilities of PS surfaces, i.e. from hydrophilicity to hydrophobicity, or from hydrophobicity to superhydrophilicity. When the wettability transition from hydrophobicity to hydrophilicity occurs, there is only mild hydrophilicity loss. And the hydrophilicity of PS micro/nano pillars-aligned patterns is more stable in 200 min and 2 days recovery than that of PS flat surfaces after plasma irradiation.

## Acknowledgements

This work was financially supported with the Aero-Science Fund of China (2009ZH53073) and the National Natural Science Foundation of China (20874080), Research Grants Council of Hong Kong (RGC, PolyU5327/07E).

## References

[1] Schulz B., Frommer W. B.: A plant ABC transporter takes the lotus seat. Science, **306**, 622–625 (2004). DOI: 10.1126/science.1105227

[2] Ma Y., Cao X. Y., Feng X. J., Ma Y. M., Zou H.: Fabrication of super-hydrophobic film from PMMA with intrinsic water contact angle below 90°. Polymer, **48**, 7455–7460 (2007). DOI: 10.1016/j.polymer.2007.10.038

[4] Liu Q. T., Zhang H., Yin S. Y., Wu L. X., Shao C., Su Z. M.: Hierarchical self-assembling of dendritic-linear diblock complex based on hydrogen bonding. Polymer, **48**, 3759–3770 (2007). DOI: 10.1016/j.polymer.2007.04.041

[5] Zhang W., Chu P. K., Jia J. H., Zhang Y. H., Fu Ricky K. Y., Yan Q.: Antibacterial properties of plasma-modified and triclosan or bronopol coated polyethylene. Polymer, **47**, 931–936 (2006). DOI: 10.1016/j.polymer.2005.12.009

[6] Chen J-K., Chan C-H., Chang F-C.: Immobilization of layered double hydroxides in the fluidic system for nanoextraction of specific DNA molecules. Applied Physics Letters, **92**, 053108/1–053108/3 (2008). DOI: 10.1063/1.2840175

[7] Ruiz A., Valsesia A., Ceccone G., Gilliland D., Colpo P., Rossi F.: Fabrication and characterization of plasma processed surfaces with tuned wettability. Langmuir, **23**, 12984–12989 (2007). DOI: 10.1021/la702424r

[8] Tsujii K., Yamamoto T., Onda T., Shibuichi S.: Super oil-repellent surfaces. Angewandte Chemie International Edition, **36**, 1011–1012 (1997). DOI: 10.1002/anie.199710111

[9] Morita M., Koga T., Otsuka H., Takahara A.: Macroscopic-wetting anisotropy on the line-patterned surface of fluoroalkylsilane monolayers. Langmuir, **21**, 911–918 (2005). DOI: 10.1021/la0485172

[10] Puukilainen E., Rasilainen T., Suvanto M., Pakkanen T. A.: Superhydrophobic polyolefin surfaces: Controlled micro- and nanostructures. Langmuir, **23**, 7263–7268 (2007). DOI: 10.1021/la063588h

[11] Kojio K., Mitsui Y., Furukawa M.: Synthesis and properties of highly hydrophilic polyurethane based on diisocyanate with ether group. Polymer, **50**, 3693–3697 (2009). DOI: 10.1016/j.polymer.2009.05.030

[12] Yi F. P., Zheng S. X.: Effect of hydrophobic polystyrene microphases on temperature-responsive behavior of poly(*N*-isopropylacrylamide) hydrogels. Polymer, **50**, 670–678 (2009). DOI: 10.1016/j.polymer.2008.11.038

[13] Nurmi L., Holappa S., Nykänen A., Laine J., Ruokolainen J., Seppälä J.: Ultra-thin films of cationic amphiphilic poly(2-(dimethylamino)ethyl methacrylate) based block copolymers as surface wettability modifiers. Polymer, **50**, 5250–5261 (2009).
DOI: 10.1016/j.polymer.2009.08.043

[14] Wang Z., Koratkar N., Ci L., Ajayan P. M.: Combined micro-/nanoscale surface roughness for enhanced hydrophobic stability in carbon nanotube arrays. Applied Physics Letters, **90**, 143117/1–143117/3 (2007).
DOI: 10.1063/1.2720761

[15] Steinhart M., Wendorff J. H., Greiner A., Wehrspohn R. B., Nielsch K., Schilling J., Choi J., Gösele U.: Polymer nanotubes by wetting of ordered porous templates. Science, **296**, 1997 (2002).
DOI: 10.1126/science.1071210

[16] Conrad P. G., Nishimura P. T., Aherne D., Schwartz B. J., Wu D., Fang N., Zhang X., Roberts M. J., Shea K. J.: Functional molecularly imprinted polymer microstructures fabricated using microstereolithography. Advanced Materials, **15**, 1541–1544 (2003).
DOI: 10.1002/adma.200304602

[17] Vogler M., Wiedenberg S., Mühlberger M., Bergmair I., Glinsner T., Schmidt H., Kley E. B., Grützner G.: Development of a novel, low-viscosity UV-curable polymer system for UV-nanoimprint lithography. Microelectronic Engineering, **84**, 984–988 (2007).
DOI: 10.1016/j.mee.2007.01.184

[18] Mata A., Fleischman A. J., Roy S.: Fabrication of multi-layer SU-8 microstructures. Journal of Micromechanics and Microengineering, **16**, 276–284 (2006).
DOI: 10.1088/0960-1317/16/2/012

[19] Guo C. W., Feng L., Zhai J., Wang G. J., Song Y. L., Jiang L., Zhu D. B.: Large-area fabrication of a nanostructure-induced hydrophobic surface from a hydrophilic polymer. ChemPhysChem, **5**, 750–753 (2004).
DOI: 10.1002/cphc.200400013

[20] Liu H., Li S. H., Zhai J., Li H. J., Jiang L., Zhu D. B.: Self-assembly of large-scale micropatterns on aligned carbon nanotube films. Angewandte Chemie International Edition, **43**, 1146–1149 (2004).
DOI: 10.1002/anie.200351988

[21] Zhang L., Zhou Z., Cheng B., DeSimone J. M., Samulski E. T.: Superhydrophobic behavior of a perfluoropolyether lotus-leaf-like topography. Langmuir, **22**, 8576–8580 (2006).
DOI: 10.1021/la061400o

[22] Lee J. A., McCarthy T. J.: Polymer surface modification: Topography effects leading to extreme wettability behavior. Macromolecules, **40**, 3965–3969 (2007).
DOI: 10.1021/ma070061i

[23] Feng L., Li S., Li Y., Li H., Zhang L., Zhai J., Song Y., Liu B., Jiang L., Zhu D.: Super-hydrophobic surfaces: From natural to artificial. Advanced Materials, **14**, 1857–1860 (2002).
DOI: 10.1002/adma.200290020

[24] Liu H., Zhai J., Jiang L.: Wetting and anti-wetting on aligned carbon nanotube films. Soft Matter, **2**, 811–821 (2006).
DOI: 10.1039/b606654b

[25] Guruvenket S., Komath M., Vijayalakshmi S. P., Raichur A. M., Rao M. G.: Wettability enhancement of polystyrene with electron cyclotron resonance plasma with argon. Journal of Applied Polymer Science, **90**, 1618–1623 (2003).
DOI: 10.1002/app.12816

[26] Chan C-M., Ko T-M., Hiraoka H.: Polymer surface modification by plasmas and photons. Surface Science Reports, **24**, 1–54 (1996).
DOI: 10.1016/0167-5729(96)80003-3

[27] Dhaya M., Parry K. L., Short R. D., Bradley J. W.: Investigating the plasma surface modification of polystyrene at low ion power densities. Journal of Physical Chemistry B, **108**, 14000–14004 (2004).
DOI: 10.1021/jp0477046

[28] Dhayal M., Forder D., Short R. D., Bradley J. W.: Electron temperature control in low-pressure plasmas using a two-mesh-separation technique. Vacuum, **70**, 67–71 (2003).
DOI: 10.1016/S0042-207X(02)00769-8

[29] Kong J., Yung K-L., Xu Y., He L., Lau K. H., Chan C. Y.: Self-organized micropatterns of high aspect ratio polymer nanofibers by wetting of nanopores. Journal of Polymer Science Part B: Polymer Physics, **46**, 1280–1289 (2008).
DOI: 10.1002/polb.21462

[30] Wang X. D., Chen Y. F., Wang L., Cui Z.: Fabrication of nanoimprint template in Si with high etch rate by non-switch DRIE process. Microelectronic Engineering, **85**, 1015–1017 (2008).
DOI: 10.1016/j.mee.2008.01.073

[31] Masuda H., Fukuda K.: Ordered metal nanohole arrays made by a 2-step replication of honeycomb structures of anodic alumina. Science, **268**, 1466–1468 (1995).
DOI: 10.1126/science.268.5216.1466

[32] Xu T. T., Piner R. D., Ruoff R. S.: An improved method to strip aluminum from porous anodic alumina films. Langmuir, **19**, 1443–1445 (2003).
DOI: 10.1021/la0264724

[33] Yung K-L., Kong J., Xu Y.: Studies on flow behaviors of polymer melts in nanochannels by wetting actions. Polymer, **48**, 7645–7652 (2007).
DOI: 10.1016/j.polymer.2007.11.013

[34] Kong J., Xu Y., Yung K. L., Xie Y. C., He L.: Enhanced polymer melts flow though nanoscale channels under vibration. The Journal of Physical Chemistry C, **113**, 624–629 (2009).
DOI: 10.1021/jp809164k

[35] Moon S. I., McCarthy T. J.: Template synthesis and self-assembly of nanoscopic polymer 'Pencils'. Macromolecules, **36**, 4253–4255 (2003).
DOI: 10.1021/ma0300239

[36] Zhang M. F., Dobriyal P., Chen J-T., Russell T. P.: Wetting transition in cylindrical alumina nanopores with polymer melts. Nano Letters, **6**, 1075–1079 (2006).
DOI: 10.1021/nl060407n

[37] Feng X. J., Jiang L.: Design and creation of superwetting/antiwetting surfaces. Advanced Materials, **18**, 3063–3078 (2006).
DOI: 10.1002/adma.200501961

[38] Jin M. H., Feng X. J., Feng L., Sun T. L., Zhai J., Li T. J., Jiang L.: Superhydrophobic aligned polystyrene nanotube films with high adhesive force. Advanced Materials, **17**, 1977–1981 (2005).
DOI: 10.1002/adma.200401726

[39] Yeh K-Y., Chen L-J., Chang J-Y.: Contact angle hysteresis on regular pillar-like hydrophobic surfaces. Langmuir, **24**, 245–251 (2008).
DOI: 10.1021/la7020337

[40] Lejeune M., Lacroix L. M., Brétagnol F., Valsesia A., Colpo P., Rossi F.: Plasma-based processes for surface wettability modification. Langmuir, **22**, 3057–3061 (2006).
DOI: 10.1021/la052515f

[41] Arpagaus C., Rossi A., von Rohr P. R.: Short-time plasma surface modification of HDPE powder in a Plasma Downer Reactor – Process, wettability improvement and ageing effects. Applied Surface Science, **252**, 1581–1595 (2005).
DOI: 10.1016/j.apsusc.2005.02.099

[42] Sanchis R. M., Calvo O., Sánchez L., García D., Balart R.: Enhancement of wettability in low density polyethylene films using low pressure glow discharge $N_2$ plasma. Journal of Polymer Science Part B: Polymer Physics, **45**, 2390–2399 (2007).
DOI: 10.1002/polb.21246

[43] Idage S. B., Badrinarayanan S.: Surface modification of polystyrene using nitrogen plasma. An X-ray photoelectron spectroscopy study. Langmuir, **14**, 2780–2785 (1998).
DOI: 10.1021/la9711286

[44] Di Mundo R., Palumbo F., d'Agostino R.: Nanotexturing of polystyrene surface in fluorocarbon plasmas: From sticky to slippery superhydrophobicity. Langmuir, **24**, 5044–5051 (2008).
DOI: 10.1021/la800059a

*eXPRESS Polymer Letters Vol.4, No.12 (2010) 763–772*
*Available online at www.expresspolymlett.com*
*DOI: 10.3144/expresspolymlett.2010.92*

# Electrospun water soluble polymer mat for ultrafast release of Donepezil HCl

*Zs. K. Nagy*[1*]*, K. Nyúl*[1]*, I. Wagner*[1]*, K. Molnár*[2]*, Gy. Marosi*[1]

[1]Budapest University of Technology and Economics, Faculty of Chemical Technology and Biotechnology, Department of Organic Chemistry and Technology, 1111 Budapest, Budafoki út 8., Hungary
[2]Budapest University of Technology and Economics, Faculty of Mechanical Engineering, Department of Polymer Engineering, 1111 Budapest, Műegyetem rkp. 3., Hungary

*Received 18 May 2010; accepted in revised form 18 August 2010*

**Abstract.** Electrostatic spinning (Electrospinning, ES) was applied to prepare Donepezil HCl loaded nanofibers as a potential orally dissolving dosage form. Electrospinning of water solutions of different polymers were performed in order to fabricate a consistent and removable web on the collector with ultra-fast dissolution in water based media. Poly(vinyl-alcohol) of low molecular weight was found to be the most appropriate for this purpose. Morphology of the prepared nanofibers was characterized by scanning electron microscope as a function of viscosity and drug content. Diameters of the fibers were between 100 and 300 nm with narrow distribution. *In vitro* drug release of the webs was immediate (less than 30 s) after immersion independently of their drug content owing to the formed huge surface area, while cast films with the same compositions and commercial tablets needed 30 min or more for complete dissolution. The developed technology for the preparation of orally dissolving web (ODW) formulations is a promising way for producing effective and acceptable dosage forms for children, older people and patients with dysphagia.

***Keywords:*** *nanomaterials, electrospinning, drug delivery, orally dissolving web (ODW), ultrafast dissolution*

## 1. Introduction

Peroral administration of APIs (Active Pharmaceutical Ingredients) is the most preferred route in drug therapy especially if the patient compliance aspects are considered. Peroral delivery includes orally dissolving dosage forms, which are in the focus of numerous industrial research and development activities owing to their advantages such as:

- instant drug release and rapid onset action (e.g. against migraine);
- site-specific effect (e.g. sore throat);
- buccal adsorption, avoidance of first pass effect;
- improved oral bioavailability;
- acceptable for patients with swallowing difficulties (e.g. dysphagia, pediatric or geriatric patient, mental disorders, emesis, motion sickness);
- not requiring mastication or water;
- chance for reformulation of existing drugs (product life-cycle management, market competition).

More traditional oral formulations such as syrups and drops have some considerable disadvantages. Stability of drugs in liquids is generally much less than in solid forms due to the higher reactivity of substances in liquid phase [1]. Furthermore, the dose precision of liquid formulations is mostly imperfect. These disadvantages led the European Medicines Agency (EMEA) to recommend the development of solid dosage forms instead of oral liquid dosage forms [2].

The orally disintegrating tablet formulation (ODT) [3] meets the EMEA recommendation. Administration of ODTs is easy and there is no need to swal-

---

[*]Corresponding author, e-mail: nagyzsomborkristof@gmail.com

low large particles or water. The required disintegration time of ODTs has to be less than 30 s which needs much care during the manufacturing. Compression force and hardness of the tablet are critical parameters of manufacturing of ODTs. If the compression force is too high the disintegration time increases over the established limit. In contrast, if the compression force is low the mechanical properties of the tablet will be weak, leading to fragile and brittle tablets of weak resistance against mechanical shocks during manufacturing, storage, packaging, transportation and intake. Another type of ODTs produced by freeze-drying is often very porous, brittle and fragile.

The most recent researches in the field of orally dissolving solid dosage forms have been dealing with oral thin film technology (OTF) which is a relatively new area of interest regarding the oral administration. The first commercial success of oral thin films appeared in the United States (Listerine PocketPaks). Nowadays several products, manufactured by this technology, reached the market or are in the clinical phase of development (Listerine PocketPaks, BioEnvelop, MonoSol Rx, BioFilm, Snoreeze, Triaminic, RapidFilm [4], Ora-Film [5]).

OTFs have some advantages over ODTs. The mechanical properties of the films are better than those of ODTs due to their flexibility. OTFs have higher surface to contact with the saliva and the dissolution can be faster. However oral thin films often contain ingredients insoluble in water such as microcrystalline cellulose to promote disintegration. Insoluble particles can be inconvenient for patients and furthermore they have to be swallowed.

Electrostatic spinning (Electrospinning, ES) is a dynamically developing technology which has been primarily applied in the textile/filtration industry. The ES technology is based on the impact of high electric field on polymer solutions generating polymer fibers in the submicron scale when the electric forces overcome the surface tension. The setup consist of a solution feeder and a high voltage power supply which is connected to a spinneret and a collector electrode. Usually the latter one is grounded. The solution on the spinneret electrode forms a droplet which can interact with electrostatic field. The droplet gains a cone-shape and thin jet can emerge from the tip of the cone. Fibers are drawn by electrostatic forces between the two electrodes and the solvent evaporates, resulting in solid nanofibers. The prepared non-woven web is removable from the grounded collector as a sheet. There are numerous promising research activities in various relevant areas such as composites [6–11], sterile filtration [12], wound dressing [13, 14], wound healing [15], tissue engineering [16–19] and semiconductors [20]. This technique is relatively new in the field of medical industry and ES is quite slightly known in pharmaceutical technology, where most of the relevant papers deal with sustained drug release [21]. Immediate release from nonwoven system of electrospun nanofibers (called mat or web generally) has been published only in some cases [22–25]. Consequently the reviews dealing with fast dissolving oral dosage forms such as OTFs, and ODTs missed to mention this technology [3, 5, 26–28].

Formation of non-woven tissues of the nanofibers, owing to their huge surface area, is a promising way to develop oral fast-dissolving dosage forms and the electrostatic spinning can be a capable technology for manufacturing such formulations. The wide versatility of the polymers available for this purpose supports this idea. Papers dealing with immediate release from electrospun mat applied organic solvents during their electrospinning process [22–25].

The aim of this work was to investigate applicability of organic solvent free electrostatic spinning method to produce orally dissolving formulation (ODW = Orally Dissolving Web) using a water soluble model drug. Donepezil HCl, administered against Alzheimer's disease, was chosen as an example because its ODT formulation is available on the market (Aricept ODT, Eisai) and its OTF formulation, developed using Rapidfilm technology (LabTec), is under clinical testing.

## 2. Materials and methods

### 2.1. Materials

The model drug Donepezil HCl (Figure 1) was kindly provided by Richter Plc (Budapest, Hungary).

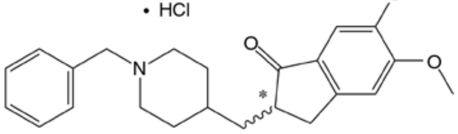

**Figure 1.** Chemical structure of Donepezil HCl

Poly(vinyl-alcohol) ($M_w$ = 31 000 Da), purchased from Fluka (Buchs, Switzerland), PVA-PEG graft copolymer of Kollicoat IR type (BASF, Ludwigshafen, Germany) and Pharmacoat 606 HPMC hydroxypropylmethylcellulose (Shin-Etsu, Tokyo, Japan), were used as polymer matrices.

## 2.2. Preparation of solutions

The polymer was added into 10 ml purified water and stirred by ARE magnetic stirrer (VELP Scientifica, Usmate, Italy) at 600 rpm and 50°C till the complete dissolution. The API was dissolved in the solution of the polymer (magnetic stirrer, 600 rpm, 25°C). The compositions of PVA based solutions are presented in Table 1.

**Table 1.** Composition of PVA based solutions

| Samples | | PVA | Water | Do |
|---|---|---|---|---|
| Number | Referred as | [g] | [ml] | [g] |
| 1 | PVA 10% | 1.11 | 10 | 0 |
| 2 | PVA 15% | 1.76 | 10 | 0 |
| 3 | PVA 20% | 2.50 | 10 | 0 |
| 4 | PVA:Do 5:1 | 2.50 | 10 | 0.50 |
| 5 | PVA:Do 2:1 | 2.50 | 10 | 1.25 |

## 2.3. Electrostatic spinning process

The electrostatic spinner used for the experiments was equipped with NT-35 High Voltage DC Supply (MA2000, Nagykanizsa, Hungary). The utilized electrical potential on the spinneret electrode was between 10–35 kV which was adjusted during the experiments. A grounded aluminium plate covered with aluminium foil or thin PVA film was used as collector. The distance of the spinneret and the collector was 15 cm and the experiments were performed at room temperature (25°C). Polymer solutions were dosed by SEP-10S Plus syringe pump (Aitecs, Vilnius, Lithuania). Electrospinning process was repeated 2 times to investigate the repeatability in the case of the drug containing compositions. Samples (equivalent to 10 mg Donepezil HCl) were cut from 3 different places of the collected web and were assayed by dissolution test. The weights of the cut PVA:Do 5:1 and PVA:Do 2:1 samples were ~60 and ~30 mg, respectively.

## 2.4. Rheological measurements

Viscosity of the solutions was determined by AR 2000 Rotational Rheometer (TA Instruments, New Castle, USA) in a parallel plate configuration. The upper moved portion was a 40 mm diameter stainless steel plate. The lower portion was a Peltier plate covered by Teflon and the applied gap between the plates was 0.5 mm. The temperature of the solutions was adjusted to 25°C by the Peltier thermoelement. The viscosities were measured at torques increased logarithmically from 10 to 1000 μNm·Pa. The viscosities shown in the Table 2 are the average of 10 measured values at different torques (no significant changes were estimated as a function of the torque).

## 2.5. Conductivity tests

Conductivity of the solutions was measured using a Radelkis OK-102/1 conductivity meter (Radelkis, Budapest, Hungary). The electrode was immersed into the solution and the measurement was carried out at 25°C. The results given in Table 2 represent the average of 3 parallel measurements.

## 2.6. Scanning electron microscopy (SEM)

Morphology of the samples was investigated by a JEOL 6380LVa (JEOL, Tokyo, Japan) type scanning electron microscope. Each specimen was fixed by conductive double sided carbon adhesive tape and sputtered by gold (using JEOL 1200 instrument) in order to avoid electrostatic charging.

**Table 2.** Viscosity and conductivity of the solutions at 25°C

| Sample | Viscosity [Pa·s] (n=10) | Standard deviation [Pa·s] | Conductivity [mS/cm] (n=3) | Standard deviation [mS/cm] |
|---|---|---|---|---|
| Water | 0.00088 | 0.00026 | 0.023 | 0.002 |
| PVA 10% | 0.02590 | 0.00140 | 0.760 | 0.050 |
| PVA 15% | 0.10900 | 0.00800 | 0.940 | 0.040 |
| PVA 20% | 0.39500 | 0.01500 | 1.040 | 0.060 |
| PVA:Do 5:1 | 0.40900 | 0.01100 | 3.700 | 0.110 |
| PVA:Do 2:1 | 0.52100 | 0.01700 | 7.500 | 0.110 |

## 2.7. Film casting

Donepezil HCl containing PVA films (PVA:Do 5:1 and 2:1) were also prepared by casting method to compare the dissolution rate of electrospun mats and cast films. PVA was dissolved in purified water with magnetic stirrer at 50°C and 600 rpm (ARE Magnetic Stirrer, VELP Scientifica, Usmate, Italy). After the complete dissolution of the polymer Donepezil HCl was added into the solution at room temperature (25°C). Then the solution of the polymer and the drug was cast into square silicone moulds (4×100×100 mm). After evaporation of the water (room temperature, 3 days) the films were removed and stored at room temperature. The thicknesses of the prepared films were between 100 and 110 μm measured by Pro-Max electronic digital caliper (NSK, Tokyo, Japan). For dissolution tests squared films were cut equivalent to 10 mg Donepezil HCl.

## 2.8. *In vitro* drug dissolution measurement

The dissolution studies were performed by Erweka DT6 dissolution tester (USP II apparatus, Erweka, Heusenstamm, Germany). 3-3 samples were investigated from the two parallel electrospinning process in the cases of PVA:Do 5:1 and PVA:Do 2:1. Electropun samples to 10 mg Donepezil HCl were placed in the dissolution vessel containing 900 ml distilled water maintained at 37±0.5°C and stirred at 50 rpm. Samples (5 ml) were collected after 0.5, 1, 1.5, 2, 2.5, 5, 10, 15, 20 and 30 minutes and were analyzed by Hewlett-Packard HP 8452A UV-VIS spectrophotometer (Palo Alto,USA) using diode array detector at 272 nm. Concentration of Donepezil HCl in the collected samples could be easily calculated with the help of the calibration curve of pure Donepezil HCl in water (since PVA has no detectable absorbance at this wavelength).

For comparison 3 parallel samples of cast films (10 mg Donepezil HCl) with same composition as electrospun samples and six commercial Aricept peroral tablets (10 mg Donepezil HCl) were assayed. The collected liquid samples were filtrated through 0,22 μm membrane in the case of tablets.

## 2.9. Modeling oral dissolution

5 ml purified water was poured in a Petri dish ($d$ = 5 cm). Electrospun samples were placed onto the surface of the water by a clip. The weight of the samples was ~60 mg for electrospun PVA placebo, while ~30 and ~60 mg for electrospun PVA:Do 2:1 and electrospun PVA:Do 5:1 respectively. Dissolution (disappearance) was investigated visually and the time of disappearance was measured. Six parallel assays were carried out on each composition (electrospun PVA placebo, electrospun PVA:Do 5:1 and electrospun PVA:Do 2:1).

*In vivo* dissolution (disappearance) test was also performed by electrospun PVA placebo. Electrospun samples (60 mg) were placed onto the tongue of a volunteer and the time of disappearance of the web was measured. Six parallel tests were performed.

## 3. Results and discussion

### 3.1. Selection of the polymer

Different polymers were applied to prepare adequate web for fast dissolution. The compared polymers were as follows: PVA, HPMC, PVA-PEG graft copolymer. The first characteristic of these polymers to be taken into consideration was their solubility and dissolution. For the purposes of present application the polymer has to be soluble in the water based medium of salvia and the dissolution time has to be as short as possible. The polymers applicable for pharmaceutical purposes are quite limited due to the stringent regulations. Several water soluble and insoluble polymers are applied by filmcoating technology, which is a rapidly developing part of pharmaceutical industry. In the most cases tablet coatings have to dissolve rapidly to avoid any delay in the action of APIs. Thus polymer components of fast dissolving filmcoatings are good candidates to develop orally dissolving systems.

Donepezil HCl has appropriate water solubility therefore the preferred solvent for electrospinning was pure water. Sequences of polymer water solutions of different concentrations were tested by the electrospinning apparatus. It was found that the selected type of cellulose derivate (see in the 2.1) is not adaptable for preparing suitable web for oral dissolution at any concentration in water. The experiments performed by water solutions of PVA-PEG graft copolymer were more successful but separated non fibrous particles were found as a result on the collector when the concentration was

≤ 20 w/w%. (At higher concentration there was not any utilizable material on the collector.) In the case when separated particles are formed instead of fibers the method is called electrospraying. With this process fine particles are readily producible but it is not the subject of this paper.

PVA solutions resulted promising fibrous web at various concentrations therefore further investigations were performed using PVA-based systems.

### 3.2. Morphology of the electrospun poly(vinyl-alcohol) webs

The morphology of the electrospun products as a function of the concentration of the polymer solution was examined by SEM. Varying the concentration of PVA solution in course of the electrospinning process beaded-fibers were gained at 10 w/w% while at higher concentrations (15, 20%) fibers of different thickness were formed owing to the increased viscosity and higher entanglement of the polymer chains. The concentration of 20 w/w% was found to be optimal for getting stabile structure of discrete fibres (Figure 2).

The structure shown in Figure 2c was expected to be important both from the diffusion and dissolution point of view. The drug diffusion in solid polymer matrix and consequently its crystal-growing process can be hindered, keeping them in nanocrystal range, when the discrete fibers are obtained. (No three-dimensional diffusion can occur.) Concerning the dissolution it was expected that not only faster dissolution rate of nanocrystals, enclosed in the fibers, can be achieved (owing to the higher surface area), but the total solubility can be higher as well comparing to large particles. The chance for it is based on the enhanced angle of curvature of the fine fibers resulting in higher surface energy, which in turn modifies the equilibrium solubility. (The particle size effect on the solubility is significant in the nanorange, while above several microns it is negligible.) Enhanced solubility influences the bioavailability of the drug substantially.

Diameter of the fibers and the beads was determined by the aid of the software provided by the SEM analyzer. Particle size of the beads was around 1 μm (see in Figure 2a) and the diameter of the fibers was in the range of hundred nanometers.

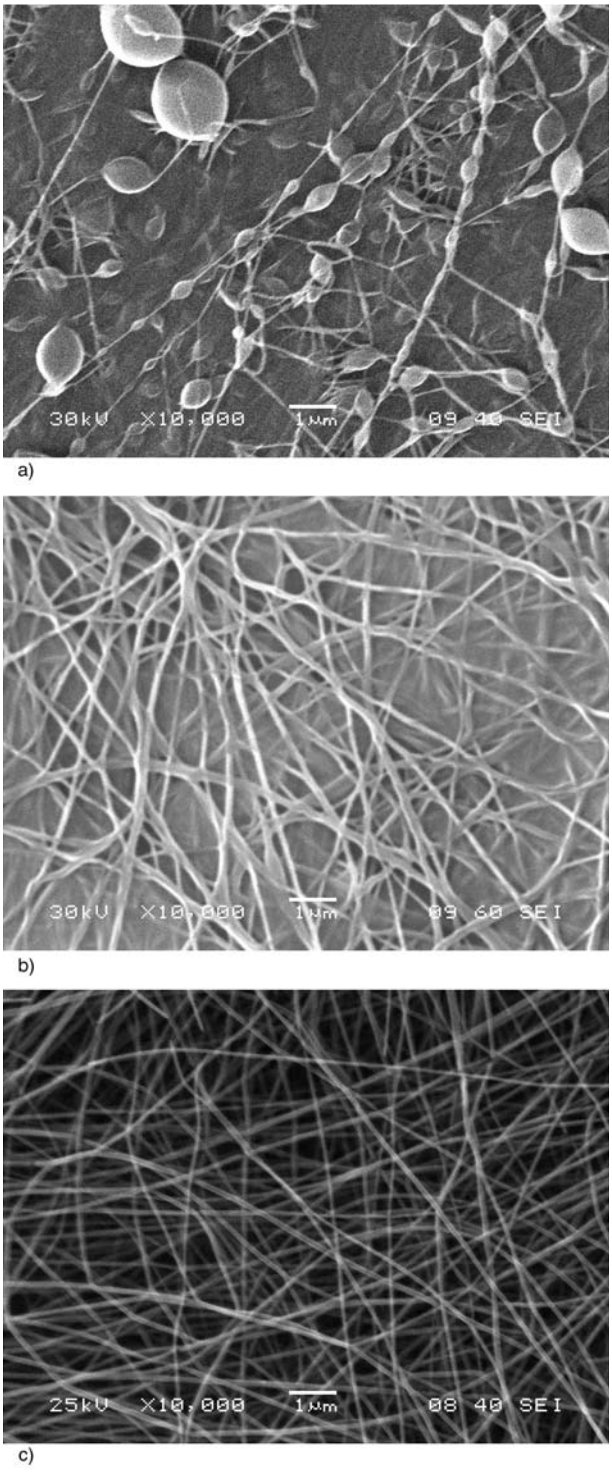

**Figure 2.** Scanning electron microscopic (SEM) images of PVA water solutions (magnification: 10 000×): a) PVA 10%, b) PVA 15%, c) PVA 20%

The mean fiber diameter of the electrospun PVA 20 w/w% solution was between 100–130 nm according to Figure 3. These very thin fibers have huge enough surface area to increase the dissolution rate significantly.

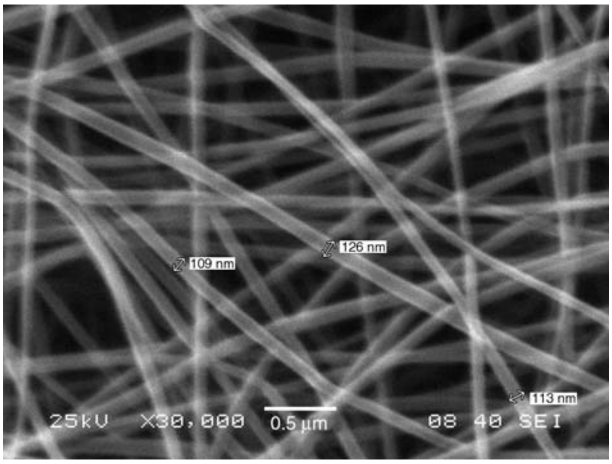

**Figure 3.** Scanning electron microscopic image of electrospun PVA 20% water solution (magnification 30 000×)

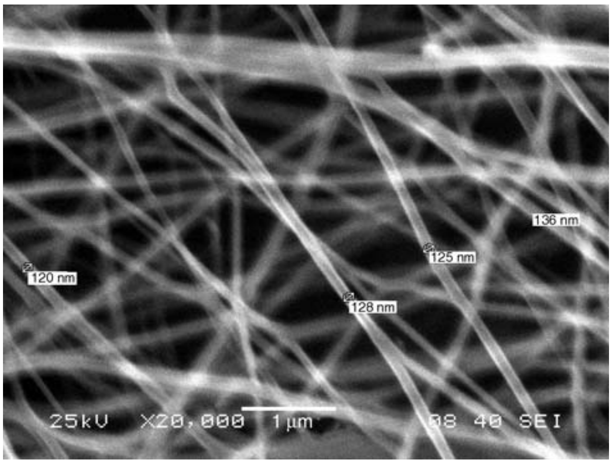

**Figure 4.** Scanning electron microscopic image of electrospun PVA:Do 5:1 (magnification 20 000×)

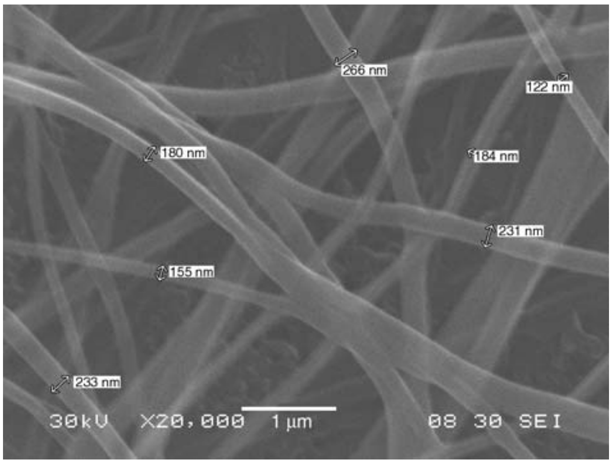

**Figure 5.** Scanning electron microscopic image of electrospun PVA:DO 2:1 (magnification 20 000×)

### 3.3. Morphology of the drug-containing electrospun fibers

Addition of Donepezil HCl (PVA:Do, 5:1) into the solution of PVA does not have significant effect on the technology and on the diameter. The mean diameter was between 100–150 nm (Figure 4). When the polymer drug ratio was increased up to 33 w/w% (PVA:Do, 2:1) the diameter of the electrospun fibers increased slightly, but it still not exceeding the 300 nm (Figure 5).

### 3.4. Rheology and conductivity of solutions

The entanglement of PVA chains depends on the PVA concentration of the aqueous solutions, which consequently determines its rheological behaviour during the electrospinning process. Addition 10 and 20 w/w% of PVA into water leads to 30 and 450 times higher viscosity respectively than the viscosity of pure water (Table 2). At low polymer concentration (≤10 w/w%) there is not enough entanglement between the polymer chains for increasing the viscosity and thus maintaining a uniform fiber stream that is the reason why beads or beaded fibers are formed during the electrostatic spinning [29]. Increased entanglement of PVA chains and consequently increased viscosity in the case of ~20 w/w% concentration results in stable fibrous morphology.

The viscosity of PVA 20% solution was not affected significantly by addition 4 w/w% Donepezil HCl and diameters of electrospun fibers did not changed noticeably. (Donepezil HCl of 4w/w% in the solution means (after the evaporation of water) ~16.7 w/w% in the solid electrospun product.) Increasing the Donepezil HCl concentration up to 10 w/w% in the PVA-water solution (33 w/w% in the solid product) leads to slightly increased viscosity and somewhat enlarged fiber thickness. It is concluded that the presence of the small Donepezil HCl molecules has a minor effect on the viscosity in this range of concentration.

However, the effect Donepezil HCl from the point of view of the conductivity is considerable. Addition of Donepezil HCl into the PVA solution increased the conductivity significantly as given in Table 2. Baumgarten [30] found that increasing of conductivity of the acrylic polymer solution decreased the diameter of fibers due to the stronger interaction between the solution and the electric field. However, according to our finding, the increased conductivity raised the viscosity of the solution slightly and the viscosity (and increased dry solid content) influenced the diameter of fibers more significantly than the effect of increased conductivity.

### 3.5. Drug dissolution investigation

The prepared drug loaded samples of described morphology were considered promising for oral dissolution because of good water solubility of the applied fiber-forming polymer and the huge surface of the formed fibers. PVAs of high molecular weight were applied earlier in electrospinning for controlling and sustaining drug release through gel formation [31]. However, in this work the instant dissolution was the aim therefore PVA of low molecular weight (31 000 Da) was selected having moderate tendency for gel formation.

Figures 6 and 7 show the drug release profiles of electrospun webs, cast films with the same composition and commercial tablets. (Data of the samples from the two parallel electrospinning processes are represented in one plot because there were no significant differences between the samples collected from these processes.)

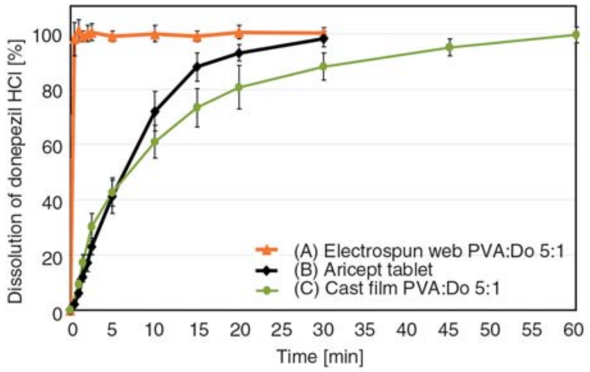

**Figure 6.** *In vitro* dissolution of Donepezil HCl (dose 10 mg, 900 ml distilled water, 50 rpm, 37°C): (A) Electrospun web of PVA-Do ratio 5:1 (*n* = 6), (B) Commercial Aricept tablet (dose 10 mg, *n* = 6), (C) Cast film of PVA-Do ratio 5:1 (*n* = 3)

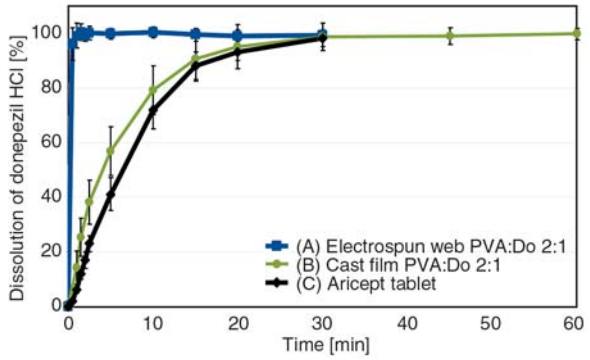

**Figure 7.** *In vitro* dissolution of Donepezil HCl (dose 10 mg, 900 ml distilled water, 50 rpm, 37°C): (A) Electrospun web of PVA-Do ratio 2:1 (*n* = 6), (B) Cast film of PVA-Do ratio 2:1 (*n* = 3), (C) Commercial Aricept tablet (dose 10 mg, *n* = 6)

The considerable difference between the rates of dissolution of different samples is well recognizable.

Dissolution of cast films was dependent of their drug content. Drug release of PVA:Do 2:1 cast films was significantly faster than that of PVA:Do 5:1. Probably Donepezil HCl as a small molecule with good water solubility can get easily into the solution phase, while PVA as a macromolecule dissolves slower if its long polymer chains are less plasticized by the drug molecules allowing larger extent of entanglement, inter- and intramolecular H-bonds. It means that PVA has retardant effect excepting the case when formation of extremely huge surface area decreases the value of bulk of entangled structure.

The electrospun webs, independently of their drug concentration, were dissolved immediately after immersion in dissolution media owing to the formed huge surface area. The correlation of surface area and dissolution rate, corresponding to the Noyes and Whitney equation [32], is described by Equation (1):

$$\frac{\mathrm{d}C}{\mathrm{d}t} = \frac{D\cdot A\cdot(C_s - C_t)}{h\cdot V} \tag{1}$$

where d$C$/d$t$ is the dissolution rate, $D$, the diffusion coefficient, $A$, the surface area exposed to the dissolution media, $h$, the diffusion layer thickness, $V$, the volume of the dissolution media, $C_s$, the saturation solubility of the drug and $C_t$, the drug concentration at time $t$.

The equation shows that the dissolution rate is directly proportional to the surface area exposed to the dissolution media.

Modeling of oral dissolution of electrospun webs showed similar results as the standard USP II dissolution method. The disappearance time of the samples was 13±6 s, 11±4 s, 6±3 s for electrospun PVA placebo, electrospun PVA:Do 5:1 and electrospun PVA:Do 2:1, respectively. Time of disappearance increased slightly in the function of decreasing drug content but all electrospun samples fulfilled the requirement of fast dissolution (<30 s). *In vivo* assays were carried out using electrospun PVA placebo which had the longest dissolution time of electrospun samples. The average disappearance time of the webs on the volunteers tongue was 9±6 s. The obtained results confirmed the possible applicability of electrospun PVA webs for oral dissolving dosage forms.

Electrospinning provides a very effective tool to increase the surface area and thus speed up the dissolution rate. Future perspectives of the way of administration of electrospun webs are considered quite wide. Owing to the variability of electrospinning process the physical properties of the electrospun web can be tailored to the requirements of certain applications. If it has proper physical behaviors (tensile strength, rigidity, … etc.) it can be used simply by cut out the area of adequate dosage from non-woven fabric produced. In all cases the uniform thickness of the web has to be ensured. Another possibility is application of a flat biocompatible solid carrier which can be the collector during the electrospinning. It can be conductive or non-conductive material as well. For demonstration PVA film ($M_w$ = 31 000 Da) plasticized with polyethyleneglycol (PEG, $M_w$ = 4000 Da) was used as collector during the electrospinning and the obtained double-layer structure was easy to handle and could be administered readily (Figure 8).

For industrial application of orally dissolving webs larger scale production has to be available. Scaling-up of electrospinning process is in the focus of several researches. Nowadays there are some promising systems available, such as Nanospider technology (Elmarco, Czech Republic). The 10 kg/day PVA web production capacity of this method means more than 100 000 units/day (if the dosage is 10 mg and one drug unit is 100 mg), which can fulfill the requirements of the pharmaceutical industry.

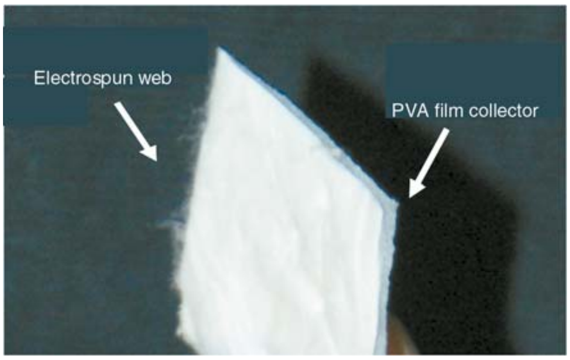

**Figure 8.** Image of nanofibrous web (PVA:Do 5:1) electrospun onto PVA film

## 4. Conclusions

Orally dissolving drug delivery systems have increasing attention in industrial and academic field too. Donepezil HCl, administered generally against Alzheimer's disease, was introduced into PVA solution and fabricated to nanofibers by electrospinning. Owing to the formed huge surface area the drug release was found immediate from the fibers. The developed method needs very low energy input and works at ambient temperature. This technology might be suitable for industrial scaling up owing to the recent rapid development of industrial electrospinning technology mainly in the textile and filtration industry [33]. The prepared PVA based nanofibrous orally dissolving web (ODW) formulation is a promising way for producing acceptable and effective dosage forms for children, older people, patients with dysphagia and so on.

## Acknowledgements

The authors would like to express their thanks to the OTKA Research Fund (code K76346), ERA Chemistry (code NN 82426), W2Plastics EU7 Project (code 212782), and the Hungarian research project TECH_08-A4/2-2008-0142. for the financial support received. This work is connected to the scientific program of the 'Development of quality-oriented and harmonized R+D+I strategy and functional model at BME' project. This project is supported by the New Hungary Development Plan (Project ID: TÁMOP-4.2.1/B-09/1/KMR-2010-0002).

## References

[1] Florence A. T., Attwood D.: Drug stability. in 'Physicochemical principles of pharmacy' (eds.: Florence A. T., Attwood D.) Pharmaceutical Press, London, 93–138 (2006).

[2] European Medicines Agency, Committee for Medicinal Products for Human Use: Reflection paper: Formulation of choice for the pediatric population (2006). (http://www.emea.europa.eu/pdfs/human/paediatrics/19481005en.pdf).

[3] Hirani J. J., Rathod D. A., Vadalia K. R.: Orally disintegrating tablets: A review. Tropical Journal of Pharmaceutical Research, **8**, 161–172 (2009).

[4] Reiner V., Giarratana N., Monti N. C., Breintenbach A., Klaffenbach P.: Rapidfilm®: An innovative pharmaceutical form designed to improve patient compliance. International Journal of Pharmaceutics, **393**, 55–60 (2010).
DOI: 10.1016/j.ijpharm.2010.03.055

[5] Dixit R. P., Puthli S. P.: Oral strip technology: Overview and future potential. Journal of Controlled Release, **139**, 94–107 (2009).
DOI: 10.1016/j.jconrel.2009.06.014

[6] Chang Z. J., Zhao X., Zhang Q. H., Chen D. J.: Nanofibre-assisted alignment of carbon nanotubes in macroscopic polymer matrix via a scaffold-based method. Express Polymer Letters, **4**, 47–53 (2010).
DOI: 10.3144/expresspolymlett.2010.8

[7] McCullen S. D., Stevens D. R., Roberts W. A., Ojha S. S., Clarke L. I., Gorga R. E.: Morphological, electrical and mechanical characterization of electrospun nanofiber mats containing multiwalled carbon nanotubes. Macromolecules, **40**, 997–1003 (2007).
DOI: 10.1021/ma061735c

[8] Farikov S.: Towards nanofibrillar single polymer composites. Express Polymer Letters, **3**, 200 (2009).
DOI: 10.3144/expresspolymlett.2009.25

[9] Shao C., Kim H-Y., Gong J., Ding B., Lee D-R., Park S-J.: Fiber mats of poly(vinyl alcohol)/silica composite via electrospinning. Materials Letters, **57**, 1579–1584 (2003).
DOI: 10.1016/S0167-577X(02)01036-4

[10] Heikkilä P., Harlin A.: Electrospinning of polyacrylonitrile (PAN) solution: Effect of conductive additive and filler on the process. Express Polymer Letters, **3**, 437–445 (2009).
DOI: 10.3144/expresspolymlett.2009.53

[11] Kostakova E., Mészáros L., Gregr J.: Composite nanofibers produced by modified needless electrospinning. Materials Letters, **63**, 2419–2422 (2009).
DOI: 10.1016/j.matlet.2009.08.014

[12] Desai K., Kit K., Li J., Davidson P. M., Zivanovic S., Meyer H.: Nanofibrous chitosan non-wovens for filtration applications. Polymer, **50**, 3661–3669 (2009).
DOI: 10.1016/j.polymer.2009.05.058

[13] Thakur R. A., Florek C. A., Kohn J., Michniak B. B.: Electrospun nanofibrous polymeric scaffold with targeted drug release profiles for potential application as wound dressing. International Journal of Pharmaceutics, **364**, 87–93 (2008).
DOI: 10.1016/j.ijpharm.2008.07.033

[14] Kneawy R., Layman J. M., Watkins J. R., Bowlin G. L., Matthews J. A., Simpson D. G., Wnek G. E.: Electrospinning of poly(ethylene-co-vinyl alcohol) fibers. Biomaterials, **24**, 907–913 (2003).
DOI: 10.1016/S0142-9612(02)00422-2

[15] Rho K. S., Jeong L., Lee G., Seo B-M., Park Y. J., Hong S-D., Roh S., Cho J. J., Park W. H., Min B-M.: Electrospinning of collagen nanofibers: Effects on the behavior of normal human keratinocytes and early-stage wound healing. Biomaterials, **27**, 1452–1461 (2006).
DOI: 10.1016/j.biomaterials.2005.08.004

[16] Kolácná L., Bakešová J., Varga F., Koštáková E., Plánka L., Necaš A., Lukáš D., Amler E., Pelouch V.: Biochemical and biophysical aspects of collagen nanostructure in the extracellular matrix. Physiological Research, **56**, S51–S60 (2007).

[17] Schnell E., Klinkhammer K., Balzer S., Brook G., Klee D., Dalton P., Mey J.: Guidance of glial cell migration and axonal growth on electrospun nanofibers of poly-ε-caprolactone and a collagen/poly-ε-caprolactone blend. Biomaterials, **28**, 3012–3025 (2007).
DOI: 10.1016/j.biomaterials.2007.03.009

[18] Yoshimoto H., Shin Y. M., Terai H., Vacanti J. P.: A biodegradable nanofiber scaffold by electrospinning and its potential for bone tissue engineering. Biomaterials, **24**, 2077–2082 (2003).
DOI: 10.1016/S0142-9612(02)00635-X

[19] Thomas V., Jose V. M., Chowdhury S., Sullivan J. F., Dean D. R., Vohra Y. K.: Mechano-morphological studies of aligned nanofibrous scaffolds of polycaprolactone fabricated by electrospinning. Journal of Biomaterials Science, Polymer Edition, **17**, 969–984 (2006).
DOI: 10.1163/156856206778366022

[20] Pinto N. J., González R., Johnson A. T., MacDiarmid A. G.: Electrospun hybrid organic/inorganic semiconductor Schottky nanodiode. Applied Physics Letters, **89**, 033505/1–033505/3 (2006).
DOI: 10.1063/1.2227758

[21] Sill T. J., Recum H. A.: Electrospinning: Applications in drug delivery and tissue engineering. Biomaterials, **29**, 1989–2006 (2008).
DOI: 10.1016/j.biomaterials.2008.01.011

[22] Verreck G., Chun I., Peeters J., Rosenblatt J., Brewster M. E.: Preparation and characterization of nanofibers containing amorphous drug dispersions generated by electrostatic spinning. Pharmaceutical Research, **20**, 810–817 (2003).
DOI: 10.1023/A:1023450006281

[23] Yu D-G., Zhang X-F., Shen X-X., Brandford-White C., Zhu L-M.: Ultrafine ibuprofen-loaded polyvinylpyrrolidone fiber mats using electrospinning. Polymer International **58**, 1010–1013 (2009).
DOI: 10.1002/pi.2629

[24] Yu D-G., Shen X-X., Brandford-White C., Zhu L-M.: Oral fast-dissolving drug delivery membranes prepared from electrospun polyvinylpyrrolidone ultrafine fibers. Nanotechnology, **20**, 055104 (2009).
DOI: 10.1088/0957-4484/20/5/055104

[25] Yu D-G., Brandford-White C., White K., Li X-L., Zhu L-M.: Dissolution improvement of electrospun nanofiber-based solid dispersions for acetaminophen. AAPS PharSciTech, **11**, 809–817 (2010).
DOI: 10.1208/s12249-010-9438-4

[26] Sastry S. V., Nysadham J. R., Fix J. A.: Recent technological advances in oral drug delivery – A review. Pharmaceutical Science and Technology Today, **3**, 138–145 (2000).
DOI: 10.1016/S1461-5347(00)00247-9

[27] Biradar S. S., Bhagavati S. T., Kuppasad I. J.: Fast dissolving drug delivery systems: A brief overview. The Internet Journal of Pharmacology, **4**, (2006).

[28] Gupta A., Mishra A. K., Gupta V., Bansal P., Singh R., Singh A. K.: Recent trends of fast dissolving tablet – An overview of formulation technology. International Journal of Pharmaceutical and Biological Archives, **1**, 1–10 (2010).

[29] Tao J., Shivkumar S.: Molecular weight dependent structural regimes during the electrospinning of PVA. Materials Letters, **61**, 2325–2328 (2007).
DOI: 10.1016/j.matlet.2006.09.004

[30] Baumgarten P. K.: Electrostatic spinning of acrylic microfibers. Journal of Colloid Interface Science, **36**, 71–79 (1971).
DOI: 10.1016/0021-9797(71)90241-4

[31] Kenawy E. R., Abdel-Hay F. I., El-Newehy M. H., Wnek G. E.: Controlled release of ketoprofen from electrospun poly(vinyl alcohol) nanofibers. Materials Science and Engineering A, **459**, 390–396 (2007).
DOI: 10.1016/j.msea.2007.01.039

[32] Noyes A., Whitney W. R.: The rate of solution of solid substances in their own solutions. Journal of the American Chemical Society, **19**, 930–934 (1897).
DOI: 10.1021/ja02086a003

[33] Marosi Gy.: Electrospinning a feasible nanotechnology. Express Polymer Letters, **4**, 263 (2010).
DOI: 10.3144/expresspolymlett.2010.33

*eXPRESS Polymer Letters Vol.4, No.12 (2010) 773–780*
*Available online at www.expresspolymlett.com*
*DOI: 10.3144/expresspolymlett.2010.93*

# Drug release behavior of a pH/temperature sensitive calcium alginate/poly(*N*-acryloylglycine) bead with core-shelled structure

*K. L. Deng*[*], *H. B. Zhong, T. Tian, Y. B. Gou, Q. Li, L. R. Dong*

College of Chemistry & Environmental Science, Hebei University, Baoding 071002, China

*Received 3 June 2010; accepted in revised form 24 August 2010*

**Abstract.** In this study, a novel pH/temperature sensitive hydrogel bead with core-shelled structure, composed of calcium alginate (Ca-alginate) and poly(*N*-acryloylglycine) (PAG), was prepared using as a drug delivery system. The equilibrium swelling has indicated the distinct sensitivities of the beads to pH value and temperature. In pH = 7.4 phosphate buffer solution (PBS), the cumulative release amount of indomethacin loaded in the core of the beads was about 83.5% within 650 min, whereas this value only reached 16.6% in pH = 2.1 PBS. In addition, the release rate of indomethacin was much faster at 37°C than that at 24°C. The experimental results have showed that the Ca-alginate/PAG beads have a potential application for the pH/temperature-controlled drug release carrier in the biomedical field.

***Keywords:*** *smart polymers, drug release, core-shelled bead, pH/temperature sensitive*

## 1. Introduction

A smart hydrogel is a three-dimensional polymeric network containing a large number of hydrophilic groups, which is capable of absorbing large quantities of water, but does not dissolve [1]. These hydrogels show the ability of abrupt change including the physical or chemical properties in response to the external stimuli such as pH [2–5], temperature [4–6], electrical field [7, 8], magnetic field [9], ion exchange [10]. The unique properties of a smart hydrogel imply that it can be used as a promising material in the biomedical and industrial applications. Some significant applications of hydrogels have been widely investigated including dialysis membranes [11], enzyme immobilization [12], tissue engineering [13], and drug controlled release systems [14–17] and so on. Among the smart materials, pH- and temperature-sensitive hydrogels have been paid more attentions because the two physiological factors are very important for the human body [18–21].

To prepare a stimulus-sensitive polymeric hydrogel with biocompatiblity and biodegradation, many efforts have been made to combine the thermo-sensitive polymers with some biopolymers such as $\beta$-cyclodextrin, starch, alginate and chitosan [22–24]. Alginate is a kind of water-soluble linear polysaccharide separated from brown sea weed and is composed of alternating blocks of 1–4 linked $\alpha$-*L*-guluronic and $\beta$-*D*-mannuronic acid residues. Alginate can be cross-linked by the chelating effect of divalent cations such as calcium ion in the aqueous solution, leading to a facile preparation of hydrogel beads. As a pH-sensitive natural material, alginate is relatively low cost [25]. As a result, alginate is often selected as a matrix for the entrapment and

---

[*] Corresponding author, e-mail: dkl369@hbu.edu.cn

delivery of proteins, drugs, and cells because of its biocompatiblity and biodegradability under the normal physiological conditions [26–28].

Recently, it was reported that many amino acid moieties have been attractive candidates for synthesizing hydrogel materials to improve their biodegradability and biocompatibility [29–31]. For instance, a new enzymatically degradable temperature-sensitive biomaterial, poly (ethylene glycol)-*b*-poly (alanine-co-phenyl alanine) was synthesized by introducing amino-acid moiety as the main component [30]. Based on glycine, El-Sherbiny *et al.* [31] prepared a novel biodegradable pH/thermo-responsive poly(*N*-acryloylglycine-chitosan) hydrogel, for using as a controlled drug delivery carrier. In addition, our recent experiments have shown the injectable behaviors of glycine-based PAG with the temperature changing. PAG aqueous solution is in fluid state at higher temperature, while PAG solution reversibly turns into solid hydrogel at lower temperature. The H-bonding network among carboxyl (–COOH), amide (–CONH) groups in PAG chains and water molecules plays a crucial role in the transition of sol to gel.

In this investigation, we described the fabrication of a novel pH/temperature sensitive bead with core-shelled structure for the drug release carrier. The pH/temperature sensitive hydrogel beads were composed of Ca-alginate and PAG. The sensitive, core-shelled beads were prepared by three steps: the core formation, the swelling in sodium alginate solution and the cross-linking of shell. The pH-sensitivity of the beads originates from the shell composed of alginate and its temperature-sensitivity is mainly attributed to the core of PAG hydrogel. Theoretically, the combination of alginate and PAG could provide a new and efficient smart drug delivery system with a dual pH-temperature sensitivity. The release behavior of indomethacin from the bead with core-shelled structure was studied as function of the PAG concentration, temperature and pH in phosphate buffer solutions simulated to gastric (pH = 2.1) and intestinal fluids (pH = 7.4).

## 2. Experimental part

### 2.1. Materials

Sodium alginate (viscosity of 2% solution at 25°C = 250 cps, Wuhan Sigma Chem. Co., Ltd., China) and indomethacin (Fluka Chem. Co., Ltd.) were used as received. Acryloyl chloride was supplied by Merck (Schuchardt OHG, Hohenbrunn, Germany). Glycine was purchased from Dongfang Health Materials Factory (Tianjin, China). All other chemicals were analytical grade and used without any further purification.

### 2.2. Measurements

$^1$H NMR spectrum of PAG was measured using a Bruker Avance400 (400 MHz) (Bruker, Switzerland) with tetramethylsilane (TMS) as internal reference. Fourier-transform infrared (FTIR) spectra were recorded on a Vector22 FTIR spectrophotometer (Bruker, Switzerland) in KBr pellet. Elemental analysis results were taken using a Elemental Analyzer CE-440 (Exeter Analytical, Inc., USA).

### 2.3. Preparation of the core-shelled beads

The composition of prepared beads was described in Table 1. Firstly, poly(*N*-acryloylglycine) (PAG) prepared from glycine and acryloyl chloride according to the described procedure [31] and sodium alginate were dissolved in deionized water, respectively. The sodium alginate concentrations were controlled at 1.5% (w/w) for all the samples in this study. Drug model, indomethacin was added into PAG solution at the ratio of 20% (w/w) (relative to the total weights of PAG). Secondly, using a syringe, the hot PAG-indomethacin solutions were extruded in the form of droplets into the cold acetate ethyl/chloroform under stirring at the rate of 60 rmp. The core of the titled bead was formed because of injectablity of PAG. The indomethacin loaded beads (with the average diameter 3 mm) were transferred to sodium alginate solution at

**Table 1.** Composition and drug content of the core-shelled beads

| Sample | Alginate concentration [% (w/w)] | PAG concentration [% (w/w)] | Drug feed to PAG [%] | Loading efficiency [%] | Drug content [%] |
|---|---|---|---|---|---|
| A | 1.5 | 10.0 | 20.0 | 75.2 | 0.31 |
| B | 1.5 | 15.0 | 20.0 | 76.8 | 0.46 |
| C | 1.5 | 20.0 | 20.0 | 78.9 | 0.61 |

room temperature. After 1 hour, the bead swelled to some extent so as to get the shell structure of the bead. Lastly, the bead with core-shelled structure were immersed in the 1.5% $CaCl_2$ (w/v) solution for 30 minutes. The spherical, homogenous and core-shelled beads were obtained via the further crosslinking in the shell. After crosslinking, the beads were washed with deionized water repeatedly to remove the un-crosslinked sodium alginate.

## 2.4. Swelling investigation

In this study, the swelling behavior of the beads was studied in different pH PBS and temperature. The pH values were simulated to gastric pH = 2.1 and intestinal fluids pH = 7.4 in human body, respectively. The beads were immersed in the required medium. After reaching the swelling equilibrium, the beads were taken out and wiped with soft paper tissue to remove the water on the bead surface, and then weighted. The swelling ratio (*SR*) for each sample was calculated by using Equation (1):

$$SR\,[\%] = \frac{W_s - W_d}{W_d}\cdot 100 \qquad (1)$$

where $W_s$ and $W_d$ represent the weights of hydrogels after and before swelling, respectively.

## 2.5. Loading content

The beads (about 25 mg) were crushed with a glass rod in a beaker and charged with 20 ml of PBS (pH = 7.4, containing 5% (v/v) ethanol) under stirring for 12 h. The clear supernatant was collected in another flask. Again, another 20 ml of PBS was added into the beaker for the further dissolving drug. The experimental process was repeated until no indomethacin was determined in the new clear supernatant by UV measurement. The amount of indomethacin loaded in the beads was determined by UV spectrophotometry at 329 nm using a calibration curve constructed from a series of standard indomethacin solutions. The loading content [%] is the weight percentage of drug indomethacin relative to the beads in this study.

## 2.6. *In vitro* indomethacin release

The drug release experiments were carried out by immersing the beads (about 0.040 g) in the desired 40 ml medium in a separate 100 ml flask. The flask was controlled at a required temperature and equipped with a magnetic stirrer. At the predetermined time interval, 4 ml release medium was taken out and the fresh medium with same volume was added to the flask to maintain the unchanged volume. The amount of indomethacin released from the beads was determined at 329 nm with a UV spectrometer. In addition, the data used in this paper were obtained from the average value of three determined value.

## 3. Results and discussion

### 3.1. Preparation of the bead with core-shelled structure

The fabrication strategy for the bead with core-shelled structure is illustrated in Figure 1. First of all, it is necessary to state that our recent experiment has indicated the obvious injectability of PAG selected in this work. PAG in water is in the form of solution at higher temperature, while PAG solution reversibly turns into hydrogel state at lower temperature. This transition of sol to gel is ascribed to the H-bonding interaction constructed by carboxyl (–COOH), amide (–CONH) groups in PAG chains and water molecules. It is also accepted that the density of crosslinking of PAG gel was increased with enhancing the PAG concentration, decreasing the temperature and pH value in the medium. The detailed study results about PAG are to be published in the other journal.

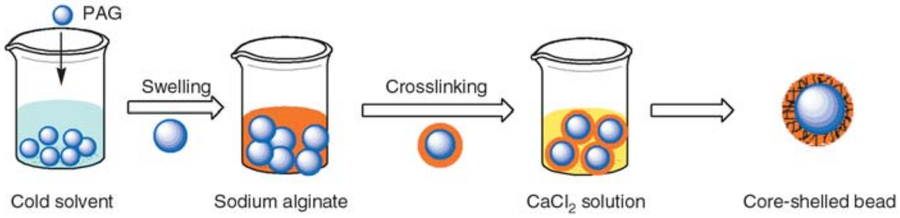

**Figure 1.** Schematic overview of synthesis of sensitive beads with core-shelled structure

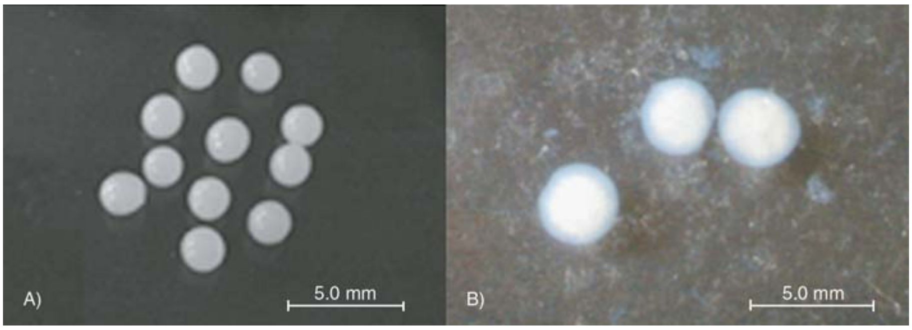

**Figure 2.** Photographs of the beads with the core-shelled structure (A: the core of PAG, B: the core-shelled bead)

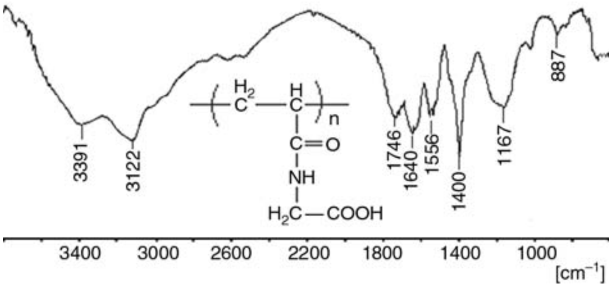

**Figure 3.** FTIR spectrum of PAG

In the process of preparing the PAG core, PAG solution was first heated up to 45°C, and then the hot PAG solution was extruded out by a syringe into a cold acetate ethyl/chloroform. To get the homogeneous spheres, some measures must be adopted in this study. The density of organic mixed solvent was controlled at about 1.0 with acetate ethyl and chloroform, avoiding the fast falling of PAG drops in the solution. In addition, the temperature of organic mixed solvent was regulated as low as possible. The PAG core hydrogel can swell to some extent in the sodium alginate solution, leading to the preliminary form of the shell layer. Obviously, the time interval of swelling for PAG core plays a key role in controlling the thickness of the shell. In the $CaCl_2$ solution, the cross-linked shell was formed by the chelating of $Ca^{2+}$ with sodium alginate. Theoretically speaking, the beads contained a partial interpenetrating network layer composed of a little PAG chain and calcium alginate. Because of the unavoidable loss of indomethacin in the preparation, the loading efficiency was round 75–80% for all the samples (Table 1). To clearly illustrate the structure of the bead, we have obtained two photographs by a digital camera. The diameter of the prepared beads in this study was about 3 mm. Seen from Figure 2, the core-shelled structure of the beads can be observed distinctly (B). The core PAG is also homogeneous and glabrous spheres.

## 3.2. Characterization of PAG

The structure of PAG was confirmed by $^1$H NMR and IR measurements. As shown in Figure 3, the absorption peak at 3000–3600 cm$^{-1}$ was assigned to N–H stretching vibration of amide groups and O–H stretching vibration of carboxyl. The stretching vibrations of carbonyl (C=O) from carboxyl and amide groups were found at 1746 and 1640 cm$^{-1}$, respectively. Additionally, the characteristic peaks of ester (C–O–C) were also observed at 1167 cm$^{-1}$. In the $^1$H NMR spectrum of PAG (Figure 4), the peaks at 3.6–4.2 ppm were ascribed to methylene group in [–NHC$\underline{H}_2$COOH] repeating unit. The chemical shift of methylene and methine groups in [–C$\underline{H}_2$–C$\underline{H}$–] repeating unit was observed at 1.3–1.9 ppm and 2.0–2.5 ppm, respectively. Herein, the peak at 8.1–8.3 ppm indicated the existence of hydrogen atom in amide group of [–N$\underline{H}$CH$_2$COOH] moiety. The absorption peaks ascribed to carboxyl (–COO$\underline{H}$) was not found because of the complete deuteration of COOH with $D_2O$. Also, the ratio among hydrogen atoms except for amide and carboxyl was in good accordance with the molecular structure of PAG. In addition, the elemental analysis for PAG $(C_5H_7N_1O_3)_n$ is listed as follow: Calcd: C 46.51, H 5.43, N 10.85; Found: C 46.39, H 5.52, N 10.67. Based on the above-mentioned data, it can

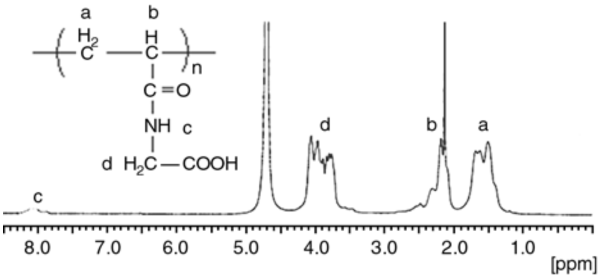

**Figure 4.** $^1$H NMR spectrum of PAG (in $D_2O$)

be concluded that we have synthesized the titled polymer PAG.

### 3.3. Swelling study

In this study, the swelling ratio was obtained from the Equation (1). Table 2 has shown the dependence of swelling behavior of the beads on the different pH values and temperatures. A remarkably lower swelling ratio was found in the lower pH PBS. Because $pK_a$ of alginate and PAG is about 3.2, most of carboxyl groups in the alginate and PAG exist in the form of COOH in the low pH medium (pH = 2.1). In the shell, the H-bonding constructed by –COOH of alginate led to the stronger interactions between polymer chains. Also, the H-bonding interactions among –COOH from PAG chains in the core predominated over the polymer-water interactions. Accordingly, the swelling ratio of the core-shelled beads in pH = 2.1 PBS is relatively low. In the higher pH PBS, the carboxylic acid groups were ionized and became $–COO^-$ form. Thus, the weakened H-bonding interaction between polymer chains and electrostatic repulsion from $–COO^-$ groups resulted in the higher swelling ratio [16].

Additionally, no significant difference of the swelling ratios was observed among all the samples in pH = 7.4 PBS at 25°C. However, the swelling ratio increases significantly with increasing the temperature. For instance, the swelling ratios were 21.9 and 38.1% when the temperature was fixed at 25 and 37°C in pH = 2.1 PBS for the sample B. This observation is ascribed to the weakened H-bonding of polymer chains at higher temperature. As a result, the effective outspread of PAG and alginate chains at 37°C led to an increase of the swelling ratio.

**Table 2.** Dependence of swelling ratio of the beads on pH and temperature

| Sample | pH = 2.1 25°C [%] | pH =2.1 37°C [%] | pH =7.4 25°C [%] | pH = 7.4 37°C [%] |
|---|---|---|---|---|
| A | 21.5 | 39.8 | 87.1 | 108.0 |
| B | 21.9 | 38.1 | 86.4 | 103.2 |
| C | 23.1 | 35.6 | 83.2 | 98.9 |

### 3.4. Drug release study

As shown in Figure 5, the release behaviors of indomethacin from the beads have reflected a remarkable dependence on pH value at 37.0°C. In pH = 2.1 PBS, the amount of indomethacin released is described as an initial burst (about 10%), thereafter, almost no further indomethacin diffused out from the bead. The initial burst release behavior can be explained as the fast diffusion of indomethacin molecules in the surface layer of the beads. The low cumulative release of indomethacin is ascribed to the low swelling ratio of the beads in acidic conditions as shown in Table 2. The smaller channels for drug diffusion in the bead caused by lower swelling ratio hold back the effective drug release. In addition, the core PAG maintains a hydrogel state with higher density of crosslinking in the acidic medium. Thus, compared with the solution state of PAG, the core PAG with hydrogel state consequentially block the release of indomethacin to the outside. As an organic acid, indomethacin ($pK_a$ = 4.5) also exists in the form of –COOH in pH = 2.1 PBS, The intermolecular H-bonding between indomethacin and PAG chains obviously block the drug release from the bead.

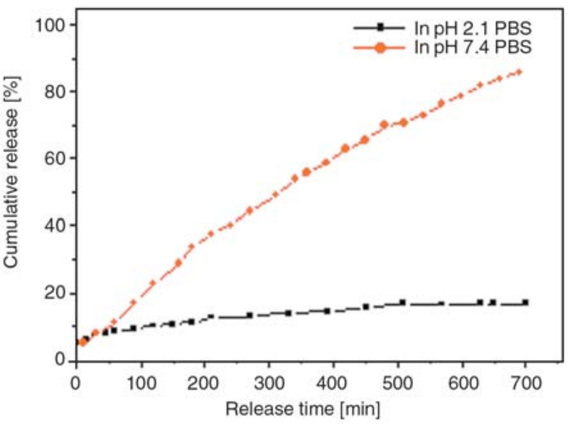

**Figure 5.** The effect of pH value on drug release behavior of the bead (B)

The cumulative amount of released indomethacin in pH = 7.4 PBS reached to as high as 83.5% within 650 min. This higher release rate may be related to the higher swelling ratio of the beads and the weak H-bonding interaction between drug and polymer network in the neutral PBS. A similar release behavior has also been reported in an inorganic-organic hybrid alginate bead and *N*-succinyl chitosan/alginate hydrogel systems [23, 24]. From the more practical point of view, the bead can overpass the acidity medium of gastric fluid without releasing substantial amounts of drug molecules, but release a mass of drug in the small intestine.

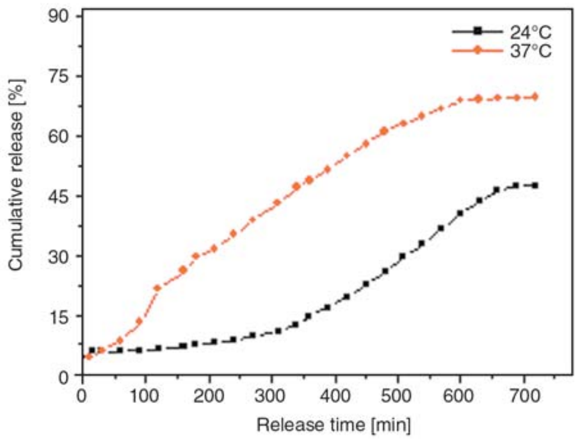

**Figure 6.** The effect of temperature on drug release behavior of the bead (B)

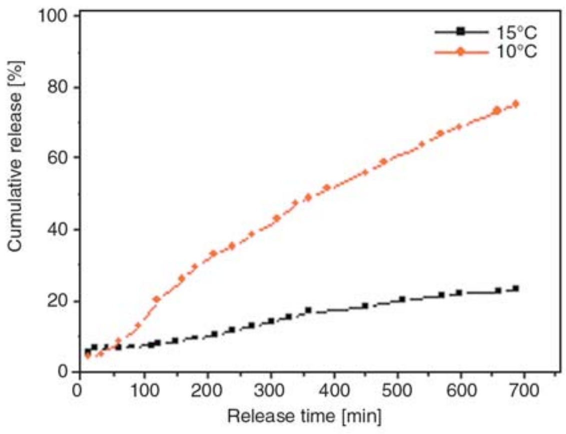

**Figure 7.** The effect of PAG concentration on drug release behavior of the bead (A and B)

The temperature-controlled release of indomethacin in pH = 7.4 PBS has been presented in Figure 6. The higher release rate was observed at 37°C while the release rate of indomethacin at 24°C was found to be much lower. For example, the amount of indomethacin released from the bead reached 46.4 and 12.1% within 330 minutes when the temperature was fixed at 37 and 24°C, respectively. For the core-shelled bead, the effective crosslinking density of PAG in the core constructed via H-bonding was decreased by increasing the temperature, which accelerated the drug release [13]. Accordingly, the transition of sol to gel of PAG or the cross-linking density formed by H-bonding in the core plays a key role in regulating the release of the entrapped drug molecules from the beads.

As for the shell composed of calcium-alginate, the disruption of the calcium-alginate in the bead is inclined to occur in PBS above pH = 5.5, via the chelating function of the phosphate ions from PBS [32]. The affinity of calcium to phosphate is higher than that to alginate in the neutral or alkaline PBS, and the solubility of calcium-phosphate complex increases at the higher temperature. Compared with 24°C, the stronger affinity of phosphate to calcium at 37°C accelerated the disruption of the shell. As a result, the faster drug release rate was observed from the beads with core-shell structure at higher temperature.

It is necessary to mention that the release rate of indomethacin in this work is lower than that reported by Park *et al.* [13] and Choi *et al.* [16] at 25°C. In the investigation of Park and Choi, drug was loaded into the beads by the sorption method, and most of the drug existed in the surface layer of the beads. In our study, the same drug was directly incorporated into the core of the beads during the preparation of bead. The release rate of drug loaded in the core was lower than that in the surface layer of the bead. Therefore, the different drug-loading methods may be responsible for the different release behaviors.

Figure 7 has indicated the effect of PAG concentration in the core on indomethacin release at 37°C and in pH = 7.4 PBS. It was found that the release of indomethacin was increased with a decreasing the PAG concentration in the core. For example, when the PAG concentration was fixed at 10 and 15%, the cumulative releases of drug were 69.4 and 21.8% within 600 minutes, respectively. It is necessary to state that the more the PAG concentration is, the higher density of crosslinking of PAG hydrogel in the core is. That is, the higher PAG concentration in the core leads to the stronger physically crosslinking constructed by H-bonding among amides and carboxyl groups, preventing the effective diffusion of drug molecule to the outside. Clearly, the PAG concentration in the core can be used as a measure to regulate the release rate of drug.

## 4. Conclusions

In this paper, a novel pH/temperature-sensitive hydrogel bead with core-shelled structure, composed of Ca-alginate and PAG, was prepared using as drug delivery carrier. The equilibrium swelling behaviors of the beads clearly indicated the remarkable sensitivity to the external pH and temperature. The drug release behavior of indomethacin from the beads was characterized as a function of pH, temperature and the PAG concentration. 83.5% indomethacin in the bead was released within 650 min in pH = 7.4 PBS, while this value was only 16.6% in pH = 2.1 PBS. Additionally, indomethacin release rate was much faster at 37°C than that at 24°C because of the injectability of PAG in the core of the bead. It seems to expect that the Ca-alginate/PAG beads possess a potential application in the drug delivery systems controlled by pH or temperature.

## Acknowledgements

The authors are grateful for the financial support from the Hebei Natural Science Foundation of China (B2008000573).

## References

[1] Wang B. B., Zhu W., Zhang Y., Yang Z. G., Ding J. D.: Synthesis of a chemically-crosslinked thermo-sensitive hydrogel film and in situ encapsulation of model protein drugs. Reactive and Functional Polymers, **66**, 509–518 (2006).
DOI: 10.1016/j.reactfunctpolym.2005.10.003

[2] Zhou Y., Yang D., Ma G., Tan H., Jin Y., Nie J.: A pH-sensitive water-soluble N-carboxyethyl chitosan/poly(hydroxyethyl methacrylate) hydrogel as a potential drug sustained release matrix prepared by photopolymerization technique. Polymers for Advanced Technologies, **19**, 1133–1141 (2008).
DOI: 10.1002/pat.1097

[3] Wu J., Su Z-G., Ma G-H.: A thermo- and pH-sensitive hydrogel composed of quaternized chitosan/glycerophosphate. International Journal of Pharmaceutics, **315**, 1–11 (2006).
DOI: 10.1016/j.ijpharm.2006.01.045

[4] Zhao Y., Su H., Fang L., Tan T.: Superabsorbent hydrogels from poly(aspartic acid) with salt- temperature- and pH-responsiveness properties. Polymer, **46**, 5368–5376 (2005).
DOI: 10.1016/j.polymer.2005.04.015

[5] Atta A. M., Arndt K-F.: Temperature and pH sensitive ionic hydrogels based on new crosslinkers. Polymers for Advanced Technologies, **16**, 442–450 (2005).
DOI: 10.1002/pat.606

[6] El-Naggar A. W. M., Alla S. G. A., Said H. M.: Temperature and pH responsive behaviours of CMC/AAc hydrogels prepared by electron beam irradiation. Materials Chemistry and Physics, **95**, 158–163 (2006).
DOI: 10.1016/j.matchemphys.2005.05.037

[7] Kim S. J., Lee C. K., Lee Y. M., Kim I. Y., Kim S. I.: Electrical/pH-sensitive swelling behavior of polyelectrolyte hydrogels prepared with hyaluronic acid-poly(vinyl alcohol) interpenetrating polymer networks. Reactive and Functional Polymers, **55**, 291–298 (2003).
DOI: 10.1016/S1381-5148(03)00019-1

[8] Gerlach G., Guenther M., Sorber J., Suchaneck G., Arndt K-F., Richter A.: Chemical and pH sensors based on the swelling behavior of hydrogels. Sensors and Actuators B: Chemical, **111**, 555–561 (2005).
DOI: 10.1016/j.snb.2005.03.040

[9] Nishio Y., Yamada A., Ezaki K., Miyashita Y., Furukawa H., Horie K.: Preparation and magnetometric characterization of iron oxide-containing alginate/poly(vinyl alcohol) networks. Polymer, **45**, 7129–7136 (2004).
DOI: 10.1016/j.polymer.2004.08.047

[10] Rhim J-W., Park H. B., Lee C-S., Jun J-H., Kim D. S., Lee Y. M.: Crosslinked poly(vinyl alcohol) membranes containing sulfonic acid group: Proton and methanol transport through membranes. Journal of Membrane Science, **238**, 143–151 (2004).
DOI: 10.1016/j.memsci.2004.03.030

[11] Lin W-C., Liu T-Y., Yang M-C.: Hemocompatibility of polyacrylonitrile dialysis membrane immobilized with chitosan and heparin conjugate. Biomaterials, **25**, 1947–1957 (2004).
DOI: 10.1016/j.biomaterials.2003.08.027

[12] Lee Y., Kim D. N., Choi D., Lee W., Park J., Koh W-G.: Preparation of interpenetrating polymer network composed of poly(ethylene glycol) and poly(acrylamide) hydrogels as a support of enzyme immobilization. Polymers for Advanced Technologies, **19**, 852–858 (2008).
DOI: 10.1002/pat.1047

[13] Park H., Kang S-W., Kim B-S., Mooney D. J., Lee K. Y.: Shear-reversibly crosslinked alginate hydrogels for tissue engineering. Macromolecular Bioscience, **9**, 895–901 (2009).
DOI: 10.1002/mabi.200800376

[14] Zhang X-Z., Zhuo R-X., Cui J-Z., Zhang J-T.: A novel thermo-responsive drug delivery system with positive controlled release. International Journal of Pharmaceutics, **235**, 43–50 (2002).
DOI: 10.1016/S0378-5173(01)00976-0

[15] Shin H. S., Kim S. Y., Lee Y. M.: Indomethacin release behaviors from pH and thermoresponsive poly(vinyl alcohol) and poly(acrylic acid) IPN hydrogels for site-specific drug delivery. Journal of Applied Polymer Science, **65**, 685–693 (1997).
DOI: 10.1002/(SICI)1097-4628(19970725)65:4<685::AID-APP7>3.0.CO;2-G

[16] Choi C. Y., Chae S. Y., Nah J-W.: Thermosensitive poly(*N*-isopropylacrylamide)-*b*-poly(ε-caprolactone) nanoparticles for efficient drug delivery system. Polymer, **47**, 4571–4580 (2006).
DOI: 10.1016/j.polymer.2006.05.011

[17] Salehi R., Arsalani N., Davaran S., Entezami A. A.: Synthesis and characterization of thermosensitive and pH-sensitive poly (*N*-isopropylacrylamide-acrylamide-vinylpyrrolidone) for use in controlled release of naltrexone. Journal of Biomedical Materials Research Part A, **89**, 919–928 (2009).
DOI: 10.1002/jbm.a.32047

[18] Ma L., Liu M., Liu H., Chen J., Gao C., Cui D.: Dual crosslinked pH- and temperature-sensitive hydrogel beads for intestine-targeted controlled release. Polymers for Advanced Technologies, **21**, 348–355 (2010).
DOI: 10.1002/pat.1434

[19] El-Sherbiny I. M., Abdel-Bary E. M., Harding D. R. K.: Preparation and *in vitro* evaluation of new pH-sensitive hydrogel beads for oral delivery of protein drugs. Journal of Applied Polymer Science, **115**, 2828–2837 (2010).
DOI: 10.1002/app.30881

[20] Mano J. F.: Stimuli-responsive polymeric systems for biomedical applications. Advanced Engineering Materials, **10**, 515–527 (2008).
DOI: 10.1002/adem.200700355

[21] Asman G., Şanl O., Tuncel D.: pH- and temperature-sensitive *in vitro* release of salicylic acid through poly(vinyl alcohol-g-acrylamide) membranes. Journal of Applied Polymer Science, **107**, 3005–3012 (2008).
DOI: 10.1002/app.27491

[22] Yang X., Kim J-C.: β-Cyclodextrin hydrogels containing naphthaleneacetic acid for pH-sensitive release. Biotechnology and Bioengineering, **106**, 295–302 (2010).
DOI: 10.1002/bit.22696

[23] Shi J., Liu L. H., Liu X. P., Sun X. M., Cao S. K.: Inorganic-organic hybrid alginate beads with LCST near human body temperature for sustained dual-sensitive drug delivery. Polymers for Advanced Technologies, **19**, 1467–1473 (2008).
DOI: 10.1002/pat.1149

[24] Dai Y-N., Li P., Zhang J-P., Wang A-Q., Wei Q.: A novel pH sensitive *N*-succinyl chitosan/alginate hydrogel bead for nifedipine delivery. Biopharmaceutics and Drug Disposition, **29**, 173–184 (2008).
DOI: 10.1002/bdd.590

[25] Matsusaki M., Akashi M.: Novel functional biodegradable polymer IV: pH-sensitive controlled release of fibroblast growth factor-2 from a poly(γ-glutamic acid)-sulfonate matrix for tissue engineering. Biomacromolecules, **6**, 3351–3356 (2005).
DOI: 10.1021/bm050369m

[26] Ju H. K., Kim S. Y., Lee Y. M.: pH/temperature-responsive behaviors of semi-IPN and comb-type graft hydrogels composed of alginate and poly(*N*-isopropylacrylamide). Polymer, **42**, 6851–6857 (2001).
DOI: 10.1016/S0032-3861(01)00143-4

[27] George M., Abraham T. E.: Polyionic hydrocolloids for the intestinal delivery of protein drugs: Alginate and chitosan – A review. Journal of Controlled Release, **114**, 1–14 (2006).
DOI: 10.1016/j.jconrel.2006.04.017

[28] Han B. S., Shen B. Y., Wang Z. H., Shi M. M., Li H. W., Peng C. H., Zhao Q. H., Gao C. Y.: Layered microcapsules for daunorubicin loading and release as well as *in vitro* and *in vivo* studies. Polymers for Advanced Technologies, **19**, 36–46 (2008).
DOI: 10.1002/pat.966

[29] Kidchob T., Kimura S., Imanishi Y.: Degradation and release profile of microcapsules made of poly[L-lactic acid-*co*-L-lysine(Z)]. Journal of Controlled Release, **54**, 283–292 (1998).
DOI: 10.1016/S0168-3659(98)00012-1

[30] Jeong Y., Joo M. K., Bahk K. H., Choi Y. Y., Kim H-T., Kim W-K., Lee H. J., Sohn Y. S., Jeong B.: Enzymatically degradable temperature-sensitive polypeptide as a new in-situ gelling biomaterial. Journal of Controlled Release, **137**, 25–30 (2009).
DOI: 10.1016/j.jconrel.2009.03.008

[31] El-Sherbiny M. I., Lins R. J., Abdel-Bary E. M., Harding D. R. K.: Preparation, characterization, swelling and in vitro drug release behaviour of poly[*N*-acryloylglycine-chitosan] interpolymeric pH and thermally-responsive hydrogels. European Polymer Journal, **41**, 2584–2591 (2005).
DOI: 10.1016/j.eurpolymj.2005.05.035

[32] Anil K. A., Bhopatkar D., Tokura S., Tamura H., Stevens W. F.: Chitosan-alginate multilayer beads for gastric passage and controlled intestinal release of protein. Drug Development and Industrial Pharmacy, **29**, 713–724 (2003).
DOI: 10.1081/DDC-120021320

eXPRESS Polymer Letters Vol.4, No.12 (2010) 781–789
Available online at www.expresspolymlett.com
DOI: 10.3144/expresspolymlett.2010.94

# Morphology and thermal stability of silk fibroin/starch blended microparticles

Y. Baimark*, M. Srisa-ard, P. Srihanam

Department of Chemistry and Center of Excellence for Innovation in Chemistry, Faculty of Science, Mahasarakham University, Mahasarakham 44150, Thailand

Received 24 May 2010; accepted in revised form 25 August 2010

**Abstract.** In the present study biodegradable microparticles of silk fibroin (SF)/starch blends were prepared by a simple water-in-oil emulsion solvent diffusion technique. SF/starch blended solution and ethyl acetate were used as water and oil phases, respectively. The influence of SF/starch ratios on characteristics of the blended microparticles was investigated. The SF conformation of microparticle matrices from FTIR analysis was changed from random coil to β-sheet form by blending with starch. The blended microparticles had lower dissolution in water than those of SF and starch microparticles. The 1/3 (w/w) SF/starch blended microparticles exhibited the lowest dissolution. The SF and starch microparticles showed irregular and deflated shapes, respectively. The blended microparticles were nearly spherical in shapes and smaller sizes. Thermal stability of the blended microparticles slightly increased with the starch blended ratio. The results suggested that SF conformational transition, thermal stability, morphology and dissolution of the blended microparticles can be adjusted by varying the blended ratio.

***Keywords:*** *biopolymers, silk fibroin, starch, conformational transition, morphology*

## 1. Introduction

Silk fibroin (SF) is a biodegradable and biocompatible natural protein polymer created by the *Bombyx mori* silkworm [1, 2] and has recently been extensively investigated as a biomaterial suitable for uses such as a matrix for cell culture substrates [3] and drug delivery systems [4, 5]. The minimal inflammatory reactions *in vitro* and *in vivo* of SF have been reported [6]. The SF has been processed into fibers, films and particles. Most research work has been focused on the widely studied SF films. However, the applications of SF films are limited due to their being very brittle in the dry state. The poor mechanical properties of the SF film could be improved by blending it with other polymers [7, 8, 9]. Other properties, such as conformational transition and thermal properties are dependant on the blended ratios. Preparation of SF microparticles by various techniques has been reported for drug delivery applications [4, 5, 10–13]. The SF/chitosan blended microparticles have been prepared by the coacervation/cross-linking method [14]. Starch is a non-toxic, biodegradable, biocompatible, edible and relative inexpensive material that has been widely studied in the entrapment of food ingredients [15, 16] and drugs [17–19]. Almost all starch microparticles have been prepared by an emulsification-cross-linking reaction [17–20]. The preparation of alginate/starch blended microparticles has been reported by Roy *et al.* [21]. However, no information on SF/starch blended microparticles has been published.

In the present work, we report the conformational transition, morphology and thermal stability of

---

[*] Corresponding author, e-mail: yodthong.b@msu.ac.th

SF/starch blended microparticles as a function of blended ratios. The dissolution in water of SF/starch blended microparticles was also determined.

## 2. Materials and methods

### 2.1. Materials

Silk cocoons from *B. mori* were kindly supplied by the Silk Innovation Center, Mahasarakham University, Mahasarakham, Thailand. $Na_2CO_3$ (99.5%, Carlo Erba, code no. 479306, MI, USA), $CaCl_2$ (94%, Unilab, code no. 0701013, Auckland, New Zealand), ethanol (99.8%, Carlo Erba, code no. 414608, France) and ethyl acetate (99.8%, Lab Scan, code no. A3511, Ireland) were used without further purification. Cassava starch (food grade, 96% starch, amylase content 16.8%) was purchased from Bangkok Inter Food Co., Ltd. (Bangkok, Thailand) and used without pretreatment.

Aqueous silk fibroin (SF) solution was prepared as follows. Silk cocoons were de-gummed by boiling in 0.5% $Na_2CO_3$ solution at 95°C for 30 min to remove sericin and then rinsed with distilled water before drying at room temperature. De-gummed SF fibers were dissolved in the ternary solvent system, $CaCl_2$-ethanol-water (mole ratio = 1:2:8), by stirring at 90°C. The SF solution was then dialyzed in cellulose tubular membranes (molecular weight cut-off 7000 Da, Lot# KC132124, Thermo Scientific, IL, USA) against distilled water for 3 days. After filtration, the SF concentration was adjusted to 1% w/v with distilled water. The 1% w/v starch solution was prepared by dispersing starch in distilled water at 80°C and stirring until gelatinization.

### 2.2. Preparation of blended microparticles

SF/starch blended solutions were firstly prepared by mixing SF and starch solutions with a magnetic stirrer for 1 hr before microparticle formation. The blended microparticles were fabricated in a one-step process by the water-in-oil (W/O) emulsion solvent diffusion method. Briefly, about 1.0 ml of blended solution was slowly added drop-wise into 200 ml of ethyl acetate with magnetic stirring at 900 rpm for 1 hr. The beaker was closed with aluminum foil to prevent organic solvent evaporation during the emulsification-diffusion process. The blended microparticles were recovered by centrifugation before being dried in a vacuum oven at room temperature overnight to remove residue organic solvent. Microparticles with SF/starch blended ratios of 4/0, 3/1, 2/2, 1/3 and 0/4 (w/w) were prepared and investigated.

### 2.3. Characterization of blended microparticles

The chemical structures and conformational transition of the microparticles were measured with Fourier transform infrared (FTIR) spectroscopy using a Spectrum GX FTIR spectrophotometer (Perkin-Elmer Co. Ltd., Massachusetts, USA) with air as the reference. The resolution of 4 $cm^{-1}$ and 32 scans were used. FTIR spectra were obtained using a KBr disk method. Thermal stability of the microparticles was analyzed by thermogravimetry (TG) using a SDT Q600 thermogravimetric analyzer (TA-Instrument Co. Ltd., New Castle, DE, USA). For TG analysis, 5–10 mg sample was heated from 50 to 1000°C at a heating rate of 20°C/min under a nitrogen atmosphere. Morphologies of the microparticles were determined by scanning electron microscopy (SEM) using a JSM-6460LV SEM (JEOL, Tokyo, Japan). The microparticles were coated with gold to enhance the surface conductivity before scanning. Particle size distribution of the microparticles was measured by the sieving method. For this purpose, the microparticles were sieved into three particle size ranges of <80, 80–150 and >150 μm before weighing. A dissolution test of microparticles in distilled water was performed. For this test, the microparticles were incubated in 20 ml of distilled water at 30°C and shaken at 100 rpm. The incubation times of 3 and 6 hrs were used. At the appropriate time, residual microparticles were separated by centrifugation at 10 000 rpm for 20 min before drying at 50°C in a vacuum oven for 24 hrs. The remaining SF microspheres were weighted after being stored in a desiccator for 6 hrs. Percentage of dissolution was calculated from Equation (1). The mean % dissolution values are the average of three parallel measurements. The differences between data sets are expressed by analysis of variance (ANOVA) and multiple *t* tests. $\leq 0.05$ was considered the statistically significant.

$$\%\ \text{dissolution} = \frac{\text{initial microparticles [mg]} - \text{remaining microparticles [mg]}}{\text{initial microparticles [mg]}} \cdot 100 \qquad (1)$$

where initial and remaining microparticles are the weights of microparticles before and after dissolution tests, respectively.

## 3. Results and discussion

### 3.1. FT-IR analysis

The functional groups of SF and starch components, and SF conformational transition were determined from the FTIR spectra of pure and blended microparticles as shown in Figure 1. The positions of absorption bands, especially amide I, II and III bands indicate the conformational transition of SF. The FTIR spectrum of SF microparticles (Figure 1a) showed absorption bands at 1654 cm$^{-1}$ (amide I), 1545 cm$^{-1}$ (amide II) and 1240 cm$^{-1}$ (amide III), assigned to the random coil SF conformation. The FTIR results indicated that the SF microparticle matrices were predominantly in random coil form. Whereas FTIR spectrum of starch microparticles in Figure 1e showed broad absorption bands at 3385–3550 and 2929 cm$^{-1}$ due to O–H and C–H stretching. The band at 1415 cm$^{-1}$ is assigned to C–H bending vibration. While the absorption band at 1000–1155 cm$^{-1}$ can be attributed to the saccharide structure of starch [20, 21]. As would be expected, band characteristics of both SF and starch were detected in the FTIR spectra of the blended microparticles. Intensities of starch characteristic bands at 2929, 1415 and 1000–1155 cm$^{-1}$ increased with the starch blended ratio (Figures 1b–1d). It should be noted that the FTIR spectra of 2/2 and 1/3 SF/starch blended microparticles showed O–H stretching bands of starch in the range of 3385–3550 cm$^{-1}$. While the FTIR spectrum of 3/1 SF/starch blended microparticles exhibited N–H stretching bands of SF at 3400 cm$^{-1}$.

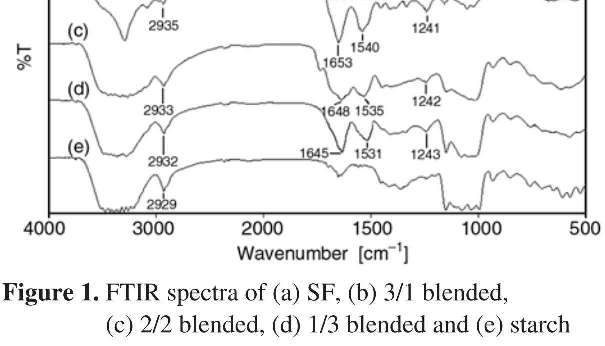

**Figure 1.** FTIR spectra of (a) SF, (b) 3/1 blended, (c) 2/2 blended, (d) 1/3 blended and (e) starch microparticles

It can be seen that the amide I and II bands of SF shifted slightly to a lower wave number after blending with starch. This shifting increased as the starch in the blended ratio increased. Whereas the amide III bands of SF shifted to a higher wave number after blending with starch. The results indicated that the SF microsphere matrices changed from random coil to β-sheet form. The fraction of β-sheet SF form of the blended microparticles increased as the starch blended ratio increased, suggesting interaction and miscibility between SF and starch. The shifting of SF amide bands in the FTIR spectra of its blends has been used to detect interactions and miscibility between SF and blended molecules [8, 22, 23]. For SF/hydroxyl propyl methyl cellulose (HPMC) blends, it has been proposed that the hydrogen bonding between NH in the amide groups of SF and OH of HPMC had occurred [22]. Therefore, the intermolecular bonds in the SF/starch blends in this work may be expected to be hydrogen bonding between NH in the amide groups of SF and OH of starch.

### 3.2. Morphology

The microparticles were formed and solidified after diffusion out of water from dispersed emulsion droplets to the continuous ethyl acetate phase. The microparticles suspended in ethyl acetate were obtained before being collecting by centrifugation. Morphology of the microparticles was characterized from the SEM images, as shown in Figure 2. It was found that the SF microparticles had an irregular-shape (Figure 2a). The microparticles of other proteins such as insulin have been prepared by the spray-drying method [24]. They were erythrocyte-like in shape. Solid shells formed because the drying started at the outside of the droplets. Almost all starch microparticles showed deflated-like shapes (Figure 2e). So, it was surprising that the blended microparticles were nearly spherical in shape and had a smooth surface (Figures 2b–2d). It should be

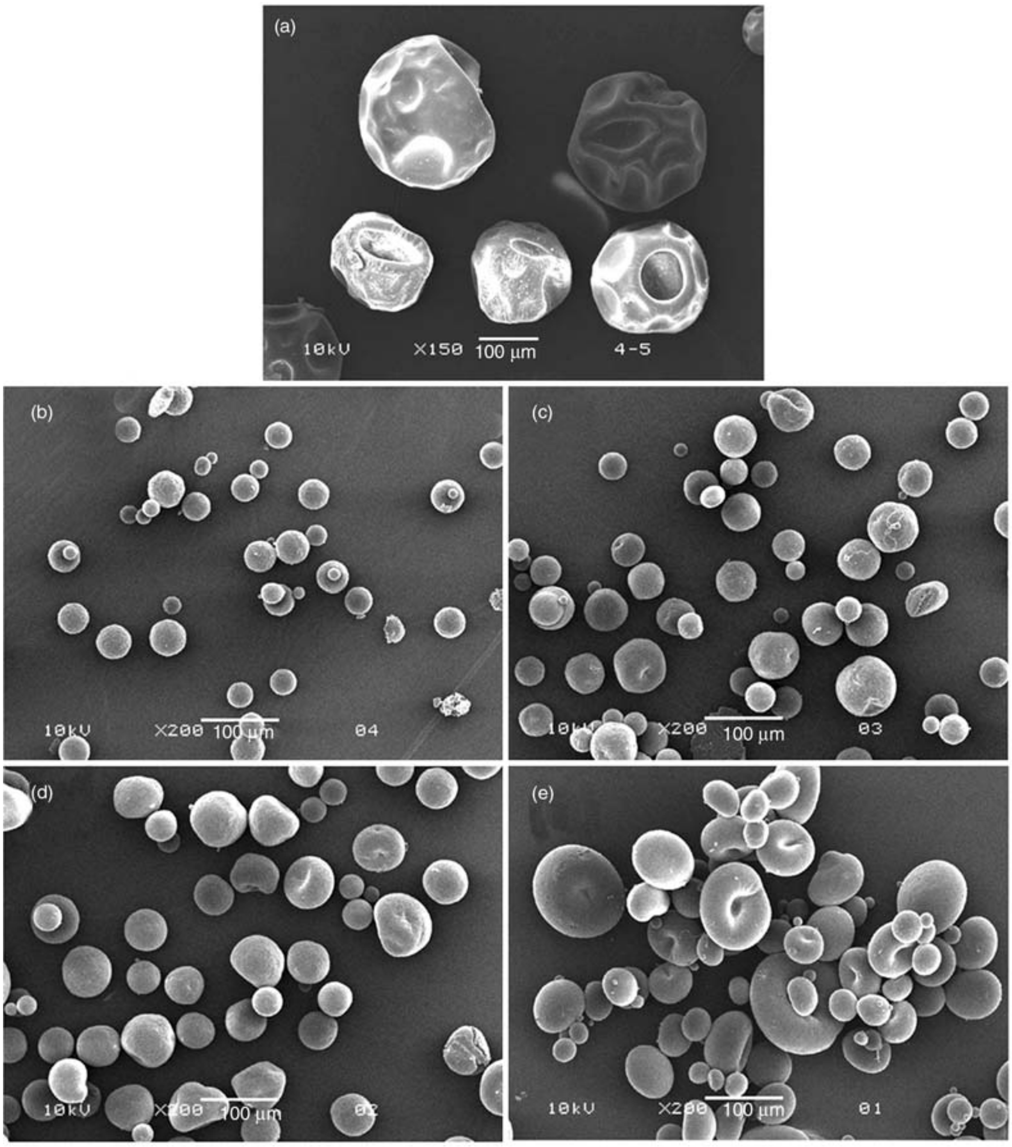

**Figure 2.** SEM micrographs of (a) SF, (b) 3/1 blended, (c) 2/2 blended, (d) 1/3 blended and (e) starch microparticles. All bars = 100 µm.

noted that the blended microparticles with SF/starch blended ratio of 3/1 (w/w) exhibited a uniform spherical shape compared to the other blended ratios. Some deflated microparticles can be found when the starch blended ratio was increased. This suggests that in the blending of SF with starch at appropriate ratios, uniformly spherical-shaped microparticles with smooth surfaces could be fabricated by the W/O emulsion solvent diffusion method.

The internal morphology of microparticles was determined from the SEM images of broken surfaces, as illustrated in Figure 3. This indicates that the microparticles contained voids or porous structures. The starch microparticle matrix was denser than that of the SF microparticle matrix. The numbers of voids decreased as the starch in the blended ratio increased. However, these porous forms were completely covered with a smooth surface for all blended ratios. Porous microparticles of a water-insoluble polymer have been prepared by the water$_1$-in-oil-in-water$_2$ ($W_1/O/W_2$) double emulsion method [25, 26]. The void structures were formed and solidified because of the diffusion out of $W_1$ to $W_2$ phase. It would be expected that the porous structures of SF, starch and their blended microparticles occurred due to diffusion out of water from emulsion droplets to the external ethyl acetate phase.

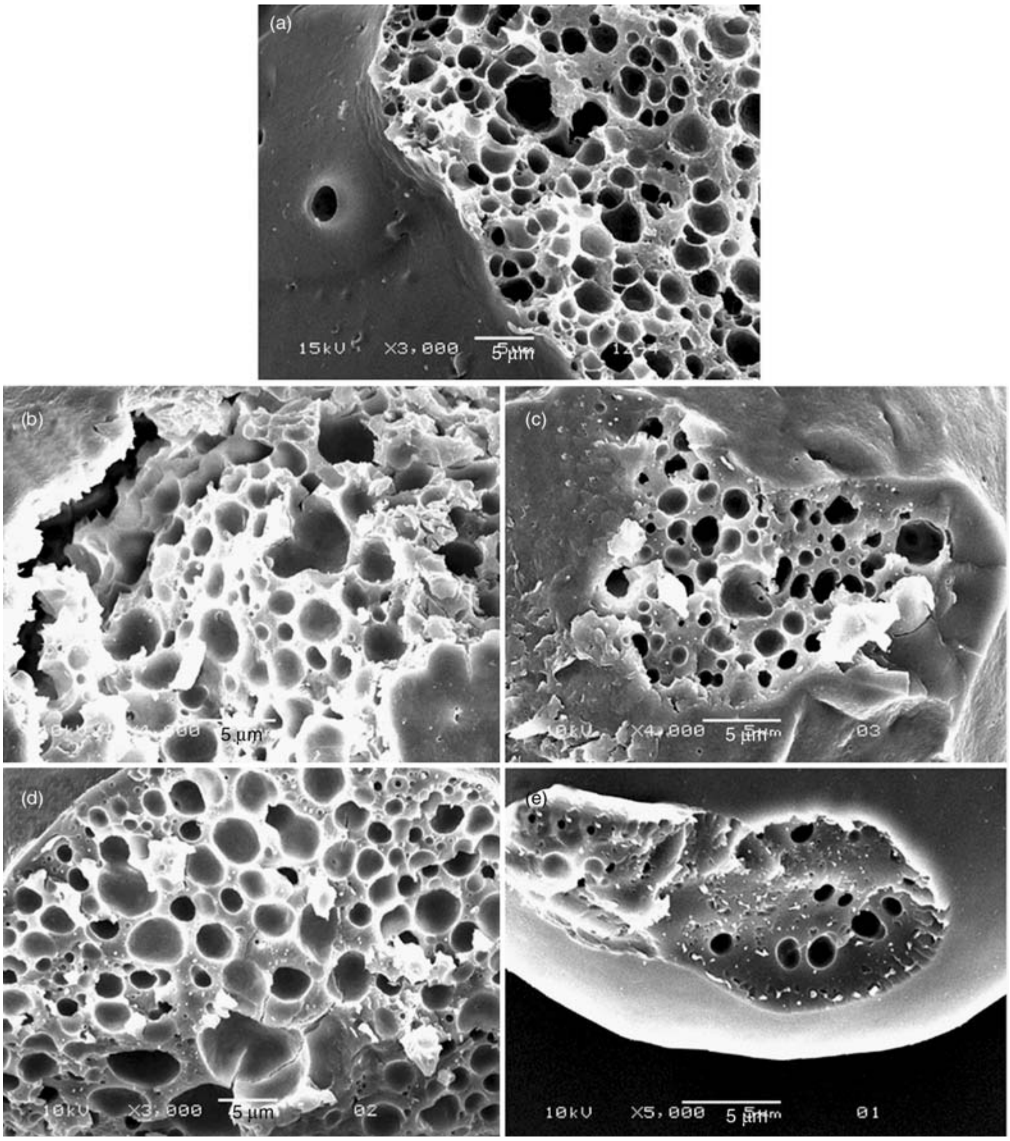

**Figure 3.** SEM micrographs of broken surfaces of (a) SF, (b) 3/1 blended, (c) 2/2 blended, (d) 1/3 blended and (e) starch microparticles. All bars = 5 µm.

## 3.3. Thermal stability

Decomposition and thermal stability of SF, starch and blended microparticles was determined from thermogravimetric (TG) thermograms as shown in Figure 4. Both the SF and starch micropaticles did not completely decompose at a temperature of 1000°C. The TG thermograms of SF, starch and blended microparticles showed a single decomposition stage. The remaining weights at 1000°C were approximate 30 and 8% for SF and starch microparticles, respectively. The remaining weights at 1000°C of all blended microparticles were similar to the SF microparticles. The remaining weights at 1000°C of blended microparticles slightly decreased as the SF in the blended ratio decreased (Figures 4b–4d).

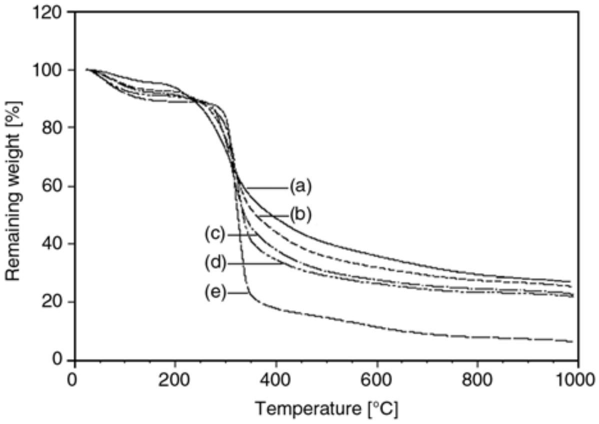

**Figure 4.** TG thermograms of (a) SF, (b) 3/1 blended, (c) 2/2 blended, (d) 1/3 blended and (e) starch microparticles

For SF microparticles (Figure 4a), it can be seen that they exhibited two major weight loss phases.

The initial weight loss at around 100°C is due to loss of moisture. The weight loss in this phase depends on the moisture content of the SF microparticles. The sharp weight loss in the second phase took place in the temperature range of 200–400°C associated with the breakdown of side chain groups of amino acid residues as well as the cleavage of peptide bonds. For starch microparticles (Figure 4e), the first phase shows the evaporation/dehydration that begins immediately after the temperature is increased and finishes at around 100°C. The moisture content of starch microparticles was higher than that of the SF microparticles. The thermal decomposition in the second phase of starch microparticles started at approximately 300°C. The TG thermograms of blended microparticles also present two phases of weight losses. The initial weight losses occurred due to moisture content exhibit between SF and starch microparticles. However, the second weight loss phase of blended microparticles did not separate.

The thermal stability of the samples can be clearly observed from differential TG (DTG) thermograms as shown in Figure 5. The small peaks in the range of 50–150°C occurred from moisture evaporation. The large peaks in the range of 150–500°C were due to decomposition of SF and starch microparticle matrices. From DTG thermograms, the temperature of maximum decomposition rate ($T_{d,\max}$) can be determined and has been summarized in Table 1. The blended microparticles had a single $T_{d,\max}$ between the SF and starch components. The $T_{d,\max}$ values of the blended microparticles slightly increased as the starch in the blended ratio increased. This supports the intermolecular interactions between SF and starch as according to the FTIR analysis.

**Table 1.** $T_{d,\max}$ of SF/starch blended microparticles

| SF/starch ratio (w/w) | $T_{d,\max}$ [°C] |
|---|---|
| 4/0 | 306 |
| 3/1 | 319 |
| 2/2 | 321 |
| 1/3 | 325 |
| 0/4 | 326 |

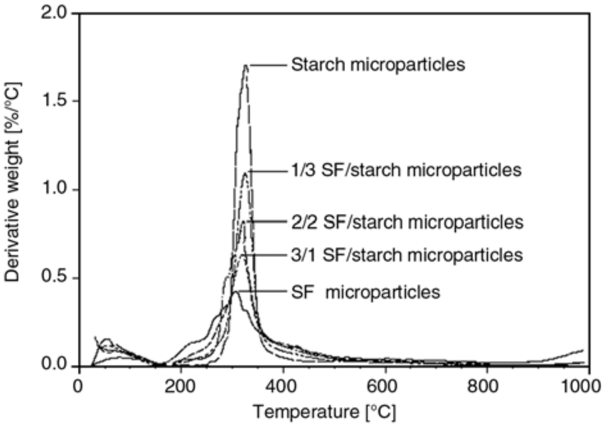

**Figure 5.** DTG thermograms of SF, starch and blended microparticles

### 3.4. Particle sizes

Particle size distributions of blended microparticles were measured by the sieving method instead of the scattering method (suspension in water) because of the partial swelling and dissolution of microparticles. The particle sizes are presented in Figure 6. It can be seen that both SF and starch microparticles showed the largest weight fraction in the range of >150 µm in size. This may be due to the rapid solidification of microparticle matrices during the emulsification-diffusion process which resulted in a large particle size. For the blended micropaticles, the particle sizes slightly decreased as the SF blended ratio increased. Both the 3/1 and 2/2 blended microparticles showed the largest weight fraction in the range of <80 µm in size. These results corresponded to their SEM images in Figure 2.

### 3.5. Dissolution test

Figure 7 shows percentage of dissolution in water of the microparticles with different incubation times. The dissolutions of all the microparticles after 3 hrs incubation showed no differences. The % dissolution values were in range of 44–64%. While for the incubation time of 6 hrs, the dissolutions of both SF and starch microparticles were nearly complete (91 and 95%, respectively). All blended microparticles had lower % dissolution values than those of SF and starch microparticles. The interactions between SF and starch in the blended microparticles may decrease microparticle dissolution. The 1/3 (w/w) SF/starch blended microparticles show the lowest % dissolution. This can be explained from the FTIR analysis, the 1/3 (w/w) SF/starch blended microparticles contained the largest water-insoluble or β-sheet form of SF

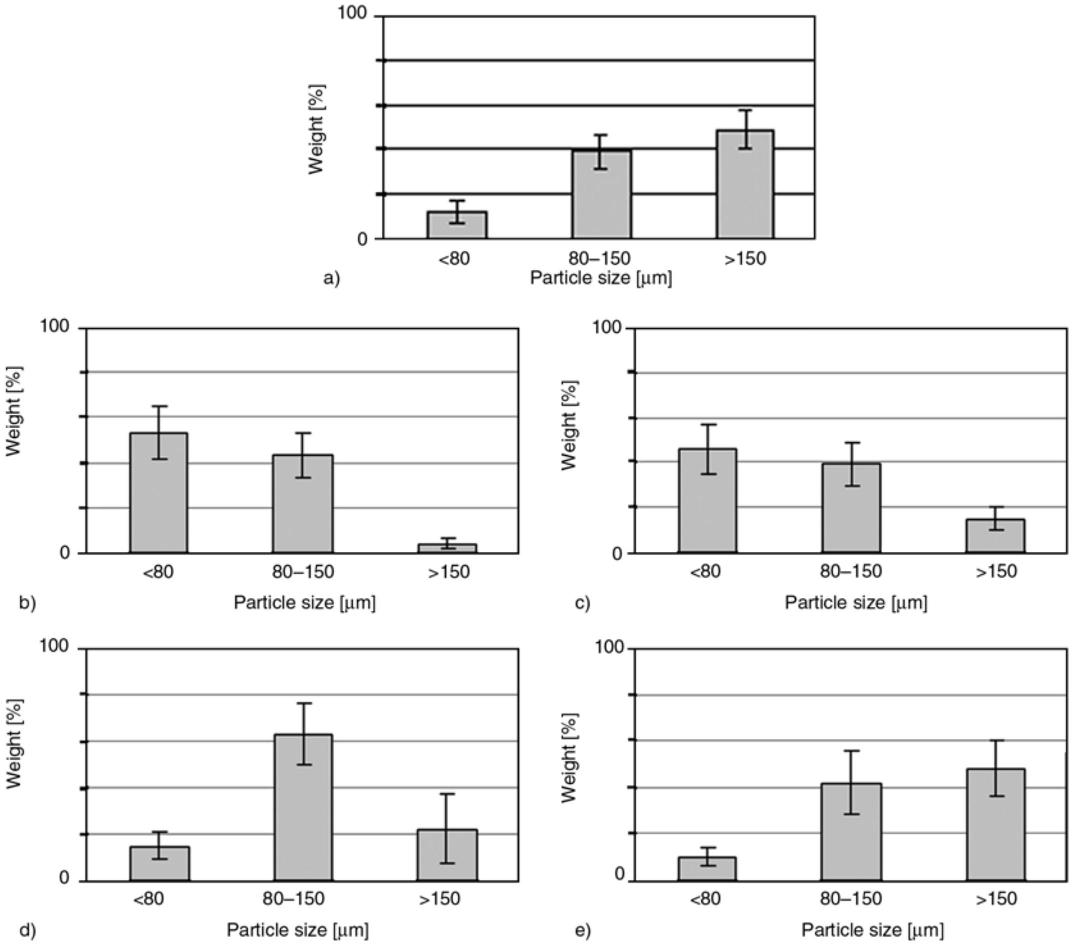

**Figure 6.** Particle size distributions of (a) SF, (b) 3/1 blended, (c) 2/2 blended, (d) 1/3 blended and (e) starch microparticles. Error bars are standard deviations ($n = 3$).

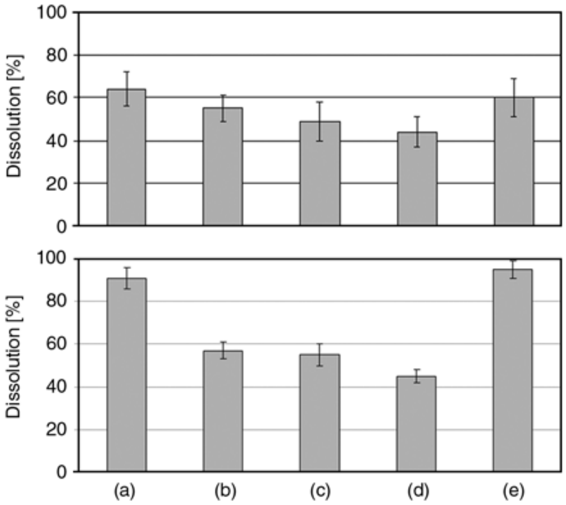

**Figure 7.** Dissolutions in distilled water of (a) SF, (b) 3/1 blended, (c) 2/2 blended, (d) 1/3 blended and (e) starch microparticles for incubation times of 3 hrs (top) and 6 hrs (bottom). Error bars are standard deviations ($n = 3$).

microparticle matrices. The results suggest that the % dissolution can be controlled by adjusting the blended ratio. This is an important advantage for drug delivery application with controllable drug release rate.

## 4. Conclusions

The SF/starch blended microparticles with different blended ratios were successfully prepared by the W/O emulsion solvent diffusion method. The SF and starch solutions were firstly blended before preparing the blended microparticles. Using FTIR and TG analyses, the intermolecular interactions which exist between SF and starch molecules were determined. The SF conformation changes from random coil to β-sheet form and increasing SF thermal stability can be induced by blending with starch. The increase of starch ratios in the blended microparticles can increase interactions between SF and starch. Blended microparticles with a spherical shape can produce with appropriate blended ratio. The % dissolution in water of blended microparticles strongly depended upon the blended ratio.

These SF/starch blended microparticles with different random coil/β-sheet form contents, thermal stabilities and % dissolutions might be of interested for use as controlled-release drug delivery systems.

## Acknowledgements

This work was supported by the Division of Research supporting and Extension services, Mahasarakham University, fiscal year 2010 and the Center of Excellence for Innovation in Chemistry (PERCH-CIC), Commission on Higher Education, Ministry of Education, Thailand. Appreciation is also expressed to Dr. Jolyon Dodgson, Faculty of Science, Mahasarakham University for helping to improve the manuscript.

## References

[1] Vepari C., Kaplan D. L.: Silk as a biomaterial. Progress in Polymer Science, **32**, 991–1007 (2007). DOI: 10.1016/j.progpolymsci.2007.05.013

[2] Zhu Z. H., Ohgo K., Asukara T.: Preparation and characterization of regenerated *Bombyx mori* silk fibroin fiber with high strength. Express Polymer Letters, **2**, 885–889 (2008). DOI: 10.3144/expresspolymlett.2008.103

[3] Kim K-H., Jeong L., Park H-N., Shin S-Y., Park W-H., Lee S-C., Kim T-I., Park Y-J., Seol Y-J., Lee Y-M., Ku Y., Rhyu I-C., Han S-B., Chung C-P.: Biological efficacy of silk fibroin nanofiber membranes for guided bone regeneration. Journal of Biotechnology, **120**, 327–339 (2005). DOI: 10.1016/j.jbiotec.2005.06.033

[4] Hofmann S., Wong Po Foo C. T., Rossetti F., Textor M., Vunjak-Novakovic G., Kaplan D. L., Merkel H. P., Meinel L.: Silk fibroin as an organic polymer for controlled drug delivery. Journal of Controlled Release, **111**, 219–227 (2006). DOI: 10.1016/j.jconrel.2005.12.009

[5] Wang X., Wenk E., Matsumoto A., Meinel L., Li C., Kaplan D. L.: Silk microspheres for encapsulation and controlled release. Journal of Controlled Release, **117**, 360–370 (2007). DOI: 10.1016/j.jconrel.2006.11.021

[6] Meinel L., Hofmann S., Karageorgiou V., Kirker-Head C., McCool J., Gronowicz G., Zichner L., Langer R., Vunjak-Novakovic G., Kaplan D. L.: The inflammatory responses to silk films in vitro and in vivo. Biomaterials, **26**, 147–155 (2005). DOI: 10.1016/j.biomaterials.2004.02.047

[7] Liu Y., Shao Z., Zhou P., Chen X.: Thermal and crystalline behaviour of silk fiborin/nylon 66 blend films. Polymer, **45**, 7705–7710 (2004). DOI: 10.1016/j.polymer.2004.09.005

[8] She Z., Jin C., Huang Z., Zhang B., Feng Q., Xu Y.: Silk fibroin/chitosan scaffold: Preparation, characterization, and culture with HepG2 cell. Journal of Material Science: Materials in Medicine, **19**, 3545–3553 (2008). DOI: 10.1007/S10856-008-3526-y

[9] Ma X. L., Li R., Ru L., Xu G. W., Huang Y. P.: Effect of polyaspartic acid on hydroxyapatite deposition in silk fibroin blend films. Express Polymer Letters, **4**, 321–327 (2010). DOI: 10.3144/expresspolymlett.2010.40

[10] Yeo J-H., Lee K-G., Lee Y-W., Kim S. Y.: Simple preparation and characteristics of silk fibroin microsphere. European Polymer Journal, **39**, 1195–1199 (2003). DOI: 10.1016/S0014-3057(02)00359-2

[11] Hino T., Tanimoto M., Shimabayashi S.: Change in secondary structure of silk fibroin during preparation of its microspheres by spray-drying and exposure to humid atmosphere. Journal of Colloid and Interface Science, **266**, 68–73 (2003). DOI: 10.1016/S0021-9797(03)00584-8

[12] Wenk E., Wandrey A. J., Merkle H. P., Meinel L.: Silk fibroin spheres as a platform for controlled drug delivery. Journal of Controlled Release, **132**, 26–34 (2008). DOI: 10.1016/j.jconrel.2008.08.005

[13] Lammel A. S., Hu X., Park S-H., Kaplan D. L., Scheibel T. R.: Controlling silk fibroin particle features for drug delivery. Biomaterials, **31**, 4583–4591 (2010). DOI: 10.1016/j.biomaterials.2010.02.024

[14] Deveci S. S., Basal G.: Preparation of PCM microcapsules by complex coacervation of silk fibroin and chitosan. Colloid and Polymer Science, **287**, 1455–1467 (2009). DOI: 10.1007/s00396-009-2115-z

[15] Bayram Ö. A., Bayram M., Tekin A. R.: Spray drying of sumac flavor using sodium chloride, sucrose, glucose and starch as carriers. Journal of Food Engineering, **69**, 253–260 (2005). DOI: 10.1016/j.jfoodeng.2004.08.012

[16] Loksuwan J.: Characteristics of microencapsulated β-carotene formed by spray drying with modified tapioca starch, native tapioca starch and maltodextrin. Food Hydrocolloids, **21**, 928–935 (2007). DOI: 10.1016/j.foodhyd.2006.10.011

[17] Malafaya P. B., Stappers F., Reis R. L.: Starch-based microspheres produced by emulsion crosslinking with a potential media dependent responsive behavior to be used as drug delivery. Journal of Material Science: Material in Medicine, **17**, 371–377 (2006). DOI: 10.1007/s10856-006-8240-z

[18] Fang Y-Y., Wang L-J., Li D., Li B-Z., Bhandari B., Chen X. D.: Preparation of crosslinked starch microspheres and their drug loading and releasing properties. Carbohydrate Polymers, **74**, 379–384 (2008).
DOI: 10.1016/j.carbpol.2008.03.005

[19] Elfstrand L., Eliasson A-C., Wahlgren M.: Changes in starch structure during manufacturing of starch microspheres for use in parenteral drug formulations: effects of temperature treatment. Carbohydrate Polymers, **75**, 157–165 (2009).
DOI: 10.1016/j.carbpol.2008.07.018

[20] Mundargi R. C., Shelke N. B., Rokhade A. P., Patil S. A., Aminabhavi T. M.: Formulation and *in-vitro* evaluation of novel starch-based tableted microspheres for controlled release of ampicillin. Carbohydrate Polymers, **71**, 42–53 (2008).
DOI: 10.1016/j.carbpol.2007.05.013

[21] Roy A., Bajpai J., Bajpai A. K.: Dynamics of controlled release of chlorpyrifos from swelling and eroding biopolymeric microspheres of calcium alginate and starch. Carbohydrate Polymers, **76**, 222–231 (2009).
DOI: 10.1016/j.carbpol.2008.10.013

[22] Kundu J., Patra C., Kundu S. C.: Design, fabrication and characterization of silk fibroin-HPMC-PEG blended films as vehicle for transmucosal delivery. Materials Science and Engineering: C, **28**, 1376–1380 (2008).
DOI: 10.1016/j.msec.2008.03.004

[23] Niamsa N., Srisuwan Y., Baimark Y., Phinyocheep P., Kittipoom S.: Preparation of nanocomposite chitosan/silk fibroin blend films containing nanopore structures. Carbohydrate Polymers, **78**, 60–65 (2009).
DOI: 10.1016/j.carbpol.2009.04.003

[24] Klingler C., Müller B. W., Steckel H.: Insulin-micro- and nanoparticles for pulmonary delivery. International Journal of Pharmaceutics, **377**, 173–179 (2009).
DOI: 10.1016/j.ijpharm.2009.05.008

[25] Giovagnoli S., Blasi P., Schoubben A., Rossi C., Ricci M.: Preparation of large porous biodegradable microspheres by using a simple double-emulsion method for capreomycin sulfate pulmonary delivery. International Journal of Pharmaceutics, **333**, 103–111 (2007).
DOI: 10.1016/j.ijpharm.2006.10.005

[26] Rawat A., Majumder Q. H., Ahsan F.: Inhalable large porous microspheres of low molecular weight heparin: In vitro and in vivo evaluation. Journal of Controlled Release, **128**, 224–232 (2008).
DOI: 10.1016/j.jconrel.2008.03.013

*eXPRESS Polymer Letters Vol.4, No.12 (2010) 790–797*
*Available online at www.expresspolymlett.com*
*DOI: 10.3144/expresspolymlett.2010.95*

# New ferrimagnetic biocomposite film based in collagen and yttrium iron garnet

*S. D. Figueiro*[1], *E. J. J. Mallmann*[2], *J. C. Góes*[1], *N. M. P. S. Ricardo*[3], *J. C. Denardin*[4], *A. S. B. Sombra*[1], *P. B. A. Fechine*[2*]

[1]Laboratory of Telecommunications and Materials Science and Engineering (LOCEM) – Physics Department, Federal University of Ceará – UFC, Campus do Pici, CP 12100, CEP 60451-970 Fortaleza – CE, Brazil
[2]Advanced Materials Chemistry Group (GQMAT) – Analytical and Physical-Chemistry Department, Federal University of Ceará – UFC, Campus do Pici, CP 12100, CEP 60451-970 Fortaleza – CE, Brazil
[3]Organic and Inorganic Chemistry Department, Federal University of Ceará – UFC, Campus do Pici, CP 12100, CEP 60451-970 Fortaleza – CE, Brazil
[4]Physics Department, Universidad de Santiago de Chile, USACH, Av. Ecuador 3493, Santiago, Chile

*Received 24 June 2010; accepted in revised form 25 August 2010*

---

**Abstract.** In recent years a great interest in the study of the association of magnetic with biological material for bioapplications has been observed in the literature. This work analyses the development of new magnetic biocomposite films from a magnetic ferrite and a biopolymer. Magnetic and dielectric properties of $Y_3Fe_5O_{12}$ (YIG)/collagen composite films were studied as a function of the YIG concentration. This biocomposite was also characterized by Infrared Spectroscopy (IR), Thermal Analysis (DSC and TG) and scanning electron microspcopic (SEM) methods. The magnetization and dielectric measurements were performed at room temperature. The results demonstrated that ferrimagnetic garnet (YIG) and collagen (Col) can be used to obtain a homogeneous composite. All the composite films showed a ferromagnetic behavior and they were characterized as a soft magnet material. These results show that Col-YIG biocomposites are biological films with magnetic properties that can be employed as a versatile performance materials, due to their flexible dielectric and magnetic features. They could be used as electronic devices in biological applications.

***Keywords:*** *thermal properties, polymer composite, biocomposite, magnetic properties*

---

## 1. Introduction

Magnetic particles have been studied due to their important versatility in bioapplications as magnetic resonance imaging (MRI) contrast agents, for cancer tumor detection, hyperthermia, drug delivery, selective separation and biomolecules detection [1]. For these applications, the particles must have combined properties of high magnetic saturation, biocompatibility and interactive functions at the surface [2]. The surfaces could be modified through the creation of few atomic layers of organic polymers, inorganic metallic or oxide surface. This kind of material can also be used in electronic devices as magnetic recording, microwave components and permanent magnetic devices [3]. Magnetic ceramics are used in a number of applications such as radar-signal absorbing, magnetic printing, magnetic levitation etc. Yttrium iron garnet (YIG) is a good example of this. It is frequently used in microwave device applications such as mobile communication systems or satellite broadcast systems [4]. This ferrimagnetic garnet has cubic structure (space group Ia3d) and formula $Y_3Fe_5O_{12}$. A new generation of devices (such as delay lines, tun-

---

[*] Corresponding author, e-mail: fechine@ufc.br

ing filters and oscillators, isolators and bubble-storage memory units) has been developed on YIG basis [5, 6].

There is a lot of research on the association of magnetic with biological materials. For example, Kim and co-workers [7] have obtained microspheres of $Fe_3O_4$ encapsulated with chitosan as a MRI image contrast, while Jain and co-workers [8] obtained magnetic nanoparticles coated with Oleic-Pluronic for sustained delivery of cancer agents. Matsumine and co-workers [9] have developed a new hyperthermic treatment modality using magnetic materials (calcium phosphate cement containing $Fe_3O_4$) for metastatic bone tumors.

In this sense, biological molecules are important to change the magnetic component into a bio-inert composite. Collagen is the most abundant of the fibrous proteins and it constitutes more than 25% of the protein mass in the human body. It constitutes part of the fibrous connective tissues of skin, bones, tendons, cartilages, blood vessels, and teeth. Individual molecules of collagen, which are semi flexible rods ~280 nm in length and ~1 nm in diameter, undergo self-assembly to form interwoven network-like structures, ranging from long fibrils to complex structures [10]. They could be used to obtain magnetic composite films with new properties.

This study reports on the synthesis, structure and dielectric-magnetic behavior of the biocomposite material obtained from a ferrite (YIG) and a collagen membrane. Through experimentation we confirm the interaction between ferrite particles and collagen to obtain a natural composite with magnetic properties.

## 2. Material and methods

### 2.1. Ferrimagnetic particle

The preparation of the ferrimagnetic particles was performed by methods used by Fechine and co-workers [11], where stoichiometric amounts of $Y_2O_3$ (99.99%, Aldrich) and $Fe_2O_3$ (99.00%, Aldrich) were used in the YIG preparation. The material was grounded on a Fritsch (Idar-Oberstein, Germany) Pulverisette 6 planetary mill in sealed stainless steel vials (221.69 $cm^3$) and balls (ø10 mm) under air in weight ratio 1/9 (wt. of mixture powder/wt. of balls). Mechanical alloying was performed for 1h of milling with 370 rpm. After this, the powder was submitted to calcination in air at 1150°C for 5 h. The reaction occurring during calcination can be summarized as shown by Equation (1):

$$3Y_2O_3 + 5Fe_2O_3 \rightarrow 2Y_3Fe_5O_{12}\ \text{(YIG)} \qquad (1)$$

### 2.2. Preparation of soluble collagen

The anionic collagen was prepared from intestinal bovine serosa by selective hydrolysis of amide groups using 50 g of intestinal bovine serosa, in the wet state and treated at 20°C for 72 h with an alkaline solution (3 ml of solution/g of tissue), salts (chlorides and sulfate), bases of alkaline ($K^+$ and $Na^+$) and alkaline earth metals ($Ca^{2+}$). The materials obtained were equilibrated with a solution containing $Na_2SO_4$, NaCl, KCl and $CaSO_4$ (6 ml of solution/g of tissue) for 12 h and the salt excess was removed as described earlier [12]. The materials was suspended in deionized water, had its pH adjusted at 3.5 with pure acetic acid and the mixture was homogenized in a blender. The soluble collagen gels concentration was 8 $mg\cdot g^{-1}$.

### 2.3. Preparation of collagen-YIG films (Col-YIG)

YIG ferrite mass (320, 480 and 640 mg) was dispersed in 40 g of the anionic soluble collagen (1:1, 1:1.5 and 1:2 Col:YIG proportions, respectively) by sonication for 3 min (1s on, 2s off) 70% in iced water bath, using a Branson (Danbury, CT, USA) Sonifier Model W-450D. The homogeneous emulsions were casted in acrylic mould and dried in laminar flow air. The samples were designed collagen, Col 1:1, Col 1:1.5 and Col 1:2.

### 2.4. Film thickness

The film thickness was measured using a Micrometer (Model 549E, Testing Machines Inc, Mineola, LI, NY). The thickness measurements were taken at 10 different points along the gauge length of each specimen and the main values were taken.

### 2.5. X-ray diffraction

The X-ray film diffraction (XRD) patterns were obtained at room temperature (300 K) in a Rigaku

(Tokyo, Japan) X-ray powder diffractometer operating at 40 kV/25 mA, using $CuK_\alpha$ radiation. The diffraction patterns were carried out using Bragg-Brentano geometry in continuous mode with speed of 0.5°/min and step size of 0.02° (2θ) in the angular range 20–60° (2θ).

## 2.6. FT-infrared spectroscopy

Fourier Transform Infrared (FTIIR) spectra were recorded using ATR regime using a SHIMATZU FTIR-283B spectrophotometer in the wave number region of 400–4000 $cm^{-1}$.

## 2.7. Differential scanning calorimetry

Differential scanning calorimetry was carried out using NETZSCH (Selb, Germany) DSC 204 F1 Phoenix® equipment. Accurately weighed (5–8 mg) dry material was placed in an aluminium cup and hermetically sealed. An empty cup was used as reference. Samples were analyzed under continuous flow of dry nitrogen gas at a heating rate of $20°C \cdot min^{-1}$ from 25 to about 200°C.

## 2.8. Thermogravimetric analysis

Thermogravimetric analysis (TG) of collagens and mineralized films was conducted by heating the sample up to 1000°C at the rate of $10°C \cdot min^{-1}$, using TGA Q5000 V2.1, TA Instruments (New Castle, DE, USA). The films were sealed in an aluminum pan and heated at the rate of $5°C \cdot min^{-1}$ in a $N_2$ atmosphere.

## 2.9. Scanning electron microscopy

Micrographs of collagen and collagen-YIG films were obtained by scanning electron microscope (SEM) (Vega XMU/Tescan, Bruker (Billerica, MA, USA)), operating with bunches of primary electrons ranging from 12 to 20 keV of rectangular samples, in samples covered with a 60 nm thick gold layer.

## 2.10. Dielectric and magnetic measurements

Dielectric measurements: real ($\varepsilon'_r$) parts of relative permittivity and loss tangent ($\tan\delta = \varepsilon''_r/\varepsilon'_r$) were performed using an Agilent (Santa Clara, CA, USA) 4294A precision impedance analyzer. It covered the region of 40 Hz–10 MHz at room temperature (300 K). This experimental part was performed in capacitors shape samples. The electrode material (Ag) was produced by the screen printing technique (Joint Metal-PC200).

The magnetization measurements were performed at room temperature with a home-made vibrating sample magnetometer (VSM). The VSM had been previously calibrated using a pure Ni wire, and after measuring the mass of each sample the magnetization was given in emu/g.

## 3. Results and discussion

All the composites (Col 1:1, Col 1:1.5 and Col 1:2) presented both crystalline and amorphous phases. For instance, Figure 1 shows the XRD obtained from composite Col 1:2. The crystalline phase is formed due to YIG (ICDD/PDF–70-0953) particles (ferromagnetic material) dispersed in the sample. It was also possible to identify a small fraction of an antiferromagnetic phase ($YFeO_3$-YFO-ICDD/PDF–86-0171). Ristić *et al.* [13] found the same result when they carried out the YIG synthesis by co-precipitation and calcination. This phase was also observed when the sol-gel method was used instead [14, 15]. In our previous work [16], we presented the YIG synthesis and made a complete structural characterization. Besides these magnetic phases, there was an amorphous phase characterized as collagen, where its major intensity was approximately in θ = 20°. This phase was identified as a broad region in the diffractogram and it was found in all the range.

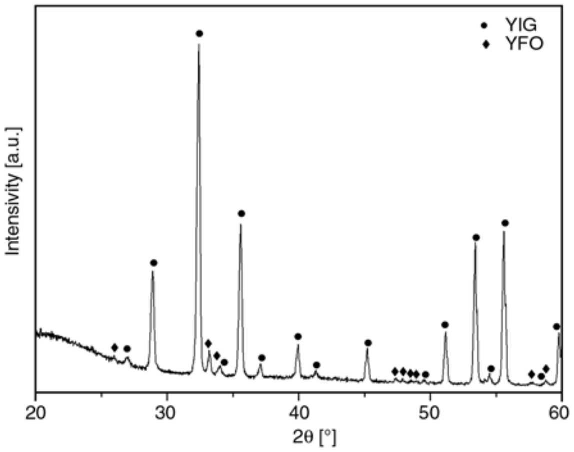

**Figure 1.** X-ray diffraction pattern of Col 1:2 biocomposite film

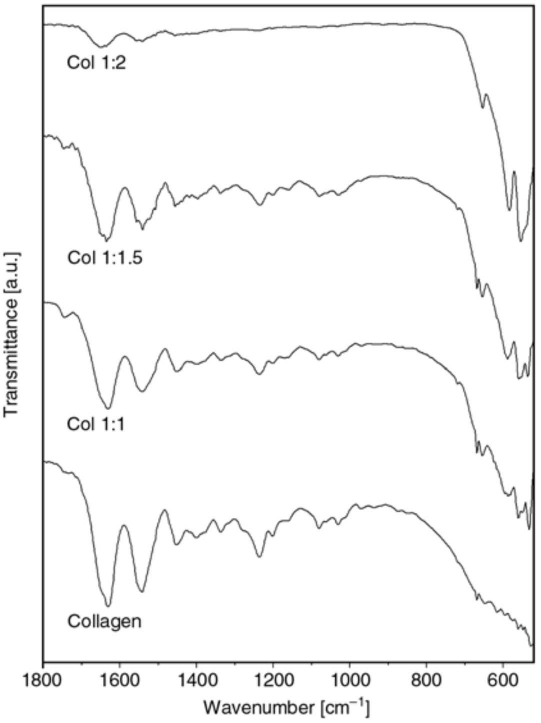

**Figure 2.** Infrared spectra of collagen and Col-YIG biocomposite films showing the finger print region

The IR spectra of the collagen and the Col-YIG composites films are shown in Figure 2. It can be observed that there are two distinct frequency regions where the bands happen for each phase of the composite. The main bands from collagen are located at 1651, 1543, 1338 and 1236 $cm^{-1}$, where the major feature of the IR spectrum of collagen film is the Amide I band between 1640 and 1660 $cm^{-1}$ [17, 18], which arises from the stretching vibration of C=O groups of amide groups in protein. The intense absorption observed at 1543 $cm^{-1}$ is due to the Amide II mode, which arises from N–H stretching vibration strongly coupled to the C–N stretching vibration of collagen amide groups. Signals in the spectral region of 1200–1400 $cm^{-1}$ absorption are generally attributed to the Amide III, arising due to the C–N stretching and N–H in plane bending from amide linkages. The C–N stretching vibration of the cyclic proline may also contribute for the absorption at 1454 $cm^{-1}$. The absorption seen at 1338 $cm^{-1}$ is attributed to $CH_2$ wagging vibration of the proline side chain.

The Col-YIG films presented the same bands observed for the collagen, as shown in Figure 2. However, one can observe three new bands in 654, 584 and 553 $cm^{-1}$. They belong to the ferrite ($Y_3Fe_5O_{12}$) used to perform the magnetic composite film. These modes are associated with the asymmetric stretching ($\upsilon_3$) of the tetrahedron (Fe–O bond) [16].

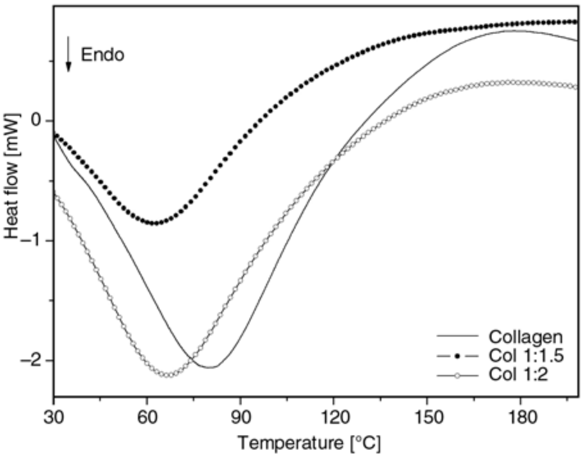

**Figure 3.** DSC curves of the Col-YIG biocomposite films

The DSC scans in Figure 3 show that collagen matrix of all samples are characterized by an endotherm peak. It is due to the denaturation process of collagen molecules and it is hydration dependant. For collagen film, the denaturation temperature is 79.7°C. For Col-YIG composites, Col 1:1.5 and Col 1:2, a decrease on this temperature was observed (62.3 and 66.7°C, respectively). These results show that YIG addition decreases the thermal stability of the collagen molecules. These results may be related to the shrinkage of the collagen matrix that is observed macroscopically.

As shown in Figure 4, the TG curves of collagen film were divided into three regions: Evaporation of absorbed water occurred from room temperature to 200°C, the thermal decomposition of collagen happened from 250 to 380°C, in which the weight

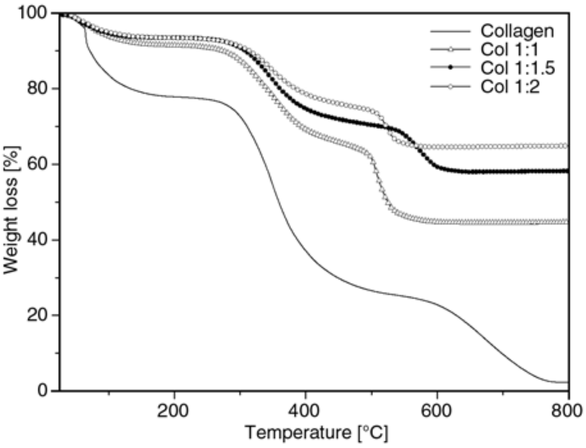

**Figure 4.** Thermogravimetric analysis of the Col-YIG biocomposite films

loss curve plateau appeared at over 550°C. The residue at 800°C was attributed to the weight of YIG in the sample. From Figure 4, one can see that the degradation temperatures vary from 351°C for collagen to 341°C for Col 1:1, 347°C for Col 1:1.5 and 346°C for Col 1:2, which suggests a decrease on thermal stabilization of collagen molecules. The amount of YIG in composite varies from 42.5% in Col 1:1 film to 56.5% in Col 1:1.5 and to 64,6 % in Col 1:2 composite. These results suggest that content higher of YIG in the composite tends to saturation.

Figures 5a, 5b and 5c show the SEM micrographs recorded on biocomposite films. The YIG particles were identified as almost uniform grains and exhibited a quasi-globular morphology. The presence of agglomerated grains was also observed in all samples. The microstructure of Col 1:1, Col 1:1.5 and Col 1:2 films were shown as particles dispersed in the polymeric matrix. Col 1:1 (Figure 5a), the sample with minor YIG quantity showed more dispersed grains than in the other films. It was also possible to observe composite phases (polymer and ferrite particles), i. e., YIG particles involved by collagen protein (or on its surface) to obtain the magnetic biocomposite film. As one can see, there were morphology changes due to the increase of YIG concentration in the film. The other samples (Col 1:1.5 and Col 1:2, Figures 5b and 5c, respectively) presented the same behavior, where the increase of the YIG concentration caused a rise of agglomerated regions.

In Figure 6, dielectric measurements ($\varepsilon'_r$ and tanδ) of the collagen and biocomposites films are shown. One can notice that the collagen presents a higher relative permittivity than other films until approximately 1 MHz (10.26), and that this value drops to 9.13 at 10 MHz (Table 1). Lima and co-workers [17] found a value of 2.60 for this same film at

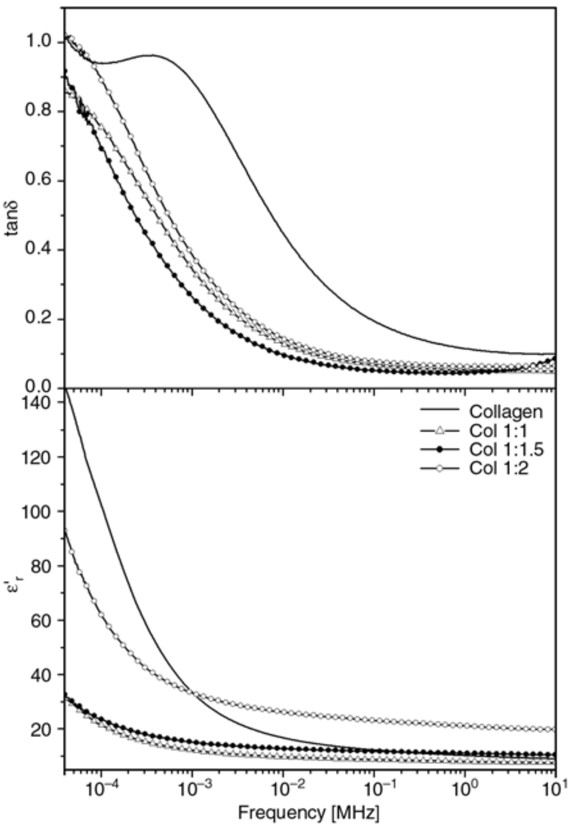

**Figure 6.** Dielectric measurements of the Col-YIG biocomposite films

**Table 1.** Thickness (*e*), relative permittivity ($\varepsilon'_r$) and loss tangent (tanδ) of the biofilms

| Samples | e [µm] | 1 kHz | | 10 MHz | |
|---|---|---|---|---|---|
| | | $\varepsilon'_r$ | tanδ | $\varepsilon'_r$ | tanδ |
| Collagen | 92.0 | 33.46 | 0.89 | 9.13 | 0.10 |
| Col 1:1 | 83.0 | 12.22 | 0.34 | 7.65 | 0.05 |
| Col 1:1.5 | 173.0 | 15.15 | 0.26 | 10.55 | 0.09 |
| Col 1:2 | 143.0 | 33.26 | 0.38 | 19.89 | 0.06 |

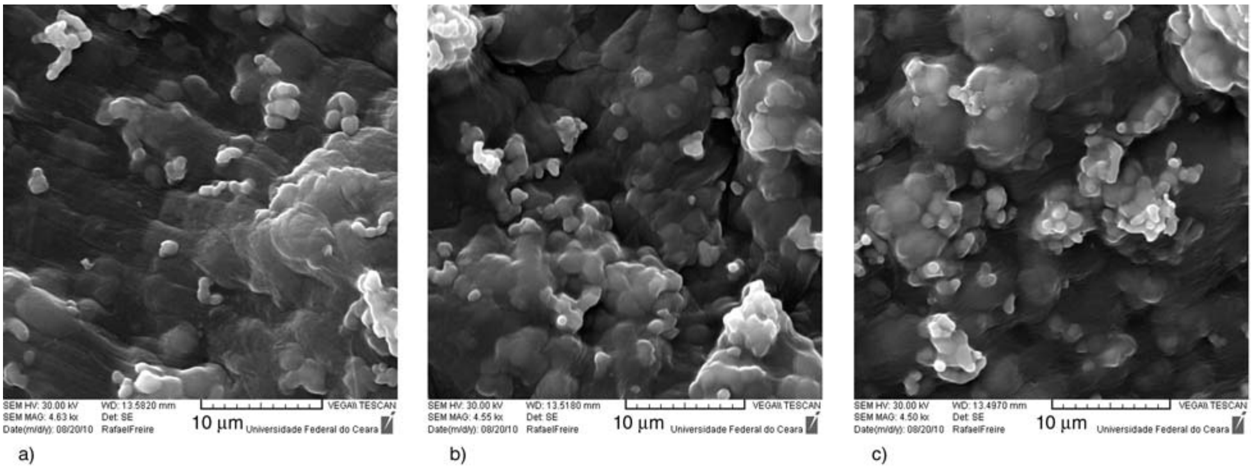

**Figure 5.** Scanning electron micrograph recorded from Col 1:1 (a), Col 1:1.5 (b) and Col 1:2 (c) films

1 MHz. This difference might have happened due to the synthetic route used to obtain the collagen, which resulted in a film with different dielectric properties. The collagen film also presented higher tanδ values when compared to biocomposites. This happens due to the large number of interfaces between the fibers and air pores that constitute the collagen network. It can also be observed that there was a shoulder at 370 Hz, which could be an evidence of the dielectric relaxation. It can be associated with the dipolar relaxation process, most probably due to the changes located at interfaces [19]. This behavior was also observed by Marzec and Pietrucha [20], when they studied the effect of different methods of collagen cross-linking on its dielectric properties as a function of the temperature.

As the biocomposites had YIG in variable proportions, it was expected a change in the dielectric behavior of the samples. Their profile was very similar to that of collagen, where the increase of the frequency decreased the $\varepsilon'_r$ and tanδ to the lowest values, when it was compared at 1 kHz and 10 MHz frequencies (Table 1). According to previous studies [11], YIG presented $\varepsilon'_r$ and tanδ values of 7.72 and 0.06 at 1 MHz, respectively. Therefore, due to the fact that the composite material had YIG and collagen, there was a modification of these dielectric features, as a result of a mutual influence (not necessarily linear). For Col 1:2, the YIG added caused a decrease of tanδ (0.06) and an increase of $\varepsilon'_r$ (19.89) at 10 MHz.

A study of the direct current (DC) magnetic features of the Col-YIG system was performed (Figure 7), where it was observed the variation in magnetization (*M*) versus the bias field (*H*) of the samples. The shape of hysteresis loops obtained from this experiment was attributed to soft ferrites due to their values of coercive field ($H_C$), remanent ($M_r$) and saturation ($M_S$) magnetization, as shown in Table 2. One can notice a decrease of the $M_S$ as a function of the collagen concentration due to the decrease of the ferrite material (YIG) in the film. For instance, the Col 1:2 film presented approximately half $M_S$ (17.12 emu/g) of the pure YIG (34.54 emu/g). However, all films presented magnetic features. The $H_C$ values showed that the increase of the collagen also makes the film harder than the ferrite alone (–11.13 Oe), where this value decreases to –40.21 Oe for the sample with minor YIG concentration (Col 1:1), see Table 2. The YIG presence in the collagen it changed into a new biocomposite with interesting magnetic behavior. Additionally, it was observed in some experiments

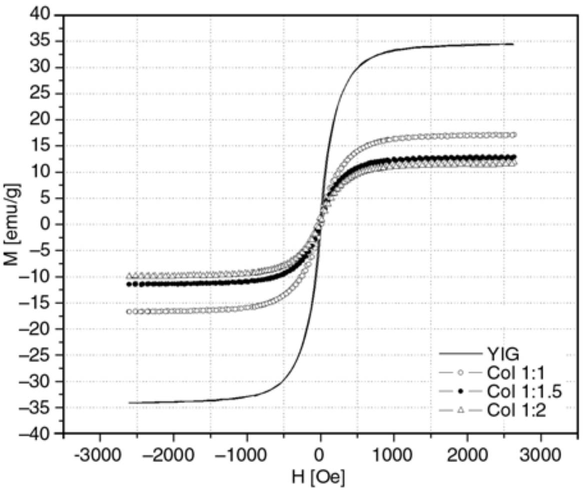

**Figure 7.** Hysteresis loop at room temperature for YIG and Col-YIG biocomposite films

**Table 2.** Properties obtained from hysteresis loop for Col-YIG system

| Samples | $H_C$ [Oe] | $M_r$ [emu/g] | $M_S$ [emu/g] |
|---|---|---|---|
| YIG (26.53 mg) | –11.13 | 1.90 | 34.54 |
| Col 1:2 (10.90 mg) | –20.54 | 1.31 | 17.12 |
| Col 1:1.5 (12.27 mg) | –28.24 | 1.32 | 12.91 |
| Col 1:1 (6.84 mg) | –40.21 | 1.46 | 11.88 |

**Figure 8.** The Col 1:1 film (a) and the experiment carried out with a neodymium-iron-boron magnet; before (b) and after (c) magnetically attracted

that they were all magnetically attracted by a permanent magnet, as shown in Figures 8a–c. In this figure, one can see the Col 1:1 film (Figure 8a) before (Figure 8b) and after (Figure 8c) magnetically attracted by a neodymium–iron–boron ($Nd_2Fe_{12}B$) magnet. This film had the minor concentration of the ferrite material of the system Col-YIG and the phenomena occurred macroscopically. Thus, this kind of biocomposite could be used as a versatile magnetic-dielectric device at radio-frequency.

## 4. Conclusions

The results of our studies demonstrated that ferrimagnetic garnet ($Y_3Fe_5O_{12}$) and collagen fiber can be used to obtain a homogeneous composite. This new material presents magnetic properties due to magnetic phase concentration in the film, and this magnetic behavior was observed by the hysteresis loops measurement. All the composite films showed a ferrimagnetic behavior and they were characterized as a soft magnet material. These results show that Col-YIG biocomposites are biological films with magnetic properties and they can be employed as a versatile performance material, due to their flexible and magnetic features. They can be used, for instance as an electronic device and for biological applications.

## Acknowledgements

This work was partly sponsored by CAPES, Funcap and CNPq (Brazilian agencies). Financiamiento Basal para Centros Cientificos y Tecnologicos de Excelencia (CEDENNA), Millennium Science Nucleus Basic and Applied Magnetism (P06-022F) and Fondecyt 1080164.

## References

[1] Shultz M. D., Reveles J. U., Khanna S. N., Carpenter E. E.: Reactive nature of dopamine as a surface functionalization agent in iron oxide nanoparticles. Journal of the American Chemical Society, **129**, 2482–2487 (2007).
DOI: 10.1021/ja0651963

[2] Gupta A. K., Gupta M.: Synthesis and surface engineering of iron oxide nanoparticles for biomedical applications. Biomaterials, **26**, 3995–4021 (2005).
DOI: 10.1016/j.biomaterials.2004.10.012

[3] Valenzuela R.: Magnetic ceramics. Cambridge University Press, New York (1994).

[4] Fechine P. B. A., Almeida A. F. L., De Oliveira R. S., Moretzsohn R. S. T., Silva R. R., Sombra A. S. B.: Bulk and patch ferrite resonator antennas based on the ceramic matrix composite: $GdIG_x$ $YIG_{1-x}$. Microwave and Optical Technology Letters, **51**, 1595–1602 (2009).
DOI: 10.1002/mop.24395

[5] Fechine P. B. A., Moretzohn R. S. T., Costa R. C. S., Derov J., Stewart J. W., Drehman A. J., Junqueira, C., Sombra, A. S. B.: Magneto-dielectric properties of the $Y_3Fe_5O_{12}$ and $Gd_3Fe_5O_{12}$ dielectric ferrite resonator antennas. Microwave and Optical Technology Letters, **50**, 2852–2857 (2008).
DOI: 10.1002/mop.23824

[6] Huang M., Zhang S. Y.: Growth and characterization of rare-earth iron garnet single crystals modified by bismuth and ytterbium substituted for yttrium. Materials Chemistry and Physics, **73**, 314–317 (2002).
DOI: 10.1016/S0254-0584(01)00365-0

[7] Kim E. H., Ahn Y., Lee H. S.: Biomedical applications of superparamagnetic iron oxide nanoparticles encapsulated within chitosan. Journal of Alloys and Compounds, **434–435**, 633–636 (2007).
DOI: 10.1016/j.jallcom.2006.08.311

[8] Jain T. K., Morales M. A., Sahoo S. K., Leslie-Pelecky D. L., Labhasetwar V.: Iron oxide nanoparticles for sustained delivery of anticancer agents. Molecular Pharmaceutics, **2**, 194–205 (2005).
DOI: 10.1021/mp0500014

[9] Matsumine A., Kusuzaki K., Matsubara T., Shintani K., Satonaka H., Wakabayashi T., Miyazaki S., Morita K., Takegami K., Uchida A.: Novel hyperthermia for metastatic bone tumors with magnetic materials by generating an alternating electromagnetic field. Clinical and Experimental Metastasis, **24**, 191–200 (2007).
DOI: 10.1007/s10585-007-9068-8

[10] Silva C. C., Pinheiro A. G., Figueiró S. D., Góes J. C., Sasaki J. M., Miranda M. A. R., Sombra A. S. B.: Piezoelectric properties of collagen-nanocrystalline hydroxyapatite composites. Journal of Materials Science, **37**, 2061–2070 (2002).
DOI: 10.1023/A:1015219800490

[11] Fechine P. B. A., Pereira F. M. M., Santos M. R. P., Filho F. P., de Menezes A. S., De Oliveira R. S., Góes J. C., Cardoso L. P., Sombra A. S. B.: Microstructure and magneto-dielectric properties of ferrimagnetic composite $GdIG_X$:$YIG_{1-X}$ at radio and microwave frequencies. Journal of Physics and Chemistry of Solids, **70**, 804–810 (2009).
DOI: 10.1016/j.jpcs.2009.03.009

[12] Bet M. R., Goissis G., Lacerda C. A.: Characterization of polyanionic collagen prepared by selective hydrolysis of asparagine and glutamine carboxyamide side chains. Biomacromolecules, **2**, 1074–1079 (2001).
DOI: 10.1021/bm0001188

[13] Ristić M., Nowik I., Popović S., Felner I., Musić S.: Influence of synthesis procedure on the YIG formation. Materials Letters, **57**, 2584–2590 (2003). DOI: 10.1016/S0167-577X(02)01315-0

[14] Vaqueiro P., Crosnier-Lopez M. P., López-Quintela M. A: Synthesis and characterization of yttrium iron garnet nanoparticles. Journal Solid State Chemistry, **126**, 161–168 (1996). DOI: 10.1006/jssc.1996.0324

[15] Kum J. S., Kim S. J., Shim I-B., Kim C. S. C. S.: Magnetic properties of Ce-substituted yttrium iron garnet ferrite powders fabricated using a sol-gel method. Journal of Magnetism and Magnetic Materials, **272**, 2227–2229 (2004). DOI: 10.1016/j.jmmm.2003.12.516

[16] Fechine P. B. A., Silva E. N., de Menezes A. S., Derov J., Stewart J. W., Drehman A. J., Vasconcelos I. F., Ayala A. P., Cardoso L. P., Sombra A. S. B.: Synthesis, structure and vibrational properties of $GdIG_X$: $YIG_{1-X}$ ferrimagnetic ceramic composite. Journal of Physics and Chemistry of Solids, **70**, 202–209 (2009). DOI: 10.1016/j.jpcs.2008.10.008

[17] Lima C. G. A., de Oliveira R. S., Figueiró S. D., Wehmann C. F., Góes J. C., Sombra A. S. B.: DC conductivity and dielectric permittivity of collagen-chitosan films. Materials Chemistry and Physics, **99**, 284–288 (2006). DOI: 10.1016/j.matchemphys.2005.10.027

[18] Madhan B., Muralidharan C., Jayakumar R.: Study on the stabilisation of collagen with vegetable tannins in the presence of acrylic polymer. Biomaterials, **23**, 2841–2847 (2002). DOI: 10.1016/S0142-9612(01)00410-0

[19] Neagu A. M., Ciuchi I. V., Curecheriu L. P., Mitoseriu L.: Impedance spectroscopy characterization of collagen samples. Journal of Advanced Research in Physics, **1**, 011006/1–011006/4 (2010).

[20] Marzec E., Pietrucha K.: The effect of different methods of cross-linking of collagen on its dielectric properties. Biophysical Chemistry, **132**, 89–96 (2008). DOI: 10.1016/j.bpc.2007.10.012

*eXPRESS Polymer Letters Vol.4, No.12 (2010) 798–808*
*Available online at www.expresspolymlett.com*
*DOI: 10.3144/expresspolymlett.2010.96*

# Affecting glass fibre surfaces and composite properties by two stage sizing application

*R.-C. Zhuang*[1]*, T. Burghardt*[2]*, R. Plonka*[1]*, J.-W. Liu*[1]*, E. Mäder*[1*]

[1]Leibniz Institut für Polymerforschung Dresden, Hohe Straße 6, 01069 Dresden, Germany
[2]Johns Manville Technical Center, 10100 West Ute Ave., Littleton CO 80127, USA

*Received 24 June 2010; accepted in revised form 3 September 2010*

**Abstract.** The influence of sizing constituent distribution on the properties of sized glass fibres (GFs) and corresponding polypropylene (PP) composites was studied by two-stage sizing application, i.e. applying silane coupling agent and polymeric film former at separate stages and with different sequences, in comparison with one-stage sizing application usually used. Surface properties of sized GFs and transverse tensile strength of unidirectional GF reinforced composites were studied using various surface and interface analysis methods and tensile testing, respectively. Two-stage technology achieved sized GFs with lower loss-on-ignition (LOI) and resulted in poor fibre-matrix adhesion strength. However, applying silane coupling agent at the first sizing stage with an increased roller speed achieved sized GFs with lower LOI but composites with mechanical properties quite close to those of composites based on one-stage technology. Moreover, the difference in surface properties of sized GFs is discussed in terms of the wetting ability difference of sizing constituents and the interactions between sizing components.

***Keywords:** polymer composites, glass fibre, polypropylene, sizing, mechanical properties*

## 1. Introduction

In last few decades, intensive research efforts have been devoted, especially, to achieve a better understanding of the interphase between reinforcement and matrix since the mechanical properties of composite materials highly depend on the interphase properties [1–3]. Interphases between reinforcement and matrix are formed by the inter-diffusion of sizing and matrix [4], resulting in different compositions and properties compared to the bulk matrix. Interphases with gradual or monotonic change of mechanical properties and composition rather than homogeneous properties are highly expected, since in such case mechanical stresses can be efficiently transferred from matrix to reinforcement and the concentration of mechanical and thermomechanical stresses at this area can be greatly avoided [5]. Recent progresses in mechanical characterisation on interphases in combination with adhesion strength measurement and real composite mechanical tests indicated the presence of an interphase with mechanical property gradients leading to high mechanical properties [6–11].

As there is a steadily increasing interest in the use of thermoplastic composites in different fields, such as construction, automotive industries and aeronautic industries, in the field of GF reinforced thermoplastic composites various strategies have been developed in order to tailor the interphase characteristics, which mainly focused on the modification of GF surface or matrix, aiming at enhancing the GF-matrix adhesion strength, such as by enhancing GF-matrix compatibility, mechanical interlocking, and acid-base interaction [1–3, 12–14]. From the viewpoint of production, on-line surface modification of the as-spun GF with an appro-

---

[*]Corresponding author, e-mail: emaeder@ipfdd.de

priate sizing (generally a mixture of silane coupling agent, polymeric film former and additives) is a straightforward strategy for tailoring the interphase properties to give cost-effective composite materials [14–25]. Thus, great attentions have been paid on the sizing structure or radial chemical composition to deepen the understanding of the correlation between the mechanical properties of composites and both the sizing and sizing technology. Post treatments and analyses [3, 26–32] on model reinforcements, especially 3-aminopropyltriethoxysilane (γ-APS) sized GF or silica, revealed that the surface of γ-APS sized model reinforcements consists of three layers, which are physically adsorbed, chemisorbed, and chemically covalent bonded polysiloxanes from air/sizing interface to sizing/GF interface [29–31]. It was found that the physically adsorbed polysiloxanes based on γ-APS have a detrimental effect on the GF-matrix adhesion strength [33]. Moreover, the sizing conditions, such as pH value and sizing concentration, can affect the detailed molecular structures of sizing and consequently the composite performance [28, 34]. For real reinforcements sized with the complete sizing formulation, it was proposed that silane coupling agent enriches on the sizing/GF interface, while the polymeric film former predominates on the sizing/air interface, hence polymeric film former and polysiloxane network form an interpenetrating network (IPN) with gradual change of chemical composition from silane coupling agent dominated phase to polymeric film former enriched phase [29, 35].

Literature addressing the formation of interphase dependence of sizing structure based on the complete sizing package is very limited [9–11, 36]. In this study, silane coupling agent and polymeric film former were applied sequentially on as-spun GF at different stages, i.e. firstly applying silane coupling agent and then polymeric film former or firstly applying polymeric film former and then silane coupling agent. Using such a strategy, one is able to 1) create silane coupling agent enriched sizing/GF interface and polymeric film former dominated sizing/air interface or inverse for the study of the interdiffusion behaviour of different sizing components during the processing, 2) study the pickup and/or adsorption/desorption behaviour of sizing components, and 3) study the influence of these two aspects on the properties of sized GFs and corresponding composites.

Furthermore, stepwise sizing application technology might lead to potential saving by reducing the LOI of GFs while maintaining the composite performance since the sizing is one of the major contributors to the cost of composites. The LOI of sized GFs can be adjusted by many factors, such as sizing application roller speed, the wetting properties (surface tension, charge, concentration, and viscosity and so on) of sizing, and drying temperature [21]. To the best of our knowledge, so far no report describes the use of multi-stage sizing application for this purpose. The idea behind this is to reduce the pickup of sizing constituents by lowering the sizing concentration.

## 2. Experimental Details

### 2.1. Materials

GF with average diameter of 15 μm (204 filaments, yarn fineness of 90 tex) were spun at the Leibniz Institute of Polymer Research Dresden using a continuous spinning device comparable to industrial ones. The take-up speed was kept constant at 750 m/min, water cooling spray was considered unnecessary in order to avoid change in concentration. The bobbin weight was kept constant at 600 g and dried at 125°C for 4 h. For the preparation of PP compatibly sized GF, maleic anhydride grafted PP (MAH-*g*-PP) dispersion (35 wt.% solid content, number average molecular weight is 81 300 g/mol) was used as film former and 1 wt.% γ-APS water solution was used as silane coupling agent at the native pH. In two stage sizing application technology (referred to as two-stage technology), the second sizing application stage (referred to as the second stage) was placed about 50 cm below the first sizing application stage (referred to as the first stage). The applicator rolls were positioned both on one side of the spread single filaments of the strand. Table 1 summarizes the information on the sizing application of the sized GFs. M1 fibre was produced by applying γ-APS solution at the first stage and PP dispersion at the second stage with sizing application conditions (applicator roll speed of 14.1 m/min) commonly used in industrial production (referred to as standard conditions), while a higher rotation speed (17.6 m/min) was applied for the first sizing applicator to give M1W fibre. M2 fibre was obtained by using reverse sizing application sequence in comparison with M1 fibre

**Table 1.** Summary of sizing application and surface properties of sized glass fibres

| GF | Sizing components and application sequence | | LOI [wt.%] | Roughness [nm] | | Contact angle with water [°] | | |
|---|---|---|---|---|---|---|---|---|
| | 1st stage | 2nd stage | | $R_q$ | $R_{max}$ | $\theta_a$ | $\theta_r$ | $\theta_a$–$\theta_r$ |
| APS | γ-APS (64–68)[1] | | 0.05±0.02 | 0.8±0.5 | 17.7±13.8 | 83.5±2.9 | 56.8±4.3 | 26.7 |
| PF | PP dispersion (33.7)[1] | | 0.23±0.01 | 2.1±1.1 | 40.5±16.0 | 58.1±2.0 | 41.6±3.9 | 16.5 |
| M1 | γ-APS | PP dispersion | 0.30±0.02 | 16.1±7.2 | 135.9±35.6 | 77.7±2.3 | 49.1±4.2 | 28.6 |
| M2 | PP dispersion | γ-APS | 0.30±0.01 | 4.9±1.5 | 67.8±32.2 | 73.2±2.2 | 45.7±2.5 | 28.5 |
| M3 | γ-APS+PP dispersion (35.3)[1] | | 0.54±0.002 | 5.8±1.8 | 74.5±19.4 | 84.5±2.1 | 58.1±2.6 | 26.4 |
| M1W[2] | γ-APS | PP dispersion | 0.37±0.003 | 18.6±2.7 | 155.1±46.1 | 84.2±3.4 | 49.2±6.2 | 35.0 |

[1] the numbers in parentheses are the surface tensions of sizing components, the unit is mN/m.

[2] using increased first applicator roll speed

while the same sizing application conditions were used. M3 fibre was spun using the one-stage technology commonly used. For a better comparison, GFs sized with γ-APS or PP dispersion were also prepared and referred to as APS and PF fibres, respectively. Homo-PP compounded with 2 wt.% MAH-*g*-PP was used as matrix for the preparation of hybrid PP/GF yarn with 50 vol.% GF for continuous fibre composites, as described in detail elsewhere [37]. The unidirectional fibre-reinforced polymer composites made of commingled yarns were processed in computer controlled identical long-term cycles (heating, consolidation, and cooling in the mould) at a temperature of 225°C and a pressure of 3 MPa.

## 2.2. Characterizations

The LOI of sized GFs was determined according to ASTM D4963-04 by means of high temperature pyrolysis at 625°C.

Atomic force microscopy (AFM, Digital Instruments D3100, Santa Barbara, USA) was used to determine the surface roughness and topography of sized GFs. The presented roughness data are averaged values based on 12 specimens each 3 on different fibres, the 2nd order plane fitting was performed prior to roughness measurement.

Electrokinetic properties of γ-APS solution, PP dispersion and corresponding sizing were studied using a Mütek PCD 03. Electrokinetic properties, Zeta-potential as a function of pH, of sized GFs were obtained by electrokinetic analysis (EKA) on an electrokinetic analyzer (Fa. Anton Paar KG, Austria).

Particle size distribution of γ-APS solution, PP dispersion and corresponding sizing was studied on a Zetasizer nano ZS (Malvern Instruments GmbH, Herrenberg, Germany).

The dynamic advancing contact angle ($\theta_a$) and receding contact angle ($\theta_r$) measurements on single GFs were performed on a tensiometer K14 (Krüss GmbH, Hamburg, Germany) using water as measurement liquid. The presented results are averaged values based on 15 specimens. The surface tensions of the aqueous solutions/dispersions were determined by using a platinum plate on the same equipment.

*XPS* investigations were performed on a Kratos AXIS Ultra X-ray photoelectron spectrometer (*XPS*). Areas of approximately 300×700 microns were analyzed with a monochromatic Al $K_\alpha$ X-ray source. The survey spectra were collected over a wide binding energy range (0–1300 eV) and were used to evaluate all of the elements present (except H and He) within the sample surface. The survey spectra were acquired at 6 areas with a pass energy of 160 eV and a step size of 1 eV. The parameters of the component peaks were their binding energy, height, full width at half maximum and the Gaussian-Lorentzian ratio.

The transverse tensile strength of unidirectional (UD) GF/PP composites was measured according to specification ISO 527 with a velocity of 1 mm/min, whereas cap strips are applied on the ends of the specimens (2×10×140 mm). The presented results are averaged values based on 10 specimens for each test series.

## 3. Results and discussion

### 3.1. Analysis on sizings

In order to better understand the formation of different sizing structures using different sizing application sequences, dynamic light scattering and particle charge detection were used to study the particle size distribution and streaming potential as a function of pH for γ-APS solution, PP dispersion

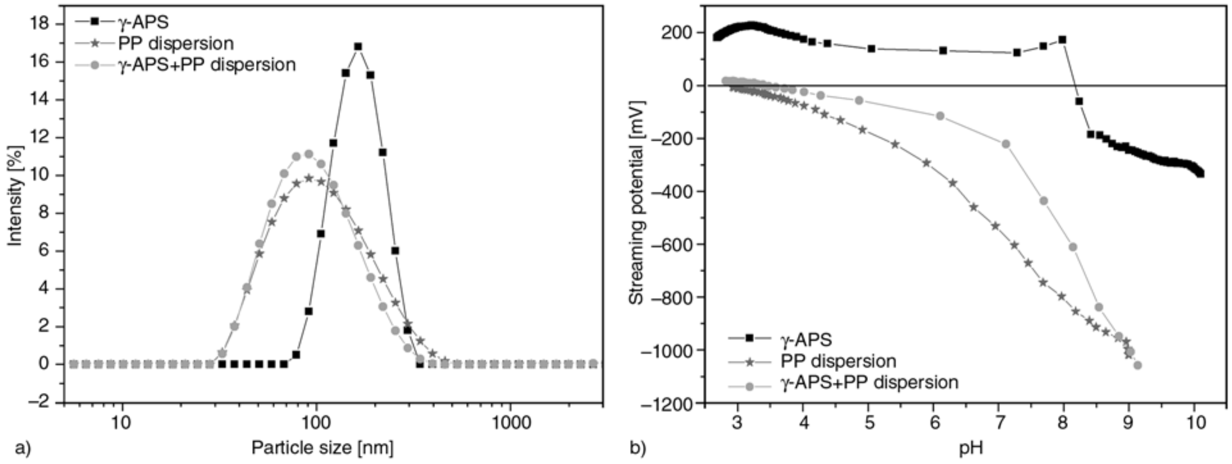

**Figure 1.** Pre-examination on γ-APS solution, PP dispersion and corresponding sizing: a) particle size distribution curves and b) streaming potential as a function of pH

and corresponding sizing, the results are shown in Figure 1a and 1b, respectively. Figure 1.a shows: 1) The hydrolyzed γ-APS molecules further oligomerized and aggregated to form aggregations with average particle diameter of around 110 nm. 2) The PP dispersion has a narrow mono-modal particle size distribution curve with a peak centered at around 90 nm. 3) Mixing PP dispersion with γ-APS solution hardly led to any apparent change, the particle size distribution of the resulting mixture is quite similar to that of pure PP dispersion. In Figure 1b, one can find that the γ-APS based micelle is negatively charged at its native pH of 10.6, the isoelectric point (IEP) of γ-APS solution is about 8.2. PP dispersion also possesses a negative streaming potential with an absolute value of 1198 mV at the native pH of 9, the IEP of PP dispersion is around pH 3. FTIR analysis on the solid part of PP dispersion (results not shown) showed the absorption band of maleic anhydride group at around 1783 cm$^{-1}$ [36]. It is known that the pKa values of succinic acid are about 4.2 and 5.5 [38], however the dense PP particles may limit the accessibility of acid groups [39] , hence that the IEP of PP dispersion shifts to a lower pH range is reasonable. It is noted that adding γ-APS solution to PP dispersion led to a little bit more negative streaming potential of 1248 mV maybe due to the change of pH, meanwhile the IEP shifts to more basic of pH 3.8.

## 3.2. Surface properties of sized GFs

The pick-up of sizing constituents onto GFs was studied by pyrolysis at 625°C. Table 1 summarizes the average LOI values of differently sized GFs. It is noted that APS and PF fibres have LOI of 0.05 and 0.23 wt.%, respectively. One-stage technology resulted in M3 fibre with the highest LOI value of 0.54 wt.%. Two-stage technology led to sized GFs, M1, M1W and M2 fibres, with lower LOI values in the range of 0.30–0.37 wt.%. Additionally, it is noted that either applying firstly γ-APS solution (M1 fibre) or applying firstly PP dispersion (M2 fibre) did not have a great influence on the LOI value of sized GFs, both sequences resulted in sized GFs with LOI value at the same level.

Tapping mode AFM was used to study the surface morphology of sized GFs, Figure 2 presents the AFM height images and the corresponding schematic topographies. Surface roughness in terms of root mean square roughness ($R_q$) and maximum roughness ($R_{\max}$) with their standard deviation is summarized in Table 1. The surface of APS fibre is quite smooth with $R_q$ of 0.8 nm and featureless except γ-APS based polysiloxane islands. PF fibre also possesses a relative smooth surface, the $R_q$ and $R_{\max}$ are 2.1 and 40.5 nm, respectively. Two-stage technology by applying PP dispersion at the second stage resulted in sized GFs with rough surfaces characterized by pine bark-like morphology, both M1 and M1W fibres have high $R_q$ and $R_{\max}$ values with high standard deviation, the latter one has slightly higher $R_q$ and $R_{\max}$ values. Two-stage technology by applying PP dispersion at the first stage and one-stage technology achieved sized GFs with smoother surface, whereas their surfaces are still rougher than those of APS and PF fibres, but quite similar to that of one-stage technology. The differ-

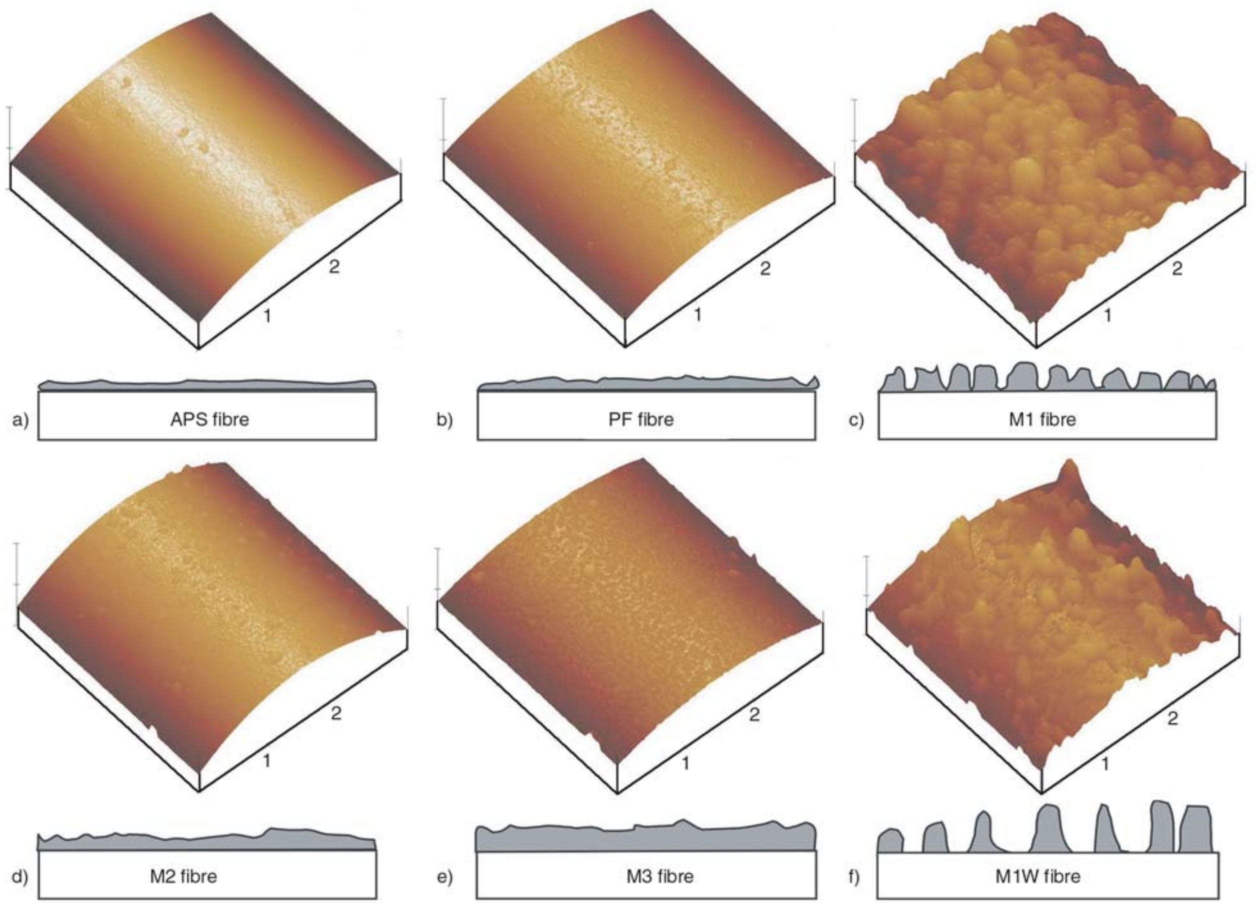

**Figure 2.** AFM height images and schematic topographies of PP compatibly sized GFs in comparison with only APS and only PP dispersion sized GFs. For all images, the Z data scale is 250 nm, the scan size is 3×3 µm

ence in surface roughness for differently sized GFs could be related to the surface tension difference of sizing constituents and the high melting point of PP particles. γ-APS solution has a higher surface tension (64~68 mN/m) compared to PP dispersion (33.7 mN/m), the wetting ability of γ-APS solution on the as-spun GFs was not at the same level as that of PP dispersion. As a result of this, the surface of γ-APS solution pre-sized GFs can not be regarded as chemically homogeneous as the surface of PP dispersion pre-sized GFs. Therefore, the further pickup of PP dispersion on the γ-APS pre-sized GFs preferentially took place on the locations of better wettability, causing the segregation of PP dispersion on specific locations. Additionally, the melting point of PP particles of the PP dispersion used is about 163°C which is higher than the drying temperature of sized GF bobbins, therefore the resulting morphology was mostly retained during the drying, thus the M1 and M1W fibres have rougher surface compared to PF and M2 fibres (cf. Figure 2). The mixture of γ-APS and PP dispersion has a surface tension of about 35.3 mN/m, this is quite close to the surface tension of pure PP dispersion, hence the mixture could also homogeneously wet the surface of the as-spun GF and the resulting M3 fibre has a smooth surface.

Dynamic contact angle measurements of single fibres using water as measurement liquid were performed to evaluate the hydrophobicity of sized GFs. Advancing contact angle ($\theta_a$), receding contact angle ($\theta_r$) and hysteresis ($\theta_a$–$\theta_r$) of all sized GFs are summarized in Table 1. It is noted that $\theta_a$ of APS fibre is about 83.5°. This value is higher than the expected one (40–68°) [40, 41] but still reasonable basing on following two reasons. (i) It was proposed that the electron pair on the amine nitrogen could point toward the glass surface, sideways, or toward free air [3, 26–28, 34, 42–44]. (ii) Using the combination of XPS and time-of-flight secondary ion mass spectroscopy (ToF-SIMS), Jones and coworkers revealed that a small amount of polydimethylsiloxane may be introduced into γ-APS in production and transferred onto the surface of only γ-APS sized GF [30, 31]. In the case of PF fibre, a more hydrophilic surface was formed, $\theta_a$ and $\theta_r$ are 58.1 and 41.6°, respectively. This arises from the polar nature of the surface of PP particles which are stabilized with alkyl polyethylene glycol ether and anionic carboxylate group of MAH-*g*-PP. $\theta_a$ of M1 and M2 fibres is in the range of 73 to 77° and smaller than that of M3 fibre (84.5°). It suggests that under standard conditions two-stage technology resulted in sized GFs with more hydrophilic surface in comparison with one-stage technology. Increasing the first applicator roll speed (M1W fibre) obtained a little bit more hydrophobic surface compared to M1 fibre, $\theta_a$ increases from 77.7 to 84.2°, which likely correlates with the increased sizing uptake. On the other hand, the hysteresis increases too, which most likely is due to the rougher surface of M1W fibre when the similarity in the surface chemical composition (see XPS results) between M1 and M1W fibres is taken into consideration.

Besides surface topography and hydrophobicity, the chemical composition and the functional groups of the outermost surface of sizings are also of great importance in determining GF-PP interaction mechanisms, which can affect the GF-matrix adhesion strength level. Hence, XPS was used to determine the surface compositions of sized GFs, while Zeta-potential measurements were used to derive information about the functional groups at the outermost surface of sized GFs.

The normalized surface compositions of sized GFs are calculated using Ca as reference and are presented in Table 2. Ca was used as reference instead of Si, since the C/Si ratios for all sized GFs are below 10 (cf. Table 2), which is indicative of thin and/or inhomogeneous sizing coverage of the whole GF-surface [35]. It is noted that γ-APS sized fibre has high Ca, B, and Al contents, suggesting that the sizing of APS fibre is very thin when the smooth and good coverage surface of APS fibre (cf. Figure 2) is taken into consideration. Moreover, the high N content of APS fibre confirms the formation of the γ-APS based sizing layer on the surface of GF. Compared to APS fibre, PF fibre possesses higher C and Na contents but lower N content as well as lower Ca, B, and Si contents. Additionally, PF fibre has about thirteen times higher C/Ca ratio and one time higher C/Si ratio while the Si/Ca ratio drops to 3.3. These indicate that the sizing of PF fibre is still relatively thin but thicker than that of APS fibre. The presence of N atoms on the surface of PF fibre can be attributed to small amine molecule additives observed by NMR analysis on the acetone soluble part of PP dispersion (data not shown here) or the contamination from air. The average surface compositions of M1 and M1W fibres are quite similar, the main difference is that M1W fibre has a higher Ca content, this may be related to the rougher surface of M1W fibre (cf. Figure 2). Correspondingly, the O/Ca, C/Ca and Si/Ca ratios of M1W fibre are lower than those of M1 fibre. On the other hand, the N/Ca ratio of M1W fibre is quite close to that of M1 fibre, one can conclude that increasing the rotation speed of the first applicator increased the pickup of γ-APS. This is verified by the Zeta-potential stated below (cf. Figure 3). Compared to M1 and M1W fibres, M2 fibre exhibits reduced C content and increased

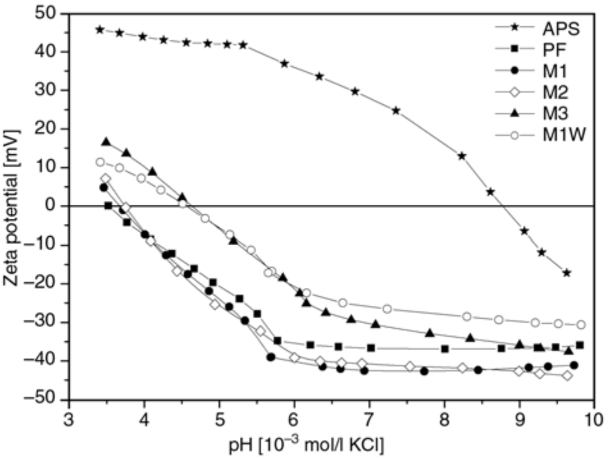

**Figure 3.** Zeta-potential as a function of pH for differently sized glass fibres

**Table 2.** Absolute and normalized average surface compositions (in at%) of sized glass fibres

| GF | Na | O | N | Ca | C | B | Si | Al | Mg | Na/Ca | O/Ca | N/Ca | C/Ca | Si/Ca | C/Si |
|---|---|---|---|---|---|---|---|---|---|---|---|---|---|---|---|
| APS | 0.2 | 39.9 | 2.2 | 4.0 | 30.4 | 3.1 | 15.4 | 3.6 | 1.2 | 0.05 | 10.0 | 0.55 | 7.6 | 3.8 | 2.0 |
| PF | 0.7 | 34.7 | 0.5 | 3.3 | 43.8 | 2.2 | 10.9 | 3.4 | 0.6 | 0.21 | 10.5 | 0.15 | 13.3 | 3.3 | 4.0 |
| M1 | 0.3 | 23.2 | 0.7 | 1.9 | 62.2 | 1.3 | 7.5 | 2.1 | 0.8 | 0.15 | 12.2 | 0.37 | 32.7 | 3.9 | 8.3 |
| M2 | 0.3 | 28.3 | 0.6 | 2.7 | 53.5 | 1.6 | 10.2 | 2.0 | 0.8 | 0.11 | 10.5 | 0.22 | 19.8 | 3.8 | 5.2 |
| M3 | 0.4 | 28.3 | 1.4 | 2.0 | 61.7 | 1.4 | 7.9 | 2.0 | 0.8 | 0.20 | 14.2 | 0.70 | 30.8 | 4.0 | 7.8 |
| M1W | 0.3 | 21.9 | 0.8 | 2.5 | 63.3 | 1.2 | 7.3 | 2.0 | 0.7 | 0.12 | 8.8 | 0.32 | 25.3 | 2.9 | 8.7 |

Si as well as the least amount of N content on the surface. Correspondingly, the normalized atom contents dropped except the Si/Ca ratio. This observation is interesting since it was expected that γ-APS based oligo- or polysiloxanes would enrich in the outermost surface of M2 fibre, which was spun by applying γ-APS solution at the second stage. It is indicative of possible migration of γ-APS based oligo- or polysiloxanes towards GF/sizing interface, which is confirmed by EKA. M3 fibre shows the highest N content and N/Ca ratio of 0.70. Taken into account its smooth surface and high LOI value, it is sure that a thicker sizing with homogeneous coverage was formed on M3 fibre when the complete sizing formulation was applied using one-stage technology.

Compared to XPS which reveals the average chemical composition for 8 nm information depth with a take-off-angle of 90°, EKA can provide indirect information of functional groups on the outermost surface of sizing in our case by measuring the Zeta-potential as a function of pH for differently sized GFs (shown in Figure 3). It is widely known that the IEP of non-sized or water sized E-glass is around 2 due to the enrichment of acidic silanol groups on the surface [45]. Compared to non-sized E-glass, APS fibre at the native pH of 5.7 has a positive Zeta-potential, which is related to the protonation of amino groups, meanwhile the IEP of APS fibre shifts to pH 8.5 owing to the basic amino groups. On the other hand, the IEP of APS fibre is lower than the pKa of aminopropyl group (9.8~10.6), indicating that the acidic silanol groups of either GF surface or γ-APS based components are still present on the APS fibre surface. The IEP of PF fibre shifts to pH of 3.5 compared to that of non-sized GFs, which is very close to the IEP of PP dispersion (Figure 1b), suggesting a good coverage of PP film former on as-spun GFs. The application of complete sizing formulation on the GF shifts the IEP further to more basic values of about pH 4.6, which is also quite close to the IEP of aqueous sizing. The low IEP value of M3 fibre suggests that the major fraction of outermost surface is PP film former. The driving force for this could be attributed to the good affinity between GF surface silanol groups and γ-APS based components and the low surface free energy of PP film former. The electrokinetic properties of M1 and M2 fibres are very similar to those of PF fibre. This is reasonable for M1 fibre since the PP dispersion was applied at the second stage, but it is especially interesting in the case of M2 fibre and it is consistent with XPS and water contact angle measurements that only a small amount of γ-APS based components was picked up and the adsorbed γ-APS based components diffused to GF surface through the PP film former coverage. It is noted that the electrokinetic properties of M1W fibre is similar to that of M3 fibre, this is indicative of the increase in the uptake of γ-APS based components at the first stage by increasing the rotation speed of the first applicator. Another possible explanation is that the low coverage of PP film former on the surface of M1W fibre could expose the γ-APS based components preferably adsorbed on the surface of GF to the medium.

Based on the above investigations, the formation mechanism of sizing for different sizing application technologies is briefly outlined in following. For one-stage technology, the mixture of γ-APS and PP dispersion has low surface tension and the highest concentration, thus leads to sized GFs with the highest LOI and smooth surface. Meanwhile, the difference in the nature for γ-APS and PP dispersion causes γ-APS based components enrichment in the GF/sizing interface and PP dispersion domination in the sizing/air interface, thus the IPN of γ-APS based components and PP dispersion is created, which is confirmed by our previous work [36]. In the case of two-stage technology, applying γ-APS solution at the first stage with normal applicator rotation speed leads to the extreme uptake of γ-APS, which is then mainly confined in the vicinity of sizing/GF interface and can not diffuse outwards to sizing/air interface due to the good affinity between γ-APS and GFs. However, with increased applicator rotation speed, the uptake of γ-APS is enhanced resulting in the formation of IPN of γ-APS based components and PP dispersion. On the other hand, applying γ-APS solution at the second stage, γ-APS based components can diffuse towards the sizing/ GF interface driven by the good affinity between γ-APS and GFs, promoting the formation of the IPN of γ-APS based components and PP dispersion.

### 3.3. Mechanical properties of unidirectional composite materials

The effect of the sizing structure on GF-matrix adhesion strength was studied by transverse tensile test on unidirectional GF reinforced PP (UD GF/PP) made from on-line commingled GF/PP- hybrid yarn of 50 vol.% GF, since the transverse tensile test is very sensitive to the interfacial bonding between GF and matrix. Figure 4 clearly shows that the sizing structure has a significant influence on the mechanical properties of UD GF/PP composites. Two-stage technology using standard conditions could not obtain UD GF/PP composites with transverse tensile strength comparable to UD GF/PP based on one-stage technology, for the latter one the strong GF-matrix adhesion strength relates to the high LOI and the IPN of γ-APS based polysiloxane and PP film former of M3 fibre [29, 35]. Applying γ-APS solution at the first stage resulted in composites with transverse tensile strength of 4.2 MPa accompanied by 0.3% elongation at break. This extremely low transverse tensile strength value suggests a poor GF-matrix adhesion strength, which is mainly due to the absence of covalent bonding between matrix and GF. Applying γ-APS solution at the second stage improved the GF-matrix adhesion, the transverse tensile strength increased up to 14.1 MPa, this value is still low compared to that of the composite based on one-stage technology. However, it evidences that γ-APS based components could migrate towards the sizing/GF interface and condense there leading to the formation of covalent bonds, although the intensity or the density of such covalent bonds is still low. The transverse tensile strength of M1W/ PP composites increases up to 20.5 MPa, the elongation at break also raises to 1.2%, these values are still lower but quite close to those of M3/PP composites. It suggests that increasing the rotation speed of applicator resulted in enhanced intensity of covalent bond. On the other hand, the increased standard deviation of transverse tensile strength and elongation at break relates to the rough surface of M1W fibre.

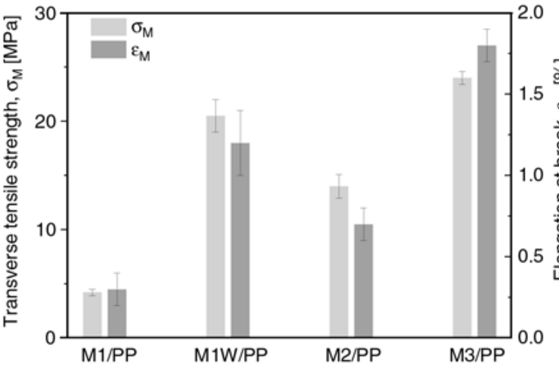

**Figure 4.** Transverse tensile strength and elongation at break of UD GF/PP composites

## 4. Conclusions

In order to achieve a better understanding of the sizing structure formation and its influence on the fibre-matrix adhesion strength, 3-aminopropyltriethoxysilane (γ-APS) and polypropylene (PP) dispersion were separately applied on as-spun glass fibres (GFs) at different stages and with different sequences. The surface properties of differently sized GFs as well as the transverse tensile strength of the corresponding unidirectional (UD) GF/PP composites were studied. It was found that the sizing application conditions have a great effect on the formation of sizing structure and, consequently, the GF-matrix adhesion strength. For two-stage technology by applying γ-APS solution at the first stage with sizing application conditions commonly used in industrial production (referred to as standard conditions), an extremely poor GF-matrix adhesion strength was observed due to the low uptake of γ-APS. However, this detrimental effect can be counteracted by increasing the uptake of γ-APS, the UD GF/PP composites obtained by applying γ-APS solution at the first stage with increased applicator roll speed achieved mechanical properties a little bit lower compared to composites prepared by one-stage sizing application of whole sizing formulation. This is attributed to the enhanced covalent bonding and base-acid interaction between the amino group of γ-APS and the anhydride group of matrix modifier. On the other hand, applying PP dispersion at the first stage, out of expectation, can obtain better GF-matrix adhesion compared with applying γ-APS solution at the first stage using standard conditions, even though the uptake of γ-APS was low at the second stage. This emphasizes the importance of the formation of an interpenetrating network of PP and polysiloxane. In future work will be devoted to better understand the influence of sizing structure on the local interphase properties, such as mechanical and thermal properties, by using nano-indentation and nano-TA.

## Acknowledgements

RCZ would like to thank Johns Manville and Leibniz Institute of Polymer Research Dresden for funding his stay as postdoc. The authors appreciate Dr. H. Brodowsky, Dr. H. Brünig, Mr. W. Ehrentraut, Dr. S.-L. Gao, Mrs. C. Goltzsche, , Mr. J. Rausch, Dr. S. Schwarz (IPF Dresden e.V), Dr. J. Asrar, Dr. D. Blasini, Dr. A. Ferryman, and Dr. K. Gleich (JMTC) for their experimental assistance and helpful discussions.

### Abbreviation list

| | |
|---|---|
| AFM | atomic force microscopy |
| γ-APS | 3-aminopropyltriethoxylsilane |
| EKA | electrokinetic analysis |
| GF | glass fibre |
| IEP | isoelectric point |
| IPN | interpenetrating network |
| LOI | loss-on-ignition |
| MAH-*g*-PP | maleic anhydride grafted polypropylene |
| PF | polymeric film former |
| PP | polypropylene |
| $R_q$ | root mean square roughness |
| $R_{\max}$ | maximum roughness |
| ToF-SIMS | time-of-flight secondary ion mass spectroscopy |
| UD | unidirectional |
| XPS | X-ray photoelectron spectrometer |
| $\theta_a$ | advancing contact angle |
| $\theta_r$ | receding contact angle |

## References

[1] Kim J-K., Mai Y-W.: High strength, high fracture toughness fibre composites with interface control – A review. Composites Science and Technology, **41**, 333–378 (1991). DOI: 10.1016/0266-3538(91)90072-W

[2] Pukánszky B.: Interfaces and interphases in multicomponent materials: Past, present, future. European Polymer Journal, **41**, 645–662 (2005). DOI: 10.1016/j.eurpolymj.2004.10.035

[3] Ishida H.: A review of recent progress in the studies of molecular and microstructure of coupling agents and their functions in composites, coatings and adhesive joints. Polymer Composites, **5**, 101–123 (1984). DOI: 10.1002/pc.750050202

[4] Drzal L-T., Rich M-J., Lloyd P-F.: Adhesion of graphite fibers to epoxy matrices: I. The role of fiber surface treatment. The Journal of Adhesion, **16**, 1–30 (1983). DOI: 10.1080/00218468308074901

[5] Ishikawa T., Yamaoka H., Harada Y., Fujii T., Nagasawa T.: A general process for *in situ* formation of functional surface layers on ceramics. Nature, **416**, 64–67 (2002). DOI: 10.1038/416064a

[6] Munz M., Sturm H., Schulz E., Hinrichsen G.: The scanning force microscope as a tool for the detection of local mechanical properties within the interphase of fibre reinforced polymers. Composites Part A: Applied Science and Manufacturing, **29**, 1251–1259 (1998). DOI: 10.1016/S1359-835X(98)00077-3

[7] Mai K., Mäder E., Mühle M.: Interphase characterization in composites with new non-destructive methods. Composites Part A: Applied Science and Manufacturing, **29**, 1111–1119 (1998). DOI: 10.1016/S1359-835X(98)00092-X

[8] Gao S-L., Mäder E.: Characterisation of interphase nanoscale property variations in glass fibre reinforced polypropylene and epoxy resin composites. Composites Part A: Applied Science and Manufacturing, **33**, 559–576 (2002). DOI: 10.1016/S1359-835X(01)00134-8

[9] Bergeret A., Bozec M-P., Quantin J-C., Crespy A., Gasca J-P., Arpin M.: Study of interphase in glass fiber-reinforced poly(butylene terephthalate) composites. Polymer Composites, **25**, 12–25 (2004). DOI: 10.1002/pc.20001

[10] Feuillade V., Bergeret A., Quantin J-C., Crespy A.: Relationships between the glass fibre sizing composition and the surface quality of sheet moulding compounds (SMC) body panels. Composites Science and Technology, **66**, 115–127 (2006). DOI: 10.1016/j.compscitech.2005.05.009

[11] Feuillade V., Bergeret A., Quantin J-C., Crespy A.: Characterisation of glass fibres used in automotive industry for SMC body panels. Composites Part A: Applied Science and Manufacturing, **37**, 1536–1544 (2006). DOI: 10.1016/j.compositesa.2005.11.010

[12] Mäder E., Pisanova E.: Interfacial design in fiber reinforced polymers. Macromolecular Symposia, **163**, 189–212 (2001). DOI: 10.1002/1521-3900(200101)163:1<189::AID-MASY189>3.0.CO;2-8

[13] Jones F-R.: Interphase formation and control in fibre composite materials. Key Engineering Materials, **116–117**, 41–60 (1996). DOI: 10.4028/www.scientific.net/KEM.116-117.41

[14] Mäder E., Pisanova E.: Characterization and design of interphases in glass fiber reinforced polyproplyene. Polymer Composites, **21**, 361–368 (2000). DOI: 10.1002/pc.10194

[15] Jensen R. E., McKnight S. H.: Inorganic-organic fiber sizings for enhanced energy absorption in glass fiber-reinforced composites intended for structural applications. Composites Science and Technology, **66**, 509–521 (2006). DOI: 10.1016/j.compscitech.2005.06.004

[16] Gao X., Jensen R-E., Li W., Deitzel J., McKnight S-H., Gillespie J-W.: Effect of fiber surface texture created from silane blends on the strength and energy absorption of the glass fiber/epoxy interphase. Journal of Composite Materials, **42**, 513–534 (2008). DOI: 10.1177/0021998307086203

[17] Danner K-M., Dey M., McAllister Q-P., Barsotti R-J., Kissounko D-A.: Synergetic behavior of low $T_g$ polybutadiene polymers and polysiloxanes as components for glass fiber sizing in composite materials. Journal of Applied Polymer Science, **118**, 841–848 (2010). DOI: 10.1002/app.32333

[18] Mäder E., Moos E., Karger-Kocsis J.: Role of film formers in glass fibre reinforced polypropylene – New insights and relation to mechanical properties. Composites Part A: Applied Science and Manufacturing, **32**, 631–639 (2001). DOI: 10.1016/S1359-835X(00)00156-1

[19] Zinck P., Mäder E., Gerard J-F.: Role of silane coupling agent and polymeric film former for tailoring glass fiber sizings from tensile strength measurements. Journal of Materials Science, **36**, 5245–5252 (2001). DOI: 10.1023/A:1012410315601

[20] Frenzel H., Mäder E.: Influence of different interphases on the mechanical properties of fiber-reinforced polymers. Progress in Colloid and Polymer Science, **101**, 199–202 (1996). DOI: 10.1007/BFb0114470

[21] Thomason J-L., Adzima L-J.: Sizing up the interphase: An insider's guide to the science of sizing. Composites Part A: Applied Science and Manufacturing, **32**, 313–321 (2001). DOI: 10.1016/S1359-835X(00)00124-X

[22] Thomason J-L., Schoolenberg G-E.: An investigation of glass fibre/polypropylene interface strength and its effect on composite properties. Composites, **25**, 197–203 (1994). DOI: 10.1016/0010-4361(94)90017-5

[23] Frenzel H., Bunzel U., Häßler R., Pompe G.: Influence of different glass fiber sizings on selected mechanical properties of PET/glass composites. Journal of Adhesion Science and Technology, **14**, 651–660 (2000). DOI: 10.1163/156856100742906

[24] Lariviere D., Krawczak P., Tiberi C., Lucas P.: Interfacial properties in commingled yarn thermoplastic composites. Part II: Influence on crack initiation and propagation. Polymer Composites, **25**, 589–600 (2004). DOI: 10.1002/pc.20053

[25] Lariviere D., Krawczak P., Tiberi C., Lucas P.: Interfacial properties in commingled yarn thermoplastic composites. Part I: Characterization of the fiber/matrix adhesion. Polymer Composites, **25**, 577–588 (2004). DOI: 10.1002/pc.20052

[26] Ishida H., Naviroj S., Tripathy S-K., Fitzgerald J-J., Koenig J-L.: The structure of an aminosilane coupling agent in aqueous solutions and partially cured solids. Journal of Polymer Science: Polymer Physics Edition, **20**, 701–718 (1982). DOI: 10.1002/pol.1982.180200412

[27] Ishida H., Koenig J-L.: Fourier transform infrared spectroscopic study of the structure of silane coupling agent on E-glass fiber. Journal of Colloid and Interface Science, **64**, 565–576 (1978). DOI: 10.1016/0021-9797(78)90398-3

[28] Naviroj S., Culler S-R., Koenig J-L., Ishida H.: Structure and adsorption characteristics of silane coupling agents on silica and E-glass fiber; Dependence on pH. Journal of Colloid and Interface Science, **97**, 308–317 (1984). DOI: 10.1016/0021-9797(84)90301-1

[29] Liu X-M., Thomason J-L., Jones F-R.: XPS and AFM study of interaction of organosilane and sizing with E-glass fibre surface. The Journal of Adhesion, **84**, 322–338 (2008). DOI: 10.1080/00218460802004386

[30] Wang D., Jones F-R.: Surface analytical study of the interaction between γ-amino propyl triethoxysilane and E-glass surface. Part II X-ray photoelectron spectroscopy. Journal of Materials Science, **28**, 2481–2488 (1993). DOI: 10.1007/BF01151683

[31] Wang D., Jones F-R., Denison P.: Surface analytical study of the interaction between γ-amino propyl triethoxysilane and E-glass surface. Part I: Time-of-flight secondary ion mass spectrometry. Journal of Materials Science, **27**, 36–48 (1992). DOI: 10.1007/BF02403641

[32] Benkoski J-J., Kramer E-J., Yim H., Kent M-S., Hall J.: The effects of network structure on the resistance of silane coupling agent layers to water-assisted crack growth. Langmuir, **20**, 3246–3258 (2004). DOI: 10.1021/la035920k

[33] Plonka R., Mäder E., Gao S-L., Bellmann C., Dutschk V., Zhandarov S.: Adhesion of epoxy/glass fibre composites influenced by aging effects on sizings. Composites Part A: Applied Science and Manufacturing, **35**, 1207–1216 (2004). DOI: 10.1016/j.compositesa.2004.03.005

[34] Darbha S., Mittal K-L.: Effect of pH of silane solution on the adhesion of polyimide to a silica substrate. Journal of Applied Polymer Science, **29**, 2039–2043 (1984). DOI: 10.1002/app.1984.070290612

[35] Thomason J-L., Dwight D-W.: The use of XPS for characterisation of glass fibre coatings. Composites Part A: Applied Science and Manufacturing, **30**, 1401–1413 (1999). DOI: 10.1016/S1359-835X(99)00042-1

[36] Zhuang R-C., Burghardt T., Mäder E.: Study on interfacial adhesion strength of single glass fibre/polypropylene model composites by altering the nature of the surface of sized glass fibres. Composites Science and Technology, **70**, 1523–1529 (2010). DOI: 10.1016/j.compscitech.2010.05.009

[37] Mäder E., Rothe C., Gao S-L.: Commingled yarns of surface nanostructured glass and polypropylene filaments for effective composite properties. Journal of Materials Science, **42**, 8062–8070 (2007). DOI: 10.1007/s10853-006-1481-x

[38] Reinhardt S., Steinert V., Werner K.: Investigations on the dissociation behaviour of hydrolyzed alternating copolymers of maleic anhydride and propene-I. Potentiometric titrations. European Polymer Journal, **32**, 935–938 (1996). DOI: 10.1016/0014-3057(96)00028-6

[39] Schweiss R., Welzel P-B., Werner C., Knoll W.: Dissociation of surface functional groups and preferential adsorption of ions on self-assembled monolayers assessed by streaming potential and streaming current measurements. Langmuir, **17**, 4304–4311 (2001). DOI: 10.1021/la001741g

[40] Heise A., Menzel H., Yim H., Foster M-D., Wieringa R-H., Schouten A-J., Erb V., Stamm M.: Grafting of polypeptides on solid substrates by initiation of *N*-carboxyanhydride polymerization by amino-terminated self-assembled monolayers. Langmuir, **13**, 723–728 (1997). DOI: 10.1021/la960467g

[41] Bayer T., Eichhorn K-J., Grundke K., Jacobasch H-J.: FTIR spectroscopic studies of interfacial reactions between amino functionalized silicon surfaces and molten maleic anhydride copolymers. Macromolecular Chemistry and Physics, **200**, 852–857 (1999). DOI: 10.1002/(SICI)1521-3935(19990401)200:4<852::AID-MACP852>3.0.CO;2-V

[42] Lee L-H.: Wettability and conformation of reactive polysiloxanes. Journal of Colloid and Interface Science, **27**, 751–760 (1968). DOI: 10.1016/0021-9797(68)90109-4

[43] Bascom W-D.: Structure of silane adhesion promoter films on glass and metal surfaces. Macromolecules, **5**, 792–798 (1972). DOI: 10.1021/ma60030a024

[44] Wu H-F., Dwight D-W., Huff N-T.: Effects of silane coupling agents on the interphase and performance of glass-fiber-reinforced polymer composites. Composites Science and Technology, **57**, 975–983 (1997). DOI: 10.1016/S0266-3538(97)00033-X

[45] Rosenholm J-M., Lindén M.: Wet-chemical analysis of surface concentration of accessible groups on different amino-functionalized mesoporous SBA-15 silicas. Chemistry of Materials, **19**, 5023–5034 (2007). DOI: 10.1021/cm071289n